

KILIAN POLLOK

CRYSTAL GROWTH PATTERNS  
IN SOLID SOLUTION SYSTEMS:  
CASE STUDIES ON  
OSCILLATORY ZONING AND  
MINERAL REPLACEMENT REACTIONS

2004



Angewandte Mineralogie–Kristallographie

**Crystal growth patterns in solid solution systems:  
Case studies on  
oscillatory zoning and  
mineral replacement reactions**

**Inaugural-Dissertation**

zur Erlangung des Doktorgrades der Naturwissenschaften  
im Fachbereich Geowissenschaften  
der Mathematisch-Naturwissenschaftlichen Fakultät  
der Westfälischen Wilhelms-Universität Münster

vorgelegt von

**Kilian Pollok**

aus Hildesheim

-2004-

---

Dekan:	Prof. Dr. Hans Kerp
Erster Gutachter:	Prof. Dr. Andrew Putnis
Zweiter Gutachter:	Prof. Dr. Chris Ballhaus
Tag der mündlichen Prüfung:	26.01.2005
Tag der Promotion:	28.01.2005

# Contents

<b>Abstract - Zusammenfassung</b>	<b>1</b>
<b>Introduction and objective</b>	<b>9</b>
<b>I Oscillatory zoning</b>	<b>13</b>
<b>1 Analytical transmission electron microscopy on oscillatory zoned grandite garnets from Oslo rift</b>	<b>15</b>
1.1 Introduction . . . . .	15
1.2 Sample and experimental . . . . .	17
1.2.1 Spatial and 'chemical' resolution of ATEM . . . . .	18
1.3 Results . . . . .	19
1.3.1 Microstructural observations and microstructure-composition relationships . . . . .	19
1.3.2 Correlation of ATEM observations to the EMP-profile	22
1.4 Discussion . . . . .	24
1.4.1 Microstructure and oscillatory zoning . . . . .	24
1.4.2 Microstructure and birefringence . . . . .	28
1.5 Conclusion . . . . .	29
<b>Supplemental material to Chapter 1</b>	<b>31</b>
1.6 Analysis of grossular-rich oscillatory zoned grandites from Oslo rift area . . . . .	31
1.6.1 Results and Discussion . . . . .	33
1.7 Limits of fractal geometry in the analysis of oscillatory zoning patterns . . . . .	36
1.7.1 Fractal statistics: the Hurst exponent . . . . .	36
1.7.2 Fractal analyses of OZPs: the problem of spatial resolution . . . . .	38
1.7.3 Criticism and perspective . . . . .	41

<b>2</b>	<b>Molecular simulations of interfacial and thermodynamic mixing properties of grossular–andradite garnets</b>	<b>43</b>
2.1	Introduction . . . . .	43
2.2	Methods . . . . .	45
2.2.1	Derivation of force-field parameters . . . . .	45
2.2.2	Calculation of cation–cation interaction parameters . . . . .	49
2.2.3	Determination of thermodynamic properties . . . . .	51
2.2.4	Calculation of the vibrational entropy and the zero-point energy . . . . .	53
2.3	Results . . . . .	55
2.3.1	Comparison of experimental and calculated cell parameters . . . . .	55
2.3.2	Enthalpies of mixing . . . . .	56
2.3.3	Free energies and entropies of mixing . . . . .	57
2.3.4	Processes at interfaces . . . . .	60
2.4	Discussion . . . . .	66
2.4.1	Nonideality and miscibility gaps . . . . .	66
2.4.2	Ordering in grandites . . . . .	68
2.4.3	Hints to the formation conditions of natural grossular–andradite mixtures in relation to thermodynamic equilibrium . . . . .	69
<b>II</b>	<b>Replacement reactions</b>	<b>71</b>
<b>3</b>	<b>An analytical TEM study on complex zoning patterns in garnets from Bergen Arcs eclogites</b>	<b>73</b>
3.1	Introduction . . . . .	73
3.2	Geologic setting . . . . .	74
3.2.1	Stages of eclogitisation . . . . .	76
3.3	Analytical methods and sample assortment . . . . .	76
3.3.1	Patterns in garnets . . . . .	79
3.4	Results . . . . .	79
3.4.1	Microstructure and compositional interfaces in garnets . . . . .	79
3.4.2	Microstructures in plagioclase and omphacite . . . . .	83
3.5	Discussion . . . . .	84

<b>4 Volume changes of replacement reactions in solid solution-aqueous solution systems: Theoretical considerations on the example of the KBr – KCl – H<sub>2</sub>O system</b>	<b>89</b>
4.1 Introduction . . . . .	89
4.2 Solubility and equilibrium in SS-AS systems: I. System without solid solution . . . . .	91
4.3 Solubility and equilibrium in SS-AS systems: II. System with complete solid solution . . . . .	93
4.3.1 The Lippmann phase diagram . . . . .	94
4.3.2 The solubility phase diagram . . . . .	96
4.4 Volume change . . . . .	100
4.5 Reaction paths in the AB – AC – H <sub>2</sub> O system . . . . .	102
4.5.1 Local volume change . . . . .	105
4.6 Reaction paths and volume changes in the KBr – KCl – H <sub>2</sub> O system . . . . .	106
4.6.1 Dissolution of KBr in various solutions . . . . .	106
4.6.2 Dissolution of KCl in various solutions . . . . .	109
4.6.3 Kinetic considerations . . . . .	111
4.7 Replacement experiments in the KBr – KCl – H <sub>2</sub> O system .	113
4.7.1 Experimental procedure . . . . .	113
4.7.2 Experimental results: Texture, composition and replacement rate . . . . .	115
4.7.3 Calculated results: reaction paths and volume changes	120
4.8 Conclusion and broader impact . . . . .	126
<b>Acknowledgement/Danksagung</b>	<b>129</b>
<b>Bibliography</b>	<b>131</b>





# List of Figures

0.1	Oscillatory zoning of grandite garnet and replacement of KBr by K(Br,Cl) . . . . .	9
1.1	Optical micrograph, BSE image and EMP profile of an oscillatory zoned grandite garnet . . . . .	18
1.2	TEM micrographs and DP showing fine, non-periodic and periodic oscillatory zoning $\perp$ to (1 1 0) . . . . .	21
1.3	TEM micrograph with EDX line scan showing bimodal compositions of lamellae . . . . .	22
1.4	HRTEM image of a compositional interface {1 1 0} . . . . .	23
1.5	BSE image and EMP line scan of a zoned, grossular-rich garnet	33
1.6	TEM micrograph with EDX line scan of fine oscillatory zoning	34
1.7	TEM micrograph of fine oscillatory zoning . . . . .	34
1.8	Examples of self-affine fractals with different (local) fractal dimension . . . . .	38
1.9	Measured and simulated oscillatory zoning pattern . . . . .	40
1.10	The width $w$ of the measured and simulated OZP plus literature data from Holten <i>et al.</i> (1997) . . . . .	41
2.1	The compressibility of grossular and andradite . . . . .	46
2.2	Atomic model of an ordered 1:1 grossular–andradite conventional unit cell . . . . .	47
2.3	Atomic models of $4 \times 4 \times 4$ supercells . . . . .	48
2.4	Experimental and calculated cell parameters as function of composition of the grossular–andradite solid solution . . . . .	54
2.5	Excess enthalpies of mixing for different temperatures . . . . .	55
2.6	Free configurational energies of mixing for different temperatures and compositions . . . . .	58
2.7	Calculated phase diagram for the grossular–andradite solid solution . . . . .	59
2.8	Calculated configurational entropies of mixing . . . . .	60

2.9	Long-range order parameter $q$ as function of temperature and composition . . . . .	61
2.10	Calculated excess vibrational entropies of mixing . . . . .	62
2.11	Calculated vibrational zero-point energies of mixing . . . . .	63
2.12	Free energies of mixing with contributions from the configurational energy, the excess vibrational entropy of mixing, and the excess zero-point energy . . . . .	64
2.13	Interface $\parallel (1\ 1\ 1)$ for an $\text{Fe}^{3+}/(\text{Al} + \text{Fe}^{3+})$ ratio of 0.75 . . . . .	65
3.1	Geological map of NW Holsnøy . . . . .	75
3.2	Examples for incomplete eclogite formation from granulites.	77
3.3	BSE images of replacement patterns in garnet . . . . .	78
3.4	TEM micrograph of garnet microstructures . . . . .	80
3.5	TEM micrograph of an unknown feature in garnet . . . . .	80
3.6	EDX profile of the grt-grt interface . . . . .	81
3.7	TEM micrograph of exsolution in plagioclase . . . . .	83
3.8	TEM micrograph of anti-phase domains in omphacite . . . . .	85
3.9	Size of anti-phase domains in omphacite as a function of temperature . . . . .	86
4.1	Solubility diagram of the NaCl – KCl – H <sub>2</sub> O system . . . . .	92
4.2	Lippmann diagram of the KBr – KCl – H <sub>2</sub> O system . . . . .	95
4.3	Solubility phase diagram of the KBr – KCl – H <sub>2</sub> O system . . . . .	97
4.4	Solubility and solubility phase diagram with reaction path samples . . . . .	103
4.5	Relative volume changes in various solutions . . . . .	108
4.6	Mass of substrate dissolved to reach a certain solution composition . . . . .	112
4.7	Texture of the replaced surface of a KBr crystal . . . . .	115
4.8	SE and BSE images of the interface between replacement and unreacted KBr core . . . . .	116
4.9	EMP line scans on partly replaced KBr crystals . . . . .	117
4.10	Relative reaction rates for KBr substrate and different starting solutions . . . . .	117
4.11	Texture of the replaced surface of a KCl crystal . . . . .	118
4.12	BSE images of the interface between the replaced part and the unreacted KCl core . . . . .	119

*LIST OF FIGURES*

vii

4.13 EMP line scans on partly replaced KCl crystals . . . . .	120
4.14 Relative reaction rates for KCl substrate and different starting solutions . . . . .	120
4.15 Solubility diagram with traces for the various solutions and substrates . . . . .	123



# List of Tables

1.1	EMP and ATEM data for oscillatory zoned grandite garnets	20
1.2	EMP and ATEM data for oscillatory zoned grossular-rich garnets . . . . .	32
2.1	Potential parameters for the interactions within grossular and andradite as used for the GULP calculations . . . . .	50
2.2	Comparison of experimental and calculated structural parameters, elastic constants, dielectric constants, and third-law vibrational entropies . . . . .	52
2.3	Cation–cation interactions that were considered to describe the energetics of cation ordering and the enthalpy of mixing.	53
2.4	Atomic positions and physical properties of ordered grandite for $T = 0\text{ K}$ . . . . .	57
2.5	Interface energies for grossular–grandite and grandite–andradite interfaces . . . . .	64
2.6	Refractive indices for different garnets and garnet interfaces	66
4.1	Calculated parameters of volume change for the dissolution of KBr in initially pure saturated KCl solution ( $X_{Br,aq}^{init} = 0$ ) . .	107
4.2	Calculated parameters of volume change for the dissolution of KCl in initially pure saturated KBr solution ( $X_{Br,aq}^{init} = 1$ ) . .	110
4.3	Starting solutions used in the replacement experiments . . .	114
4.4	Calculated parameters of the experimental replacement reactions . . . . .	124



# Abstract

The available work on crystal growth patterns in solid solution systems is subdivided in two parts: I. oscillatory zoning and II. mineral replacement reactions. Each of these parts consists of two chapters with self-contained studies. The first study deals with analytical transmission electron microscopy (ATEM) on natural samples and the second one presents a theoretical model that examines a specific problem arising from the microscopic analysis, respectively. The following topics will be discussed:

## I. Oscillatory zoning

- 1 Analytical transmission electron microscopy on oscillatory zoned grossular–andradite garnets from Oslo rift
- 2 Molecular simulations of interfacial and thermodynamic mixing properties of grossular–andradite garnets

## II. Mineral replacement patterns

- 3 Analytical transmission electron microscopy on the mechanisms of eclogitisation: a study on complex replacement patterns in garnets of Bergen arc eclogites
- 4 Volume changes of replacement reactions in solid solution–aqueous solution systems: Theoretical considerations on the example of the KBr–KCl–H<sub>2</sub>O system

**Chapter 1** Analytical transmission electron microscopy (ATEM) has been used to determine the scale and the interface characteristics of oscillatory zoning in the solid solution of grossular–andradite (grandite) garnets. Oscillatory zoning on the nanometre scale was directly observed and quantitatively analysed. The composition of adjacent zones alternates between two limiting values, i.e., they are compositionally bimodal. High resolution (HRTEM) images show that the compositional interfaces are sharp and coherent.

From the microscopic and analytical findings the underlying growth dynamics can be constrained which indicates the importance of the local (non-linear) growth dynamics in generating oscillatory zoning patterns in addition to the long-considered external forcing. Furthermore, the spatial resolution of the analytical technique applied to oscillatory zoning patterns is demonstrated to be crucial to determine the 'real' pattern and its correct fractal characteristics as well as to suggest causes for the unusual optical properties of zoned grandite garnets.

**Chapter 2** The thermodynamic mixing properties and the stability of compositional interfaces of the grossular–andradite solid solution have been determined using empirical force-field interactions and Monte Carlo simulations. Cation ordering of Al and Fe<sup>3+</sup> on the octahedral site of the garnet structure influences the thermodynamic parameters below  $\approx 500$  K and leads to the an ordered grandite at  $X_{and} = 0.50$  with alternating Al and Fe<sup>3+</sup> along the main cubic crystallographic axes below 500 K. The free energies of mixing indicate two miscibility gaps, one between grossular and an ordered grandite of  $X_{and} = 0.50$  and the other between the same ordered configuration and andradite. However, the miscibility gaps take effect only for temperatures close to room temperature and thus are negligible for garnet growth in geologic environments. The interface energies of compositional interfaces, as experimentally found by ATEM, are comparably low for interfaces between the end members and the ordered grandite which may explain the stability of such microstructure formed during growth.

On the basis of the modelling results, the bimodal compositional distribution found on nanometre scale in oscillatory zoned garnets is arguably not enforced by growth in regions of immiscibility but rather is caused by kinetic effects at the solid–fluid interface.

**Chapter 3** Eclogite facies rocks within the Bergen Arcs, western Norway, have formed from granulites along shear zones and fluid pathways. Garnets that were inherited from granulite facies protoliths show different types of replacement patterns due to an incomplete eclogitisation process including concentric rim zoning, zoning along vein fillings and inclusion trails, and zoning bands without inclusions. The interfacial part between the granulitic core and the eclogitic rim of garnet as well as the microstructure of other relevant mineral (omphacite, plagioclase) have been analysed using ATEM.



In garnet, the interface is characterised by a gradual changes in composition from  $X_{alm} = 0.31$ ,  $X_{pyr} = 0.50$  to  $X_{alm} = 0.54$ ,  $X_{pyr} = 0.25$  within  $\approx 20 \mu\text{m}$  and exhibits no distinct microstructure. Granulitic plagioclase shows exsolution lamellae of the Bøggild intergrowth. In omphacite, anti-phase domains (APDs) which potentially record the temperature of mineral growth have been observed.

The appearance of the compositional profile in garnet can be described by diffusion across an initially sharp interface. However, diffusion appears to represent a process that acts subsequent to the eclogitisation reactions. The metamorphic processes that occurred in a spatially heterogeneous manner involve feedback between deformation, fluid infiltration, and chemical reactions and that operate simultaneously in different parts and at different scales of the rock. It can be suggested that the eclogitisation process was rather brief and self-limiting due to the change in rheology associated with the conversion of brittle granulite to ductile eclogite and their consequences for pervasive fluid flow. Although the replacement patterns indicate dissolution and reprecipitation in an open system, the mechanisms and kinetics of garnet re-equilibration were obscured by diffusion within the further retrograde metamorphic history.

**Chapter 4** A universal model for the calculation of volume changes due to replacement reactions in solid solution-aqueous solution systems is presented. The model utilises the thermodynamic representation of a modified Lippmann phase diagram and the solubility of the solid solution to reconstruct the effective reaction paths as a dissolution-precipitation reaction. The difference in solubility between the initial phase and the replacement has been found to result in a substantial contribution to the relative volume change that can be texturally linked to the generation of porosity or the formation of an overgrowth.

Using the  $\text{KBr} - \text{KCl} - \text{H}_2\text{O}$  system as an example it can be shown in theory and experiment that the texture and composition of the replacements as well as the kinetics of the reaction can be predicted. The model provides a detailed picture on the parameters that control, e.g., the porosity generation. Transferring the concept of volume change in replacement reactions from the modelled reaction paths to the microporosity observed in various natural and experimental samples may give an insight on the approximate reaction paths and relative solubilities in systems for which fluid compositions are unknown. Furthermore, the determination of parameters

#### 4      *CRYSTAL GROWTH PATTERNS IN SOLID SOLUTION SYSTEMS*

that control the porosity generation by mineral reactions and, thus, partly the permeability of rock is crucial to understand mechanisms and kinetics of the re-equilibration of mineral phase assemblages especially during retrograde metamorphism.

# Zusammenfassung

Die vorliegende Arbeit über Kristallwachstumsmuster in Mischkristallsystemen ist in zwei Themenkomplexe unterteilt: I. oszillierende Zonierung und II. Mineralverdrängungsreaktionen. Jeder Teil enthält zwei in sich abgeschlossene Studien, wobei sich jeweils die erste mit der analytischen Transmissions-Elektronenmikroskopie (ATEM) an natürlichen Proben befasst und die zweite ein theoretisches Modell vorstellt, das ein in der mikroskopischen Untersuchung auftretendes, spezifisches Problem behandelt. Die folgenden Themen werden besprochen:

## I. Oszillierende Zonierung

- 1 Analytische Transmissions-Elektronenmikroskopie an oszillierend zonierten Grandite-Granaten des Oslo Grabens
- 2 Molekular-Simulationen von Grenzflächeneigenschaften und thermodynamischen Mischungseigenschaften an Granaten der Grossular-Andradit-Reihe

## II. Mineralverdrängungsreaktionen

- 3 Analytische Transmissions-Elektronenmikroskopie zur Untersuchung von Eklogitisierungsmechanismen: eine Studie an komplexen Mineralverdrängungsmustern in Granaten der "Bergen Arc"-Eklogite  
(Anmerkung: Die "Bergen Arcs" bestehen aus einer Serie von Überschiebungsdecken, die bogenförmig um Bergen angeordnet sind.)
- 4 Volumenänderungen bei Verdrängungsreaktionen in Systemen Mischkristall (feste Lösung)-wässrige Lösung: Theoretische Betrachtungen am Beispiel des KBr-KCl-H<sub>2</sub>O-Systems

**Kapitel 1** Mit der analytischen Transmission-Elektronenmikroskopie (ATEM) wurde der Maßstab und die Grenzflächencharakteristika von os-

zillierender Zonierung in Grossular-Andradit (Grandite)- Mischkristallen bestimmt. Oszillierende Zonierung im Nanometer-Bereich wurde erstmals direkt beobachtet und quantitativ analysiert. Die Zusammensetzung benachbarter Zonen alterniert zwischen zwei Grenzwerten und kann daher als bimodal angesehen werden. Mit hochaufgelösten TEM-Bildern konnten die Grenzflächen zwischen verschiedenen Zusammensetzungen als scharf und kohärent bestimmt werden.

Mit den mikroskopischen und analytischen Ergebnissen kann die zu Grunde liegende Wachstumsdynamik eingegrenzt werden. Diese zeigt die Bedeutung der lokalen (nicht-linearen) Wachstumsdynamik bei der Erzeugung von oszillierenden Zonierungsmustern zusätzlich zum lange betrachteten äußeren Antriebskraft. Desweiteren wird gezeigt, dass das räumliche Auflösungsvermögen der auf die oszillierenden Zonierungsmuster angewandten analytischen Methode entscheidend ist, um sowohl die "realen" Wachstumsmuster und die dazugehörigen korrekten fraktalen Charakteristika korrekt zu bestimmen als auch um Gründe für die ungewöhnlichen optischen Eigenschaften der zonierten Grandite vorzuschlagen.

**Kapitel 2** Die thermodynamischen Mischungseigenschaften und die Stabilität von Grenzflächen zwischen Bereichen verschiedener Zusammensetzung in der Grossular-Andradit-Mischungsreihe wurden mit empirischen *force field* (Kraftfeld) Wechselwirkungen und Monte-Carlo Simulationen bestimmt. Kationenordnung von Al und  $\text{Fe}^{3+}$  auf dem oktaedrischen Gitterplatz der Granatstruktur beeinflusst die thermodynamischen Parameter unter  $\approx 500$  K und führt zu einem geordneten Grandit der Zusammensetzung  $X_{and} = 0.50$  mit alternierender Abfolge von Al und  $\text{Fe}^{3+}$  entlang der kristallographischen Hauptachse des kubischen Systems unter 500 K. Die freien Mischungsenergien zeigen zwei Mischungslücken an, eine zwischen Grossular und einem geordneten Grandit der Zusammensetzung  $X_{and} = 0.50$  und eine weitere zwischen derselben geordneten Konfiguration und Andradit. Allerdings werden die Mischungslücken nur bei Temperaturen nahe Raumtemperatur wirksam und sind daher für das Granatwachstum in geologischen Umgebungen vernachlässigbar. Grenzflächenenergien von Grenzflächen zwischen verschiedenen Zusammensetzungen, wie sie experimentell mit ATEM gefunden wurden, sind vergleichsweise klein gegenüber Grenzflächen zwischen den Endgliedern und geordnetem Grandit, was die Stabilität einer solchen während des Kristallwachstums gebildeten Mikrostruktur erklären könnte.

Auf der Basis der Modellierungsergebnisse ist die bimodale Zusammensetzungsverteilung, die im Nanometerbereich in oszillierend zonier-

ten Granaten gefunden wurde, wohl nicht durch Wachstum im Bereich der Nichtmischbarkeit erzwungen, sondern ist vielmehr durch kinetische Effekte an der Festkörper-Fluid Grenzfläche verursacht.

**Kapitel 3** Eklogit-fazielle Gesteine innerhalb des "Bergen Arc", West-Norwegen, entstanden aus Granuliten entlang von Scherzonen und Fluidbahnen. Die vom Granulit-faziellen Protolith ererbten Granate zeigen unterschiedliche Arten von Mineralverdrängungsmustern, die durch einen unvollständigen Eklogitisierungsprozess entstanden sind und konzentrische Randzonierung, Zonierungen entlang von Aderfüllungen und Spuren von Einschlüssen, und Zonierungsbänder ohne Einschlüsse einschließen. Sowohl die Grenzfläche zwischen dem granulitischem Kern und dem eklogitischem Rand der Granate als auch die Mikrostruktur anderer relevanter Minerale (Omphazit, Plagioklas) wurden mit ATEM untersucht.

Die Grenzfläche im Granat ist charakterisiert durch graduelle Änderungen in der Zusammensetzung von  $X_{alm} = 0.31$ ,  $X_{pyr} = 0.50$  zu  $X_{alm} = 0.54$ ,  $X_{pyr} = 0.25$  über  $\approx 20 \mu\text{m}$  und zeigt keine deutliche Mikrostruktur. Granulitische Plagioklase zeigen Entmischungslamellen, die auf die Bøggild-Mischungslücke zurückzuführen sind. Antiphase-domänen (APD) in Omphazit, die potenziell die Temperatur des Mineralwachstums anzeigen können, wurden ebenfalls beobachtet.

Das Auftreten eines Zusammensetzungsprofils im Granat kann durch Diffusion über eine anfänglich scharfe Grenzfläche beschrieben werden. Diffusion scheint allerdings ein Prozess zu sein, der nach dem Eklogitisierungsprozess abläuft. Die metamorphen Prozesse erfolgen räumlich in einer heterogenen Weise, die ein Feedback zwischen Deformation, Fluidinfiltration und chemischer Reaktion beinhaltet und die gleichzeitig in verschiedenen Teilen und in verschiedenen Größenbereichen im Gestein ablaufen. Durch Änderungen in der Rheologie assoziiert mit der Umwandlung von sprödem Granulit in duktilen Eklogit und deren Konsequenz für einen durchdringenden Fluidtransport kann vermutet werden, daß der Eklogitisierungsprozeß eher kurz und selbstbeschränkend war. Obwohl die Mineralverdrängungsmuster auf Lösung und Fällung hindeuten sind die Mechanismen und die Kinetik der Reäquilibration von Granat verdeckt durch post-metamorphe Diffusion.

**Kapitel 4** Ein universales Modell für die Berechnung von Volumenänderungen bei Verdrängungsreaktionen in Systemen Mischkristall (feste Lösung)-wässrige Lösung wird vorgestellt. Das Modell benutzt zur

thermodynamischen Darstellung ein modifiziertes Lippmann-Phasendiagramm and die Löslichkeit des Mischkristalls, um den effektiven Reaktionsweg einer Lösungs-Fällungsreaktion zu rekonstruieren. Die Unterschied in der Löslichkeit zwischen der initialen und der verdrängenden Phase ergibt einen wesentlichen Beitrag zur relativen Volumenänderung, die texturell mit der Bildung von Porosität oder Bildung einer Überwachsung verknüpft werden kann.

Mit dem Beispielsystem  $\text{KBr} - \text{KCl} - \text{H}_2\text{O}$  kann in Theorie und Experiment gezeigt werden, daß sowohl die Textur und die Zusammensetzung der verdrängenden Phase als auch die Kinetik der Reaktion vorhergesagt werden können. Das Modell bietet ein detailliertes Bild über die Parameter, die z.B. die Bildung von Porosität beeinflussen. Überträgt man das Konzept der Volumenänderung in Mineralverdrängungsreaktionen von dem modellierten Reaktionswegen auf die Mikroporosität, die in verschiedenen natürlichen und experimentellen Proben gefunden wurde, so kann ein Einblick in den ungefähren Reaktionsweg und die relativen Löslichkeiten für Systeme gewonnen werden, deren Fluidzusammensetzung unbekannt ist. Außerdem ist die Bestimmung von Parametern, die für die Erzeugung von Porosität durch Mineralreaktionen von Bedeutung sind und daher teilweise auch die Permeabilität des Gesteins beeinflussen von großem Interesse, um die Mechanismen und die Kinetik der Reäquilibration von Mineralparagenesen besonders während der retrograden Metamorphose zu verstehen.

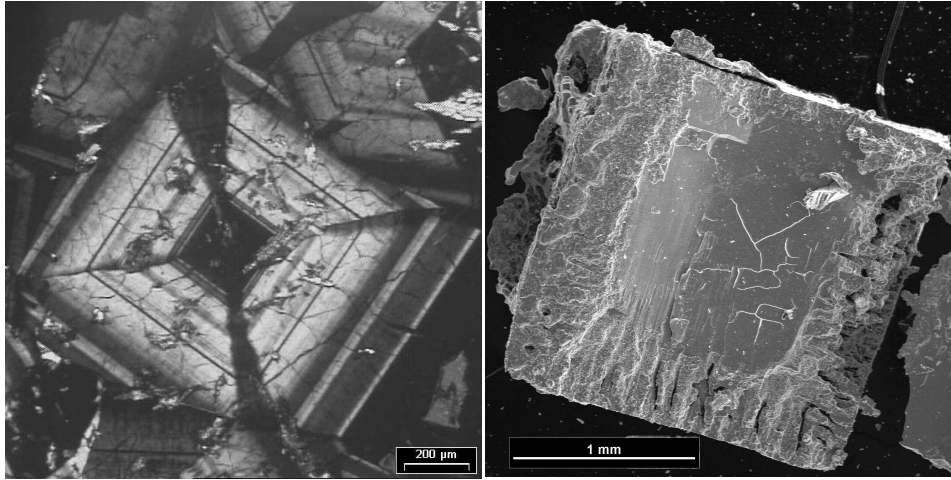


Figure 0.1: Crystal growth patterns: Oscillatory zoning of grandite garnet in cross-polarised light (*left*) and the partial replacement of KBr by K(Br,Cl) (*right*, SEM image from C. Putnis).

## Introduction and objective

The composition and morphology of growing crystals is controlled by a number of large scale and microscopic processes. These include the mineral (surface) structure, the growth conditions, the local growth kinetics, the partitioning between solute and solid, and the transport of material and heat. The interaction of these processes can lead to a variety of patterns formed by crystal growth such as mineral zonations, morphological instabilities and/or transitions, grain coarsening, eutectic intergrowths, and mineral replacements. Some patterns can be understood in terms of equilibrium thermodynamics while others require so-called far-from-equilibrium conditions to form.

Crystal growth patterns that have formed close to equilibrium (e.g., eutectic and exsolution intergrowth, prograde garnet zonation) can be used to determine the pressure-temperature-composition ( $p$ - $T$ - $x$ ) relations of a material or a rock. Although natural geological systems are never strictly

in equilibrium, a lot insight on the formation conditions of a given rock has been gained from the concepts of thermodynamics and phase equilibria in the last decades (e.g., Spear, 1993; Haasen, 1994). However, it has also become evident that a lot of processes that lead to pattern formation take place under far-from-equilibrium conditions (e.g., dendritic growth, Liesegang rings, see Jamtveit & Meakin, 1999, and references therein). These type of patterns attract growing attention because they have potentially stored information on the dynamics of the underlying processes.

In this work, two common crystal growth phenomena have been studied: oscillatory zoning and mineral replacement (Fig. 0.1). Both phenomena have been already recognised over a century ago (Blum, 1843; Herz, 1892; Lindgren, 1918; Phemister, 1934). Beside the aesthetic aspect, the considerable interest in these patterns is due to their prevalent occurrence in rock-forming and accessory minerals of various geological environments.

The origin of oscillatory zoning is often described as reflecting near-to-equilibrium growth of a under changing conditions, e.g., growth of plagioclase in a magma chamber with alternating melt composition, temperature, and/or pressure. According to Ortoleva *et al.* (1987), however, the essential requirements of a feature such as oscillatory zoning are: chemical disequilibrium and a feedback mechanism to change the reaction rate in response to the reaction that has already taken place. Additionally, noise in the system helps to stimulate the pattern formation without external forcing. In both cases, it is a matter of a dynamic system that acts at different spatial and temporal scales. Very few of the many published observation on oscillatory zoning have been made at the important 10–100 nanometre scale (Shore & Fowler, 1996) that is necessary to characterise the nature of the interface between two zones.

Generally, the chemical changes of an oscillatory zoned crystal can be described within a binary solid solution. The thermodynamic mixing properties of these solid solutions strongly affect the crystal-fluid equilibria as well as the stability of the chemical interfaces. However, for many solid solutions thermodynamic properties are difficult to determine experimentally at all relevant compositions and  $p$ - $T$  conditions, partly due to kinetics and metastability. Computer simulation methods provide an opportunity to calculate the thermodynamic properties and cation-ordering of solid solutions (see, e.g., Becker *et al.*, 2000; Bosenick *et al.*, 2001; Dove, 2001). They may offer the possibility to compare equilibrium thermodynamics with the



observed pattern and to judge whether the pattern forming process is conformable with near-equilibrium growth conditions.

Thus, the aims of the part on oscillatory zoning is to characterise the oscillatory zoning pattern of natural grossular-andradite (grandite) garnets in terms of microstructure and chemistry at the nanometre scale using analytical transmission electron microscopy (ATEM) and to calculate the local structural properties and energetics of the solid solution using molecular simulations. The results of the molecular simulation excited a limited investigation on grandite oscillatory zoning with a different composition of the zones. For clarity and to avoid confusion, this study has not been incorporated in Chapter 1 but is presented as supplemental material to this chapter (section 1.6). Another supplemental section deals with the limits of fractal geometry to describe oscillatory zoning patterns (section 1.7). Although beyond the actual scope of this work, the results obtained in Chapter 1 have some consequences for the use of fractal analysis which are briefly illustrated and discussed.

Mineral replacement reactions are of prime importance for the re-equilibration of metamorphic rocks. Generally speaking, changes in the physical and chemical environment led any assemblage of minerals response by approaching a new equilibrium state, i.e. by minimising the free energy of the system. Such response usually involves the transport of mass in the form of chemical species from the reactant minerals to the sides of crystal growth. In terms of re-equilibrating a mineral assemblage it is an important fact that most rock-forming silicates and many oxides are solid solutions (binary or multicomponent). Thus, they are capable to incorporate different cations on crystallographically defined sites as a function of  $p$ ,  $T$  and  $x$ . Such chemical substitutions in minerals are commonly described with the concept of exchange vectors (e.g., Spear, 1993). The same mineral phases (e.g. garnet) can be stable over a wide range of conditions by re-adjusting their composition which make them useful as geothermobarometers. However, it is crucial to define the underlying physical processes (intra- and intermineral) of chemical mass transport and reactions to gain insight into the degree and kinetics of re-equilibration.

In general, the transport of material through the minerals (intramineral volume diffusion) is comparatively slow to the transport through a network of grain boundaries, which at the time of metamorphism may have held an aqueous fluid that provides pathway for transport through the rock. In the presence of a fluid phase the dissolution and reprecipitation of minerals has been demonstrated to be a favourable process for

the re-equilibration of minerals (Putnis, 2002). Such process is most striking when the sites of dissolution and growth spatially coincide and form a pseudomorph, commonly observed in retrograde metamorphism. In that case the replacement is recognised by preserving the (often euhedral) shape of the former mineral. Although this common type of replacement has been described in great detail more than hundred years ago from hand specimens (Blum, 1843), there is still no comprehensive explanation on the coupling of processes at the side of reaction. Obviously, such coupling involves dissolution of the reactant parent mineral (out of equilibrium) and crystal growth of the replacement at the initial surface of the parent mineral (locally in equilibrium) which is usually observed as a moving reaction front from the surface/rim towards the core of the minerals. To keep such replacement front moving it has to stay in contact with the surrounding fluid phase. Although the preservation of volume is often emphasised as a prerequisite for pseudomorphs to form, porosity has been observed in many natural and experimental replacements (Putnis, 2002; Glikin *et al.*, 2003). A porosity which is generated by the replacement process would have a great impact on the kinetics of re-equilibration. The molar volume changes between the parent phase and the replacement are often not able to explain such generation of porosity. A proper knowledge about the thermodynamics of solid solution-aqueous solution systems is required to understand the compositional and textural changes of a replacement reactions. Due to the complexity of natural fluids and solid solutions and the uncertainty about the physical and chemical conditions in which the reactions have taken place, a comprehensive understanding can only be gained by studying simpler model systems.

The studies in the part on mineral replacement reactions aim at two quite different aspects. The first study deals with the re-equilibration mechanism of garnet within the fluid-induced transformation of a dry granulite to an eclogite with hydrous mineral phases. The eclogitisation resulted in complex compositional zoning patterns in the garnets. ATEM is used to characterise the microstructure and compositional interface at the nanometre scale. Furthermore, the microstructure of other eclogite facies minerals is studied. In the second study, the system  $\text{KBr} - \text{KCl} - \text{H}_2\text{O}$  is used as a model to calculate volume changes of solid solution-aqueous solution systems in a general way. Furthermore, the calculated values will be compared to results from replacement experiments in the model system.

*“The proof of the pudding is in the eating. By a small sample we may judge of the whole piece. ”*

---

MIGUEL DE  
CERVANTES-SAAVEDRA  
(1574–1616)

## **Part I**

# **Oscillatory zoning**



# Chapter 1

## Analytical transmission electron microscopy on oscillatory zoned grandite garnets from Oslo rift

### 1.1 Introduction

Oscillatory zoning is a frequently-described phenomenon in grandite (grossular  $\text{Ca}_3\text{Al}_2\text{Si}_3\text{O}_{12}$ -andradite  $\text{Ca}_3\text{Fe}_2\text{Si}_3\text{O}_{12}$ ) garnets (Ivanova *et al.*, 1998) as well as in a wide range of minerals from very different geological environments (Shore & Fowler, 1996). These hydrothermally grown garnets show often complex, oscillatory chemical zonation patterns chiefly perpendicular to the dodecahedral crystal faces  $\{110\}$  and involve changes of the  $\text{Fe}^{3+}/\text{Al}$  ratio as well as variation of the trace element concentrations (Jamtveit *et al.*, 1993). The hypotheses presented about the origin of these oscillatory compositional zonations range between two extremes: from the effect of large-scale processes (external dynamics), to pattern formation caused by self-organisation of the local growth process (internal dynamics; see Shore & Fowler, 1996, for review).

According to Jamtveit *et al.* (1995) the large scale zonation patterns in grandite garnets are assumed to represent changes in external parameters, such as temperature,  $f_{\text{O}_2}$ , pH and salinity. These changes affect the aqueous speciation of Fe and Al and behave like an external template reflecting near-equilibrium conditions. Variations in fluid flow velocity can cause significant kinetic dispersion, i.e. a gradient within the fluid with respect to the  $\text{Fe}^{3+}/\text{Al}$  ratio. Furthermore, widespread intercrystalline correlation among zoning patterns of neighbouring garnets is usually thought to be an indicator for externally controlled growth conditions.

However, there is also evidence from morphological instabilities for a fast, partially locally-controlled crystal growth process (Jamtveit & Anderson, 1992) driven by a fluid flow event, which may result in a far-from-equilibrium state and a significant supersaturation. This may lead to non-linear dynamics involving a coupling between solid and fluid composition, and the oscillations may be an example of chemical self-organisation (e.g., Ortoleva *et al.*, 1987).

Commonly, oscillatory zoning is interpreted as a primary growth-texture and a zonation profile can be thought to correspond to a (growth velocity dependent) time series. Therefore, the limitations in spatial resolution of micro-analytical techniques represent the threshold to the description of the exact zoning pattern and to the quality of growth models, especially if the zoning occurs at a very fine scale. Using transmission electron microscopy (TEM) Reeder & Prosky (1986) observed compositional sector zoning in oscillatory zoned dolomite crystals on the scale of tens of nanometres, a scale that is far beyond the resolution of electron microprobe analyses. Furthermore, recently, Ivanova *et al.* (1998) revealed structural inhomogeneity, explained as superfine oscillatory zoning, in birefringent grandite garnets on the scale of tens of nanometres using diffraction peak profile analysis. The grandites from the Oslo rift show oscillatory zoning with a wavelength of  $< 1 \mu\text{m}$ , which is also too small to resolve with EMP-measurements without interference from adjacent zones.

Therefore, in this chapter we present microstructural investigations and microanalytical measurements by analytical transmission electron microscopy (ATEM) of these oscillatory zoned garnets to provide additional information on the nature of the compositional interfaces at the nanometre scale and to determine how the lattice mismatch resulting from the change in composition is accommodated.

Another aim was to clarify the cause of the optical anisotropy generally associated with chemical zonation in grandite with intermediate composition. The following hypotheses have been proposed for the cause of the anisotropy: (1) the presence of OH groups distributed in a non-cubic manner (Rossman & Aines, 1986; Allen & Buseck, 1988), (2) ordering of Al and  $\text{Fe}^{3+}$  on the octahedral sites (Takéuchi *et al.*, 1982; Allen & Buseck, 1988; Kingma & Downs, 1989; Shtukenberg *et al.*, 2001b), and (3) strain from lattice mismatch at compositional boundaries (Lessing & Standish, 1973; Kitamura & Komatsu, 1978).

## 1.2 Sample and experimental

The zoned grandite garnets originate from skarns of the Oslo region, southern Norway, and have been previously described in a number of papers (Jamtveit, 1991; Jamtveit & Anderson, 1992; Jamtveit *et al.*, 1993; Jamtveit & Hervig, 1994; Jamtveit *et al.*, 1995). The samples used for this study were all of euhedral andradite-rich garnets with dodecahedral crystal form, and representative microprobe analyses were given by Jamtveit *et al.* (1995) and in Table 1.1. The compositional variation can be described as an almost binary mixture of grossular and andradite with minor amounts of spessartine ( $\text{Mn}_3\text{Al}_2\text{Si}_3\text{O}_{12}$ ) and hydrogarnet [ $\text{Ca}_3(\text{Fe}, \text{Al})_2(\text{OH})_{12}$ ]. Therefore the composition given as the mole fraction of andradite  $X_{\text{and}}$  refers to  $X_{(\text{Fe}/[\text{Fe}+\text{Al}])}$ .

Garnet crystals were selected for the study after examination of doubly polished thin sections by optical and scanning electron microscopy. A part of a crystal was selected for electron microprobe analysis (JEOL JXA 8600 Superprobe) at  $1\ \mu\text{m}$  steps along a line approximately perpendicular to the zoning (accelerating voltage 15 kV, beam current 15 nA), using both natural and synthetic standards. Special care was taken to correlate the position of this profile with subsequent ATEM analysis. Part of the thin section containing the line profile was removed using a 3 mm diameter hollow ultrasonic drill. All samples were prepared for TEM by ion beam thinning with Ar ions (5 kV, 1 mA,  $14^\circ$  to the sample surface) using a Gatan Duomill 600. In the following, compositions are given with superscripts identifying the technique used ( $X_{\text{and}}^{\text{EMP}}$  or  $X_{\text{and}}^{\text{ATEM}}$ ).

The electron microprobe analysis (Fig. 1.1) shows a strong correlation between birefringence and composition. Isotropic zones have a composition close to pure andradite ( $X_{\text{and}}^{\text{EMP}} = 0.95 - 1$ ) whereas anisotropic zones reflect a more intermediate composition ( $X_{\text{and}}^{\text{EMP}} = 0.60 - 0.75$ ). The back-scattered electron image shows average atomic number contrast and so the contrast is reversed relative to the optical image. In the thinned sample correlation with the polished section studied by microprobe was made by photographing the positions of holes in the sample relative to the original thin section. Although the edges around the holes were too thin to display birefringence, the boundaries of different zones could be traced visually from thicker regions.

ATEM was performed using a 300 kV JEOL 3010 with a  $\text{LaB}_6$  cathode and equipped with an Oxford Link Isis 300 System for energy dispersive X-ray analysis. Crystals were oriented for electron diffraction and imaging using a double-tilt sample holder and quantitative EDX-analyses were carried out in EDS-mode. X-rays were collected using a [Si(Li)]-detector with

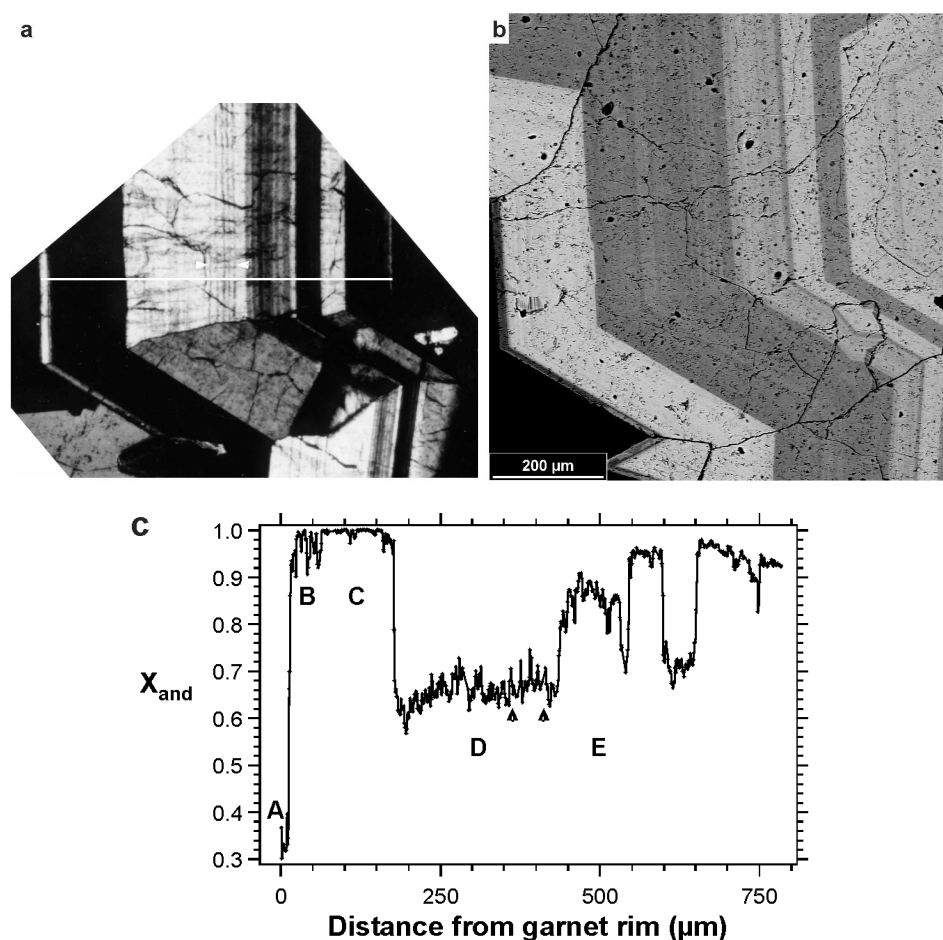


Figure 1.1: **a** Optical micrograph (crossed polars) of an oscillatory zoned garnet showing alternating birefringent and isotropic zones. The zonation is parallel to the  $\{110\}$  growth face. *Arrows* mark thin isotropic zones that cannot be resolved in the EMP profile. **b** Backscattered electron (BSE) image. Not the reversed contrast relative to the optical image. **c** EMP profile. The birefringence is clearly correlated with the composition. Fluctuation in composition occur in region of fine oscillatory zoning.

a  $17.81^\circ$  take-off angle and an ultra-thin window, which allowed us to also analyse oxygen. Atomic percentages were calculated by the Link Isis data acquisition and processing system using experimental  $k$ -factors.

### 1.2.1 Spatial and 'chemical' resolution of ATEM

Although it is possible to generate a beam diameter of 1 nm, the number of X-ray counts in peaks relevant to determine the compositional change ( $\text{Al} \rightleftharpoons \text{Fe}^{3+}$ ) would be too low, because Al and Fe form just 10 at% of the garnet



composition and the Al-peak disappears towards an andradite-rich composition. As the time to collect an EDX-spectrum cannot be increased (because of contamination, amorphisation, etc.) a compromise has to be made between spatial resolution and accuracy. For EDX-analyses we used a beam diameter of 10-15 nm, 60 s lifetime and a specimen of  $\approx 100$  nm thickness. The absorption correction scheme of Van Cappellen & Doukhan (1994) was used. As explained by Klein *et al.* (1997) the spatial resolution of an analysis of a compositional lamellar microstructure can be strongly affected by the orientation of the interfaces to the beam. For a  $10^\circ$  tilt of the interfaces to the beam we calculate a spatial resolution without interference from adjacent microstructure of about 30 nm. The effect of beam broadening is small because of the relative large beam diameter and the high accelerating voltage.

## 1.3 Results

### 1.3.1 Microstructural observations and microstructure-composition relationships

TEM bright-field images within optically anisotropic zones ( $X_{and}^{EMP} = 0.60-0.75$ ) show generally parallel lamellae with a width varying from  $\simeq 10$  to more than 500 nm occurring in both periodic and non-periodic sequences (Fig. 1.2). The interfaces of the lamellae are oriented perpendicular to  $\langle 110 \rangle$ , as determined from selected-area electron diffraction (SAED) patterns and stereographic methods. An EDX line scan (Fig. 1.3) reveals compositional differences of adjacent lamellae alternating from  $X_{and}^{ATEM} = 0.75$  to nearly  $X_{and}^{ATEM} = 1$ . Systematic measurements on a number of lamellae in different birefringent zones and different samples gave an almost bimodal distribution in composition of  $X_{and}^{ATEM} = 0.55 - 0.75$  and  $X_{and}^{ATEM} = 0.95 - 1$ , respectively (Table 1.1). The whole range for the intermediate composition is not realised in one particular area (see Fig. 1.1), but is measured in different areas within the same birefringent zone as well as in different birefringent zones. The bimodal compositional distribution of the lamellae puts constraints on the relative volume filled by each composition as it has to match the composition measured with EMP. Consistently the lowest andradite content ( $X_{and}^{ATEM} = 0.55$ ) was measured in areas where EMP-analyses gave compositions of  $X_{and}^{ATEM} = 0.60 - 0.65$ .

Measurements were carried out in a standardised orientation where the interfaces were tilted  $\simeq 10^\circ$  to the beam because the diffraction contrast in zone axis masks the lamellae, and strong diffraction conditions can influ-

Table 1.1: Electron microprobe (EMP) and analytical transmission electron microscopy (ATEM) data for oscillatory zoned grandite.

	ATEM																
	EMP			Isotropic zone						Lamellae within a birefringent zone			Andradite-rich				
	Birefringent			Intermediate composition						Andradite-rich							
	SiO <sub>2</sub>	36.51	36.36	36.73	36.61	35.58	35.05	34.98	38.69	38.03	37.70	37.47	37.06	38.10	36.87	36.67	33.59
CaO	33.40	33.82	33.92	33.68	33.36	32.63	31.24	33.87	33.92	32.79	32.17	32.12	32.36	33.51	32.72	31.65	32.98
MnO	0.63	0.59	0.48	0.46	0.44	0.37	1.80	0.15	0.50	0.34	0.64	0.75	0.52	0.69	0.26	0.48	0.50
Fe <sub>2</sub> O <sub>3</sub>	20.02	21.46	21.92	22.90	23.93	29.73	30.87	17.99	19.19	21.01	21.65	22.66	22.52	23.91	29.35	33.88	31.59
Al <sub>2</sub> O <sub>3</sub>	8.36	6.96	6.86	6.34	5.17	1.08	0.03	9.31	8.36	8.16	8.08	7.42	6.51	5.03	1.00	0.40	0.14
MgO	<i>b.d.</i>	0.01	<i>b.d.</i>	0.02	0.02	0.07	0.11	<i>n.a.</i>	<i>n.a.</i>	<i>n.a.</i>	<i>n.a.</i>	<i>n.a.</i>	<i>n.a.</i>	<i>n.a.</i>	<i>n.a.</i>	<i>n.a.</i>	<i>n.a.</i>
TiO <sub>2</sub>	<i>b.d.</i>	0.01	0.04	<i>b.d.</i>	0.02	<i>b.d.</i>	<i>b.d.</i>	<i>n.a.</i>	<i>n.a.</i>	<i>n.a.</i>	<i>n.a.</i>	<i>n.a.</i>	<i>n.a.</i>	<i>n.a.</i>	<i>n.a.</i>	<i>n.a.</i>	<i>n.a.</i>
Total	98.92	99.20	99.95	99.99	98.52	98.93	99.03	100.00	100.00	100.00	100.00	100.00	100.00	100.00	100.00	100.00	100.00
	Formula on the basis of 8 cations and 12 oxygen																
Si	2.988	2.985	2.996	2.995	2.971	2.981	2.996	3.10	3.07	3.09	3.07	3.05	3.13	3.05	3.03	2.87	2.97
Ca	2.929	2.974	2.964	2.951	2.984	2.973	2.867	2.91	2.93	2.88	2.83	2.83	2.85	2.97	2.90	2.90	3.01
Mn	0.044	0.041	0.033	0.032	0.031	0.027	0.131	0.01	0.03	0.02	0.04	0.05	0.04	0.05	0.02	0.03	0.04
Fe <sup>3+</sup>	1.233	1.326	1.346	1.409	1.503	1.902	1.990	1.09	1.16	1.29	1.34	1.40	1.39	1.49	1.83	2.18	2.03
Al	0.807	0.674	0.659	0.611	0.508	0.108	0.003	0.88	0.79	0.79	0.78	0.72	0.63	0.49	0.10	0.04	0.01
Mg		0.001		0.002	0.002	0.008	0.014										
Ti		0.000	0.003		0.001												
Sum	8.001	8.001	8.001	7.998	8.000	7.999	8.001	7.99	7.98	8.07	8.06	8.05	8.04	8.05	7.87	8.03	8.06
X <sub>and</sub>	0.60	0.66	0.67	0.70	0.75	0.95	1.00	0.55	0.59	0.62	0.63	0.66	0.69	0.75	0.95	0.98	1.00

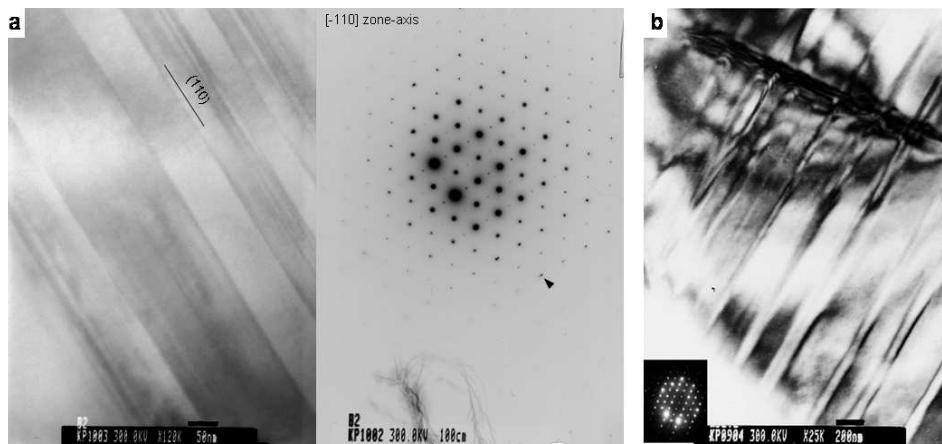


Figure 1.2: **a** Transmission electron micrograph and its diffraction pattern showing very fine, non-periodic lamellae with interfaces perpendicular to (1 1 0) and as a result small peak splitting (*arrows*). **b** Transmission electron micrograph with periodic lamellar microstructure. The apparent needle shape of the lamellae is a consequence of the diffraction condition when the interfaces are not orientated parallel to the beam (zone axis [2 1 0]).

ence the measured composition (Borrmann effect). Therefore, the spatial resolution of the analyses was limited to 30 nm at best. The high-resolution image (Fig. 1.4) proves the sharpness of the compositional interfaces and shows a completely coherent interface that is only noticeable by the diffraction contrast superimposed on this image because of a small objective aperture. Although the lamellae consist of two discrete phases with an almost bimodal composition, the difference in the diffraction contrast (defining the diffraction contours) between them is low because the structure factors are very similar, the orientation is identical, and the change in lattice parameters (calculated  $\Delta a \simeq 0.08 \text{ \AA}$ ) does not result in interface imperfection. Lamellae can be observed best by looking at the small bending of the diffraction contrast at the interface during tilting the crystal.

The compositions of the finest lamellae (<50 nm) are thought to have the same compositional distribution as the larger one because the diffraction contrast is very similar. EDX-analyses of small lamellae consistently appear to lie between the two extremes (with  $X_{and}^{ATEM} = 0.80 - 0.85$ ), which shows the mixing effect of analysing adjacent lamellae of different composition.

Diffraction patterns show no measurable deviation from cubic symmetry in the optically anisotropic regions. Areas of very fine lamellar inter-

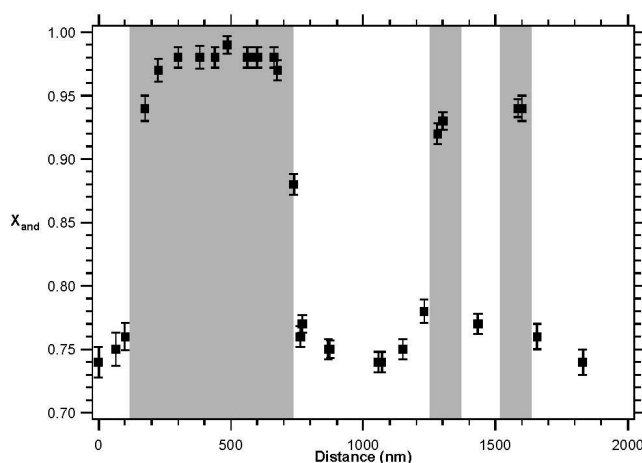
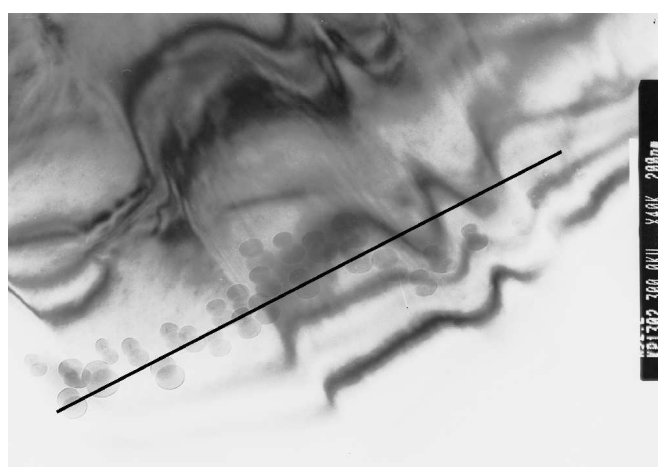


Figure 1.3: Transmission electron micrograph with EDX line scan showing bimodal distribution of the composition. The diffraction contours indicate the compositional changes. Note the contamination spots, which can be used for rough thickness determination. Image is taken in non-zone axis orientation.

growth show a small streaking at diffraction spots of high indices perpendicular to the interfaces. This is interpreted as a shape effect.

Parts of the specimen without a lamellar microstructure show no characteristic Al-peak in the EDX-spectra and can consistently be related to optically isotropic zones.

### 1.3.2 Correlation of ATEM observations to the EMP-profile

Part A of the EMP-profile (Fig. 1.1) shows a very grossular-rich composition, which has been grown in the latest stage of crystallisation. In this region we found a lamellar microstructure similar to other anisotropic zones with lamellar compositions of  $X_{and}^{ATEM} = 0.15$  and  $X_{and}^{ATEM} = 0.51$ , respectively, and also lamellae with a composition close to the 'bulk' composition of this zone ( $X_{and}^{ATEM} = 0.38$ ). Because of the small size of this zone

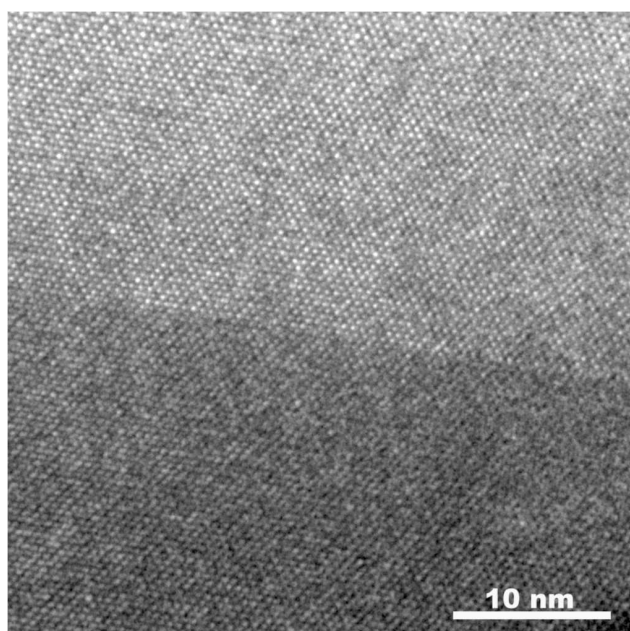


Figure 1.4: High resolution transmission electron micrograph of the compositional interface  $\{110\}$ . The interface is only visible because most beams have been excluded using a small objective aperture to superimpose diffraction contrast. Note the coherency of the interface.

it was not possible to evaluate whether there is a bimodal distribution of a grossular-rich and an intermediate composition or whether the lamellar compositions are distributed over a broader range.

Although part B of the EMP-profile is optically nearly isotropic we found a microstructure with very fine lamellae (10–50 nm) of intermediate composition ( $X_{and}^{ATEM} = 0.55 - 0.75$ ) in a host of broader lamellae with andradite-rich composition ( $X_{and}^{ATEM} = 0.95 - 1.0$ ). This observation explains the compositional fluctuation in this part measured by EMP, which averages over these heterogeneities. Part C is a very homogeneous zone of nearly pure andradite without a significant microstructure.

The parts D and E show pervasive lamellae covering the whole range of lamellar width, which reconfirmed the compositional fluctuation in EMP-analyses. A further analytical correlation of the EMP-profiles with ATEM was limited because of the limited number of thin areas in the sample.

SAED shows that the compositional interfaces in the EMP-profile form an angle of about  $20^\circ$  to the beam. Therefore, the spatial resolution of the EMP is limited to about  $2.5 - 3 \mu\text{m}$  solely because of orientation of the heterogeneities. In comparison, the interfaces of the adjacent growth sector are nearly parallel to the electron beam, hence the spatial resolution would be determined by the excited volume. As a consequence, optically visible isotropic lamellae within an anisotropic zone with a width of  $\approx 1 \mu\text{m}$  cannot be resolved by the EMP-analyses and appear as compositional ‘peaks’ within the intermediate composition (arrows in Fig. 1.1 a, c). All kinds of

compositional fluctuations turn out to mark areas of heterogeneous composition and can be easily overlooked by the use of wider steps or large beam diameter in microprobe line scans.

## 1.4 Discussion

### 1.4.1 Microstructure and oscillatory zoning

The observed microstructure is interpreted as originating from and preserved after the crystal growth process. The maximum temperature of formation for the garnet-bearing skarn caused by fluid-infiltration was estimated to be  $\sim 400^\circ\text{C}$  (Jamtveit *et al.*, 1992), too low a temperature for solid state diffusion to obliterate or significantly reorganise the compositional gradients, even on a geological time-scale. The lamellae are perpendicular to the  $[110]$  growth direction of the garnets and represent oscillatory zoning at a very fine scale.

Hirai & Nakazawa (1986) reported a compositional lamellar microstructure with a width of 180–750 nm in an iridescent grandite. Although the description of the microstructure is very similar to our investigation, these authors favoured exsolution forced by subsolidus decomposition instead of oscillatory zoning, because of the regular spacing of the lamellae and the supposed sharpness of the interface. This argument seems to be unlikely, at least for our samples, as miscibility gaps in the grossular-andradite join that could drive exsolution are uncertain, especially for andradite-rich compositions, and would surely occur at fairly low temperatures ( $<500^\circ\text{C}$ ) where the kinetics would be sluggish. Recent calculation on the mixing behaviour of the grossular-andradite binary, based on empirical potentials and Monte-Carlo simulations, would completely rule out exsolution and ordering because of the very low starting temperatures for these processes (see chapter 2).

Ivanova *et al.* (1998) described, from X-ray peak profile analysis of grandites with grossular-rich to intermediate composition, an inhomogeneous structure with lamellae along the  $[110]$  direction varying in width from  $<20$  to  $>100$  nm within one birefringent zone. They proposed the composition of the lamellae to span a broad range from pure grossular to andradite-rich compositions by modelling of the diffraction profiles. Their structural findings are in excellent agreement with our observations showing that oscillatory zoning at the nanometre-scale might be rather the rule than the exception in birefringent zones of zoned grandite garnets. This seems to be further confirmed by the available data on compositional zon-

ing in grandites summarised by Ivanova *et al.* (1998). The minimum thickness of the zones in nearly all studies is reported to be below the spatial resolution of the EMP ( $\approx 1\text{--}3\ \mu\text{m}$ ). It is also conspicuous that the compositions of optically birefringent and isotropic zones often fall in the ranges  $X_{\text{and}}^{\text{EMP}} \approx 0.5\text{--}0.7$  and  $X_{\text{and}}^{\text{EMP}} \approx 0.9\text{--}1$  respectively, similar to our samples. The compositional bimodality observed in our ATEM study should therefore be proved on other samples from different localities as well as on other grandite 'bulk' compositions to deduce similarities of the growth mechanisms.

Jamtveit (1991) used the proposed (and disputed) miscibility gaps to model qualitatively non-periodic oscillatory zonation patterns with bimodal compositions using a set of non-linear equations. An important point of this model is the inclusion of a dampening term that takes into account strain resulting from lattice mismatch at the compositional interfaces. This dampening term can be considered as an activation energy (here: interface energy), which is necessary to switch from one to the next growing composition. The interfaces are observed to be coherent and sharp within one unit cell periodicity. The calculated lattice mismatch for the analysed compositions would be  $\approx 0.08\ \text{\AA}$  and the interface cannot be localised without superimposed diffraction contrast. This is done by using a small objective aperture (just a few diffracted beams contribute to the image), which lowers the spatial resolution significantly. Therefore, the amount of strain at the interfaces may only be noticeable by its effect on the optical properties. However, there are several reasons that can cause anisotropy in grandite garnets (see section 1.4.2).

Furthermore, the lattice mismatch could be partly balanced by the incorporation of trace elements that are correlated with the intermediate (Mn) and the andradite-rich composition (As, W), or different amounts of water in the structure caused by the hydrogarnet substitution ( $\text{Si}^{4+} \rightleftharpoons 4\text{H}^+$ ).

As the fine zonation is interpreted as a crystal growth phenomenon the growth velocity is an important factor in deciding between locally controlled processes (internal dynamics) and external forcing caused by large scale processes. However, constraints on the growth velocity of crystals in hydrothermal systems are rare. Jamtveit *et al.* (1995) deduced the minimum growth velocity for garnet growth that could produce variable concentration gradients near the garnet-fluid interface to  $10^{-11}\ \text{m/s}$  ( $\approx 1\ \mu\text{m}/\text{day}$ ) in a porous environment. In addition, occasionally formed morphological instabilities observed in andradite-rich garnets from the same locality (Jamtveit & Anderson, 1992) indicate moderately high growth velocities. Assuming a constant growth velocity of  $10^{-11}\ \text{m/s}$  a compositionally ho-

mogeneous lamella of 50 nm within a birefringent zone would grow in  $1\frac{1}{2}$  h. In contrast the wider andradite-rich isotropic zones, which can have a thickness of tens of micrometres would grow in about 1 month (calculated for 25  $\mu\text{m}$ ). An external template explaining the whole zonation pattern must therefore in this case act over a longer period and show oscillations in one or more parameters with uniform extent on a short time-scale. Naturally the growth velocity is not constant, but will be affected by both internal and external processes. Internally controlled growth velocity depends on the supersaturation and hence on the relation between solid solution and aqueous solution composition, that is, the actual distribution coefficient (Prieto *et al.*, 1993). External processes can change the overall fluid composition (e.g. by fluid mixing) as well as affect the Al-Fe fractionation between the aqueous solution and the garnet by changes in temperature, pH,  $f_{\text{O}_2}$  and salinity. Furthermore rapid fluid flow can lead to kinetic dispersion, which results in a Fe/Al ratio at the growing crystal deviating from the overall fluid composition (Jamtveit *et al.*, 1995).

In the case of just one underlying process (internal or external), changes in growth velocity should correspond to the actual growing composition. Because bimodality in composition is observed at different scales, changes in growth velocity would consequently have to occur at different time scales, and the underlying process has to act in a uniform way over these time scales. This seems to be unlikely at least solely for changes in external parameters.

Statistical analyses of zoning patterns from garnets and other minerals based on microprobe profiles and digitalised back-scattered electron (BSE) images have shown scale invariance, which can be described in terms of power law scaling and self-affine fractal geometry (Holten *et al.*, 1997). A self affine fractal (in contrast to a self-similar fractal) scales differently in different directions, which is always the case when directions have a different physical meaning (units), for instance spatial units and composition. Their study suggests that an increase/decrease in composition in one space step favours a decrease/increase in the next step, which is indicated by anti-persistent statistics. TEM cannot provide a full zoning pattern profile over an adequate length scale and a bias towards the selection of interesting parts would be unavoidable by measuring parts of the pattern at different magnification (Meakin, 1998). However, the large compositional changes at the nanometre-scale limit the application of statistical methods. These changes cannot be analysed by fractal geometry because the composition are strongly bounded as a result of the compositional bimodality and fill



out the whole compositional range within the narrowest spatial step (see section 1.7).

The resolution limit (spatial/chemical) of the applied technique is of prime importance for analysing the fractal dimension, and detecting the 'real' zonation pattern is a prerequisite for further modelling. Averaging over an inhomogeneous or finely zoned part leads to a smoothed zonation pattern, which, when analysed with statistical methods, may give misleading fractal characteristics especially when the real composition is much more bounded or even bimodally distributed (see also section 1.7). For the grandite garnets studied here, the conclusion that power law scaling implies just one underlying growth process cannot hold.

The sharpness and coherence of the compositional interfaces and their planar form constrain the underlying crystal growth process(es) to be uninterrupted, but also lead to frequent changes in crystal composition. This rules out episodic flow of fluid with hiatuses or even dissolution in the growth history of nanometre-scale lamellae. The high frequency and partial periodicity of lamellae controlled externally would require a highly dynamic hydrothermal system with also frequent (periodic) changes in one or more parameters of definite extent. From this we suggest that nanometre-scale oscillatory zoning in grandites is much more likely to be controlled by local growth dynamics than by an external template.

On the basis of the provided data we suggest a possible, but simplified outline for the growth process of oscillatory zoned grandite garnets. The Al concentration in the fluid phase is thought to be mainly controlled by the dissolution of Al-bearing minerals, whereas the Fe concentration is controlled by the fluid influx (Jamtveit *et al.*, 1993). In andradite-rich parts, the rate of fluid infiltration is high and keeps the fluid saturated with respect to an andradite-rich garnet composition. At this stage the growth rate is assumed to be high, causing morphological instabilities (Jamtveit & Anderson, 1992) and dissolution of Al-bearing minerals is a negligible contribution to the fluid composition in relation to the fluid influx. As the fluid flow rate drops, the growth rate decreases and the dissolution of Al-bearing minerals becomes important in determining the fluid composition. A coupling of dissolution rate, the transport of Al to the growing interfaces and a compositional threshold that causes the transition of the growing composition may provide a possible feedback mechanism for a self-organisation growth process (e.g. Ortoleva *et al.*, 1987) that produces the very fine oscillatory zoning observed with TEM. As the fluid infiltration increases again, this coupling will be destroyed and an andradite-rich composition grows again. Therefore, the major changes in growth composition from larger

birefringent to isotropic zones, also shown as intercrystalline correlation, could reflect external changes, most probably in fluid flow, whereas the growth of principally birefringent zones is thought to be strongly affected by internal growth dynamics. The length scale at which a transition from external to internal controlled zoning pattern probably occurs, cannot be deduced from this simple outline. Moreover, an interaction of both mechanisms can be expected. However, Holten *et al.* (2000) showed recently that by adding small external fluctuation (e.g. noise) to non-linear growth models that generate oscillatory zoning, the resultant correlation of zoning patterns of neighbouring mineral grains does not necessarily imply an externally controlled growth process, but may result from synchronisation even when the growth process is driven by highly non-linear dynamics.

#### 1.4.2 Microstructure and birefringence

Various hypotheses have been proposed to explain the birefringence in grandite garnets and we will discuss the three most probable points in relation to the microstructure observed in our samples: (1) the presence of OH<sup>-</sup> groups distributed in a non-cubic manner (Rossman & Aines, 1986; Allen & Buseck, 1988), (2) ordering of Al and Fe<sup>3+</sup> on the octahedral sites (Takéuchi *et al.*, 1982; Allen & Buseck, 1988; Kingma & Downs, 1989; Shtukenberg *et al.*, 2001b), and (3) strain from lattice mismatch at compositional boundaries (Lessing & Standish, 1973; Kitamura & Komatsu, 1978).

The incorporation of OH<sup>-</sup> was stated above as one possibility to accommodate the changes in lattice parameter at compositional interfaces. To make this factor responsible for the observed birefringence in areas with intermediate composition, a strong correlation of the incorporation of water and the growing composition at all scales must be present, which seems to be unlikely.

The existence of an order-disorder phase transition caused by ordering on octahedral sites would lead to quite a few possible twin laws as every symmetry operation that is lost may act as a twin operation (Takéuchi *et al.*, 1982; Hatch & Griffin, 1989). But, no twins were observed in any of our samples. In addition, the energetics of cation ordering have been calculated using empirical potentials (see Chapter 2) and it can be concluded that there is a tendency to order, but that long-range order in grandite would only become stable at very low temperatures (<50 °C). Such a temperature would completely discount cation ordering after growth. Thus, if symmetry reduction caused by ordering is the reason for the birefringence it only could have taken place metastably during the crystal growth process

as suggested by Gali (1983) and Akizuki (1984). However, during growth under metastable conditions the kinetics tends to favour the growth of disordered rather than ordered structures, even if the latter are stable (Carpenter & Putnis, 1985). Furthermore, McAloon & Hofmeister (1993) found no evidence for a symmetry reduction to a non-cubic space-group by infrared spectroscopy of birefringent grandites that were described as ordered.

Regular spacing of lamellae of about 100-1,000 nm with distinct compositions were found to produce iridescence and was always accompanied by birefringence (e.g. Akizuki *et al.*, 1984; Hirai & Nakazawa, 1986). In our samples the birefringence was clearly associated with the lamellar microstructure, which consists of a large number of compositional interfaces. Furthermore, regions with lamellar microstructure can always be correlated to optical textures and growth features of oscillatory zoned grandite crystals (Akizuki, 1984; Jamtveit & Anderson, 1992; Badar & Akizuki, 1997). Recently, Shtukenberg *et al.* (2001a) studied optical anomalies of alums grown under various conditions and stated that the results are also applicable to the grandite binary. According to these authors the anomalous birefringence is a superposition of mismatch strain, strain along dislocations (rarely observed in this study) and growth ordering of isomorphous components, which are all sensitive to variation in growth conditions and the relief of the growing face. These effects seem to give a comprehensive explanation for the appearance of birefringence associated with intermediate compositions grown under dynamic conditions.

## 1.5 Conclusion

Oscillatory zoning of grandite garnets down to the nanometre scale was directly observed and quantitatively analysed for the first time. A transition from one composition to the next takes place within one unit cell periodicity reflecting dynamical, but non-transient growth conditions. Compositional bimodality of andradite and an intermediate composition on a small scale accounts for growth conditions far from equilibrium at moderate growth rate. The significance of the specific compositions at different scales and the underlying driving forces within the grandite binary are still not clearly understood.

To determine the minimum scale of oscillatory zoning within a mineral and thus the 'real' zoning pattern is a prerequisite for successful modelling of the growth conditions and the underlying processes (external/internal). Therefore, the spatial resolution of the applied analytical technique is a cru-

cial parameter and insufficient resolution can lead to misleading interpretation of the data. Hence, further studies on oscillatory zoned garnets and other minerals covering the important nanometre scale are required to get a further insight into the common properties and the differences of this phenomenon in different geological environments.

# Supplemental material to chapter 1

## 1.6 Analysis of grossular-rich oscillatory zoned grandites from Oslo rift area

Oscillatory zoning patterns of grandite garnets with andradite-rich composition have been described in Chapter 1. In the same skarn locality (Oslo region, southern Norway), grandite garnets with a high grossular content are also common (Jamtveit, 1991). These grandites show a correlation between birefringence and composition as well but are generally smaller than the andradite-rich ones. Zones with compositions of  $X_{and}^{EMP} = 0.10 - 0.20$  are weakly birefringent whereas zones with compositions of  $X_{and}^{EMP} = 0.30 - 0.50$  are generally strong birefringent (cf. Fig. 1.5 and Table 1.2). In contrast to the andradite-rich samples, both weak and strong birefringent zones cover a broader range of compositions and the variations in composition are generally smaller than for andradite-rich samples. Nevertheless, discrete zones are clearly defined to a wavelength of  $\approx 1 \mu\text{m}$ . The smaller size of the grossular-rich garnets correspond to the findings of Heuss-Aßpichler & Fehr (1997) from synthesis experiments. These authors reported much smaller grain sizes ( $\approx 15 \mu\text{m}$ ) for intermediate grandite compositions compared to  $80 \mu\text{m}$  and  $180 \mu\text{m}$  for grossular and andradite, respectively.

A limited study on these samples were conducted to answer various additional questions: Do the grossular-rich samples also show oscillatory zoning on the nanometre scale? If there, is the oscillatory zoning bimodal as for the andradite-rich samples? What are the compositional boundaries and do they show any agreement to the calculated miscibility gaps of the grandite solid solution presented in chapter 2? The experimental details of the sample preparation and analysis are the same as given in section 1.2.

Table 1.2: Electron microprobe (EMP) and analytical transmission electron microscopy (ATEM) data for oscillatory zoned grossular-rich garnets.

	EMP				ATEM											
	weak birefringence		strong birefringence		Lamellae within birefringent zones											
					Grossular-rich		Intermediate I		Intermediate II							
SiO <sub>2</sub>	37.68	38.36	38.15	38.07	38.02	38.11	37.14	36.31	40.01	39.65	40.15	40.03	39.07	38.92	38.49	38.33
CaO	35.95	36.04	34.86	35.83	35.83	35.38	35.66	35.41	35.67	35.35	34.64	34.50	35.29	33.84	33.55	34.88
MnO	1.52	0.84	0.87	0.21	0.14	0.18	0.09	<i>b.d.</i>	0.19	0.18	0.15	0.18	0.21	0.18	0.30	0.03
Fe <sub>2</sub> O <sub>3</sub>	4.05	5.51	6.68	9.57	10.55	11.95	14.17	15.14	3.91	5.51	9.28	9.82	10.56	13.97	15.49	15.64
Al <sub>2</sub> O <sub>3</sub>	19.62	18.66	17.91	15.08	15.08	14.32	12.14	11.84	20.22	19.31	15.78	15.47	14.87	13.10	12.17	11.12
MgO	<i>b.d.</i>	<i>b.d.</i>	<i>b.d.</i>	<i>b.d.</i>	0.02	0.02	0.03	0.03	<i>n.a.</i>	<i>n.a.</i>	<i>n.a.</i>	<i>n.a.</i>	<i>n.a.</i>	<i>n.a.</i>	<i>n.a.</i>	<i>n.a.</i>
TiO <sub>2</sub>	0.55	0.51	0.49	0.08	0.39	0.03	0.39	0.49	<i>n.a.</i>	<i>n.a.</i>	<i>n.a.</i>	<i>n.a.</i>	<i>n.a.</i>	<i>n.a.</i>	<i>n.a.</i>	<i>n.a.</i>
Total	99.37	99.91	98.98	98.94	100.08	100.02	99.60	99.22	100.00	100.00	100.00	100.00	100.00	100.00	100.00	100.00
Formula on the basis of 8 cations and 12 oxygen																
Si	2.896	2.945	2.971	2.994	2.965	2.986	2.950	2.905	3.04	3.04	3.12	3.10	3.06	3.07	3.06	3.04
Ca	2.961	2.964	2.908	3.019	2.993	2.969	3.035	3.034	2.91	2.91	2.88	2.86	2.96	2.86	2.86	2.97
Mn	0.054	0.057	0.050	0.014	0.009	0.012	0.006	0.099	0.01	0.01	0.01	0.01	0.01	0.01	0.02	0.00
Fe <sup>3+</sup>	0.234	0.319	0.392	0.566	0.619	0.688	0.847	0.911	0.22	0.32	0.54	0.57	0.62	0.83	0.93	0.93
Al	1.777	1.688	1.644	1.397	1.358	1.311	1.137	1.117	1.81	1.75	1.44	1.41	1.37	1.22	1.14	1.04
Mg					0.002	0.002	0.003	0.004								
Ti	0.032	0.030	0.029	0.005	0.023	0.002	0.023	0.030								
Sum	7.999	8.000	8.001	8.001	8.000	8.001	8.001	8.001	8.00	8.02	8.00	7.96	8.03	7.98	8.02	7.98
X <sub>and</sub>	0.12	0.16	0.18	0.29	0.31	0.34	0.43	0.46	0.11	0.15	0.27	0.29	0.31	0.41	0.45	0.47

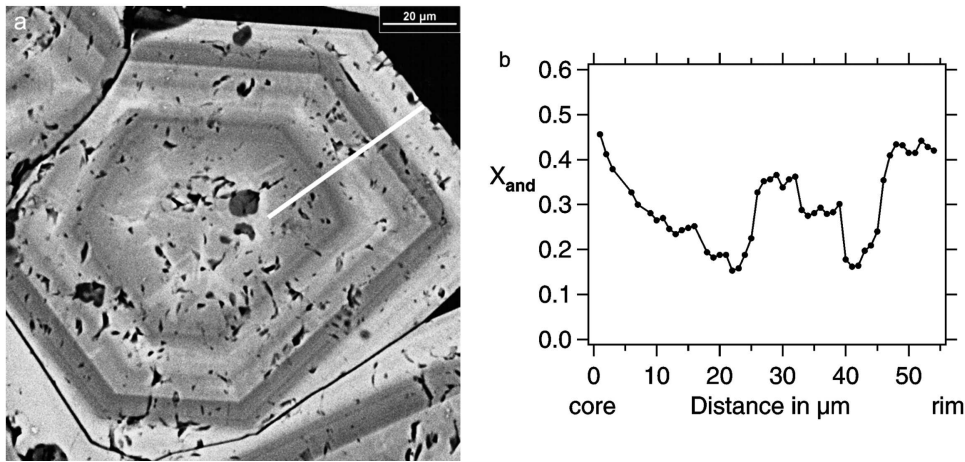


Figure 1.5: **a** BSE image of an idiomorphic, oscillatory zoned garnet with grossular-rich composition. **b** EMP line scan. Step width 1  $\mu\text{m}$ .

### 1.6.1 Results and Discussion

All parts of the grossular-rich samples show a lamellar microstructure in the nanometre range. As for the andradite-rich samples, the interfaces of the lamellae are oriented perpendicular to  $\langle 110 \rangle$ . Pervasive lamellae microstructure was only observed in region of intermediate composition ( $X_{and}^{EMP} = 0.29 - 0.50$ ) which is characterised by strong birefringence. In the EDX line scan of such an area (Fig. 1.6) the composition of adjacent lamellae varies from  $X_{and}^{ATEM} \simeq 0.30$  to  $X_{and}^{ATEM} \simeq 0.46$ . Systematic measurements on discrete lamellae result in two groups of intermediate compositions with  $X_{and}^{ATEM} = 0.27 - 0.31$  and  $X_{and}^{ATEM} = 0.41 - 0.50$ , respectively (Table 1.2). In the grossular-rich, nearly isotropic parts only few lamellae in a homogeneous matrix were observed. The matrix has a composition of  $X_{and}^{ATEM} = 0.10 - 0.15$  whereas the composition of lamellae range from  $X_{and}^{ATEM} \simeq 0.25 - 0.35$ . However, these lamellae are rather small and, thus, their compositions are not well constrained due to the limited spatial resolution of about 30 nm (cf. section 1.2). Fig. 1.7 shows this very fine oscillatory zoning with a width of lamellae of about 10 nm which corresponds to only 10 times the unit cell dimensions.

Comprising, the grossular-rich samples show three distinguishable compositional ranges in the oscillatory zoning on the nanometre scale. However, only two of these compositions occur adjacent to each other, either grossular-rich with the intermediate I or intermediate I with intermediate II (Table 1.2). The latter case is much more pronounced, showing both periodic and non-periodic sequences over longer distances ( $\geq 1 \mu\text{m}$ ). There-

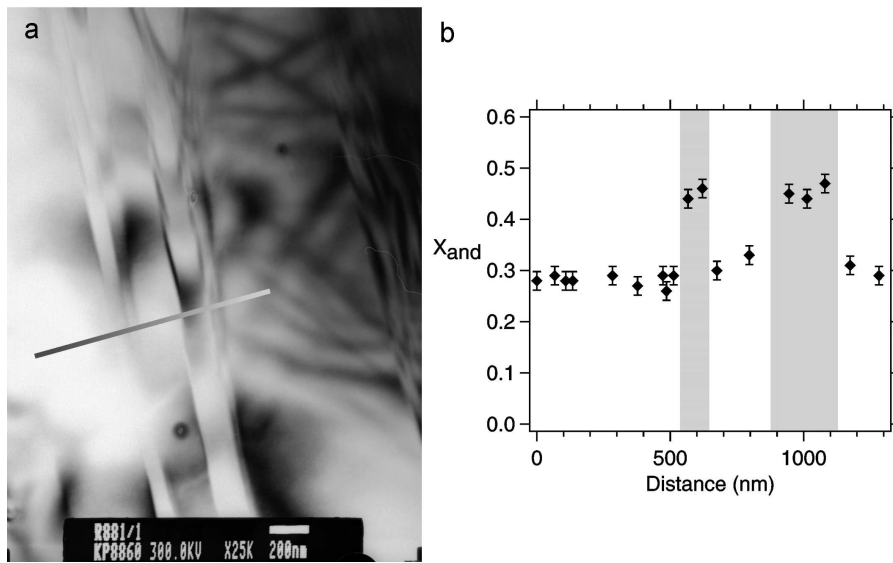


Figure 1.6: **a** Transmission electron micrograph of fine oscillatory zoning in a grossular-rich garnet. The interfaces of the lamellae appear blurred because they are inclined to the beam. **b** EDX line scan on the lamellar microstructure. The analysis have been corrected for differences in sample thickness and have been traced to the line given in **a**

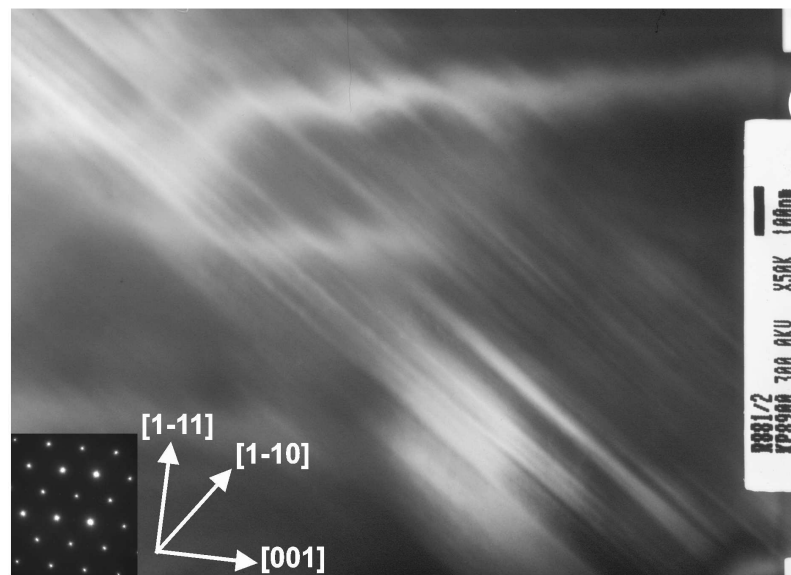


Figure 1.7: Transmission electron micrograph showing a very fine lamellar microstructure. The orientation of the zone axis is  $[1\ 1\ 0]$  and the interfaces of the lamellae are perpendicular to  $[1\ -1\ 0]$  or, more general, perpendicular to  $\langle 1\ 1\ 0 \rangle$ .



fore, the oscillatory zoning in grossular-rich grandite can also be described as bimodal but also as more complex than in the andradite-rich samples. Nevertheless, the ATEM measurements clearly show that the changes in optical properties are coupled with a difference in microstructure for both the andradite-rich and grossular-rich samples.

An important difference between the andradite-rich and the grossular-rich samples concerns the occurrence of small scale zoning and the boundaries of the bimodal compositions. The andradite-rich samples were characterised by alternating isotropic parts with no microstructure ( $X_{and}^{EMP} = 0.95 - 1$ ) and finely zoned birefringent parts ( $X_{and}^{EMP} = 0.60 - 0.75$ ). Only the birefringent parts exhibit adjacent lamellae of intermediate ( $X_{and}^{ATEM} = 0.55 - 0.75$ ) and almost pure andradite composition ( $X_{and}^{ATEM} = 0.95 - 1$ ). In contrast, in the grossular-rich samples compositional oscillations occur in all parts of the crystal but with variable frequency and width of the lamellae and with three different composition ranges. Combining the observed compositional ranges and comparing them with the available thermodynamic data on non-ideal mixing within the grandite binary system (Huckenholz & Fehr, 1982; Engi & Wersin, 1987; Jamtveit, 1991, and chapter 2 of this work) highly questioned the idea of Jamtveit (1991) that possible miscibility gaps control the compositions in the oscillatory zoning pattern. Hence, a combination of kinetic effects and external forcing is favoured. The external forcing is needed to maintain a far from equilibrium situation in which transport and growth kinetics will act.

Possible kinetic effects include variable kinetic dispersion, near-surface processes, and aqueous complexation behaviour (Jamtveit *et al.*, 1995). The variable kinetic dispersion, which is the change of fluid composition as function of the flow velocity, can explain changes of garnet composition in different parts of the skarn as result of e.g. rock porosity. However, as small scale zoning is unlikely to occur by rhythmic changes in the flow velocity, another effect has to be taken into account for the compositional bimodality in the oscillatory zoning patterns. Jamtveit *et al.* (1995) have shown that the Fe–Al fractionation between garnet and hydrothermal solution is very sensitive to variations of temperature, pH,  $f_{O_2}$  and salinity. This sensitivity is due to differences in aqueous complexation behaviour between Al and Fe and might explain why almost all Fe<sup>3+</sup> – Al solid solutions (grandite, alum, epidote, prehnite) commonly show extensive and complex zonation patterns.

## 1.7 Limits of fractal geometry in the analysis of oscillatory zoning patterns

Fractal geometry has been applied to oscillatory zoning patterns (OZP) in a variety of minerals over the last decade (e.g., Halden & Hawthorne, 1993; Halden, 1996; Holten *et al.*, 1997, 1998; Hoskin, 2000; Cortini & Anastasio, 2001; Bryxina *et al.*, 2002) as well as to a wide range of other phenomena in nature (Mandelbrot, 1982; Feder, 1988; Meakin, 1998). The challenge was to describe complex patterns in a statistical and quantitative way from which a deeper understanding of the important parameters or even the underlying mechanism(s) may be gained. These includes especially for OZPs to unravel a possible dependence on either the petrogenetic conditions or the main growth dynamics (internal vs. external). Furthermore, fractal statistic characteristics may act as test for modelled OZPs.

The value of interest to characterise a fractals is the fractal dimension,  $D$ , which is a measure of how much space the fractal fills at different length scales. In geoscience, two types of fractals are of particular importance: self-similar fractals which scale equally (isotropically) in all directions (e.g. coastlines) and self-affine fractals which scale differently in different directions (e.g. annual river outflow, surface roughness) The latter is the case in particular when the directions have different physical dimensions (e.g., for OZP, composition or grey scale on the y-axis versus distance or time on the x-axis).

Quantitative OZPs can be recorded in different ways depending on the nature of zoning. EMP line scans, backscattered electron as well as digitised thin-section images are commonly used (e.g. for grandite garnets; cf. Fig. 1.1). Additionally, proton-induced X-ray emission (PIXE) has been used for plagioclase and agate (Holten *et al.*, 1997; Bryxina *et al.*, 2002). Cathodoluminescence (CL) imaging is the method of choice to study the OZPs of zircon (Halden & Hawthorne, 1993; Hoskin, 2000). The spatial resolution of these analytical techniques is similar (0.5 – 3  $\mu\text{m}$ ).

In this section the significance and limits of fractal geometry characterising OZPs will be discussed. Special emphasis is given to the fact that the oscillations are often in the range or even smaller than the spatial resolution of the applied analytical technique.

### 1.7.1 Fractal statistics: the Hurst exponent

OZPs might be described as a two-dimensional (or more exactly a  $1 + 1$  dimensional) self-affine fractal,  $y(x)$ , which is statistically invariant under

the transformation:

$$\begin{aligned}x &\rightarrow \lambda x \\y &\rightarrow \lambda^H y\end{aligned}\quad (1.1)$$

where  $H$  is the Hurst exponent (or roughness exponent) and  $\lambda$  is a real number. For such a self-affine fractal, the absolute vertical height difference  $\delta y$  between pairs of points separated by a distance  $\delta x$  in the x-direction scales on the average as  $\langle \delta y \rangle \sim (\delta x)^H$  ( $\langle \cdot \cdot \cdot \rangle$  denotes average; Turcotte, 1997). The relationship of  $H$  to the fractal dimension  $D$  is given by:

$$H = 2 - D. \quad (1.2)$$

Fractional Brownian motion (a generalisation of ordinary Brownian motion,  $H = 0.5$ ; Feder, 1988) can be used to visualise differing dimensions of two-dimensional self-affine fractals (Fig. 1.8). A value for  $H > 0.5$  denotes persistent behaviour, i.e., an increasing trend in the past favours an increasing trend in the future and vice versa. Therefore, persistent patterns look smooth with broad peaks. In contrast, anti-persistent patterns ( $H < 0.5$ ) look rough with sharp peak, i.e., a decreasing trend in one increment favours an increasing trend in the next and vice versa.

An important difference between OZPs and fractional Brownian motion is that the zoning patterns have a limited y-scale. The composition of the mineral can only vary between endmember compositions (in molar fractions between 0 and 1) and in nature the range of composition observed is much narrower. Therefore, the self-affine fractal behaviour of OZPs is always bounded. It will be shown in the next sections that this characteristic is critical in the description of OZPs with fractal statistics.

Two methods have been used to measure the Hurst exponent of an OZP: (i) the width (Holten *et al.*, 1997) and (ii) the power spectrum (Halden & Hawthorne, 1993). The width  $w$  of a function is defined as

$$w(l) = \sqrt{[\langle y^2(x) \rangle_l - \langle y(x) \rangle_l^2]} \quad (1.3)$$

where  $\langle \cdot \cdot \cdot \rangle_l$  denotes an average over all sections with a length  $l$ . The width  $w$  scales as

$$w(l) \approx l^H \quad (1.4)$$

for self-affine fractals, i.e. a log-log plot of width versus length is linear over certain length scales with a slope of  $H$ .

The power spectrum method uses a Fourier transform of the x-y data, the so-called power spectrum. From this a spectral density,  $S_f$ , and a length

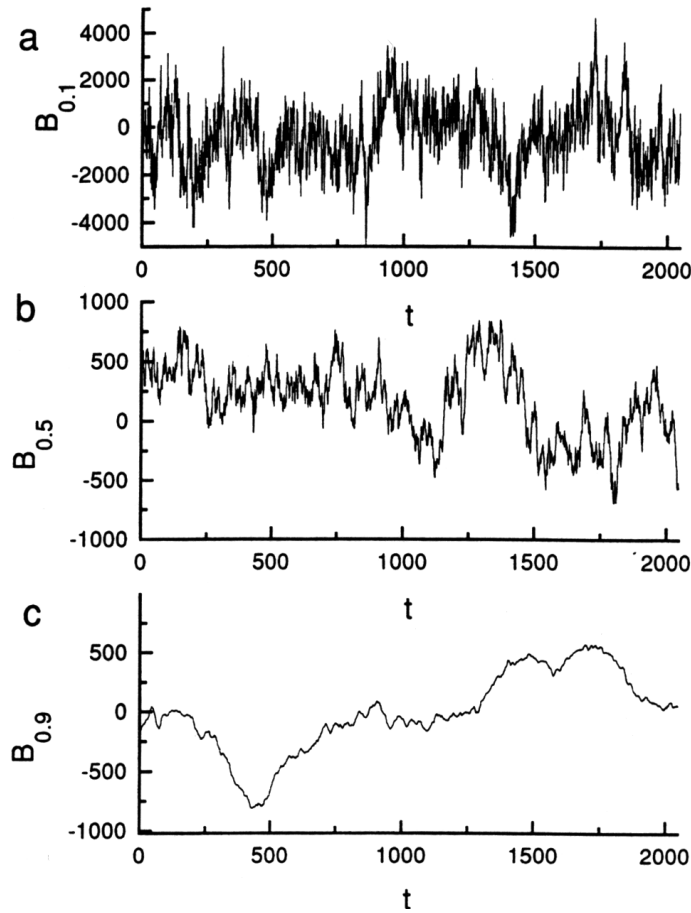


Figure 1.8: Fractional Brownian motion as an examples of self-affine fractals with varying (local) fractal dimension generated by Holten *et al.* (1997). **(a)**  $H = 0.1$  (anti-persistence) **(b)**  $H = 0.5$  (ordinary Brownian motion) **(c)**  $H = 0.9$  (persistence).

scale,  $f$ , can be obtained and scale as

$$S_f = f^{-\beta}. \quad (1.5)$$

The slope  $\beta$  of a log-log plot of  $S_f$  and  $f$  can be related to the Hurst exponent by

$$H = \frac{\beta - 1}{2}. \quad (1.6)$$

The disadvantage of this method to the width method is a higher standard deviation of  $H$ . However, some extra information about periodic components in the OZP might be gained but can also be obscured by a high noise level in the pattern.

### 1.7.2 Fractal analyses of OZPs: the problem of spatial resolution

The width  $w$  of the OZP shown in Fig. 1.1 *c* has been analysed and is plotted together with literature data in Fig. 1.10. The Hurst exponent  $H$  of 0.55 is

equal to the finding of Holten *et al.* (1997) for the same sample and method (EMP line scan). Further measurements of these authors on grandite garnets resulted in a range of  $H$  from 0.14 – 0.55. Generally, anti-persistent to slightly persistent behaviour has been found for all OZPs in different minerals which let Holten *et al.* (1997) conclude that “the input noise itself is anti-persistent”, i.e., the fractal behaviour is inherently in the crystal growth process. This statement must be questioned in the light of the findings of section 1.3 which have shown that oscillatory zoning can also occur on a scale beyond the spatial resolution of the techniques commonly applied to measure OZPs. Experimentally, the OZP cannot be measured with much higher spatial resolution because ATEM cannot provide a full zoning pattern over a distance of about 500  $\mu\text{m}$  mainly due to the limits of specimen preparation. Furthermore, measuring parts of the patterns with different magnification would unavoidably create a bias towards interesting parts of the pattern (Meakin, 1998). Therefore, the effect of small scale zoning on the fractal behaviour will be demonstrated by a simple model and the OZP of grandite garnet (Fig. 1.1 c) will be used as sample graph.

To simulate the effect of fine scale oscillatory zoning on  $H$  the spatial resolution of the pattern will be artificially increased. Each original x-value with a step width of 1  $\mu\text{m}$  will be replaced by five x-values with a step width of 200 nm. By this procedure only the x-scaling of the original pattern would change if the new points inherit the composition of the old.

The small scale zoning has been found in optically anisotropic regions with compositions of  $X_{and}^{EMP} = 0.5 - 0.9$ , but not in the optically isotropic parts ( $X_{and} > 0.9$ ). In the parts which show small scale zoning it appeared nearly bimodal with alternating compositions of  $X_{and}^{ATEM} = 1$  and  $X_{and}^{ATEM} = 0.5 - 0.7$ , respectively (cf. Fig. 1.3). Therefore, the small scale zoning will be applied to the sample pattern as follows ( $X_{gro} = 1 - X_{and}$ ):

$$\begin{aligned} &\text{for } X_{and} > 0.9 && y(x)^{old} \rightarrow y(x_{1\dots5}) \\ &\text{for } 0.9 \geq X_{and} > 0.8 && y(x)^{old} \rightarrow y(x_{1,4,5}) = 1 \quad \text{and } y(x_{2,3}) = 1 - X_{gro} \cdot \frac{5}{2} \\ &\text{for } 0.8 \geq X_{and} > 0.7 && y(x)^{old} \rightarrow y(x_{1,5}) = 1 \quad \text{and } y(x_{2,3,4}) = 1 - X_{gro} \cdot \frac{5}{3} \\ &\text{for } 0.7 \geq X_{and} && y(x)^{old} \rightarrow y(x_1) = 1 \quad \text{and } y(x_{2\dots5}) = 1 - X_{gro} \cdot \frac{5}{4} \end{aligned}$$

For the optically isotropic parts ( $X_{and} > 0.9$ ) of the pattern only the scaling but not the composition has changed. For all other parts small bimodal oscillations have been added. Thereby, the old x-value is replaced by new x-values which still preserve the mean composition of the old data point. The oscillations have been arranged in such a way that the zones with intermediate composition are in the range of  $X_{and} = 0.5 - 0.7$  and that no

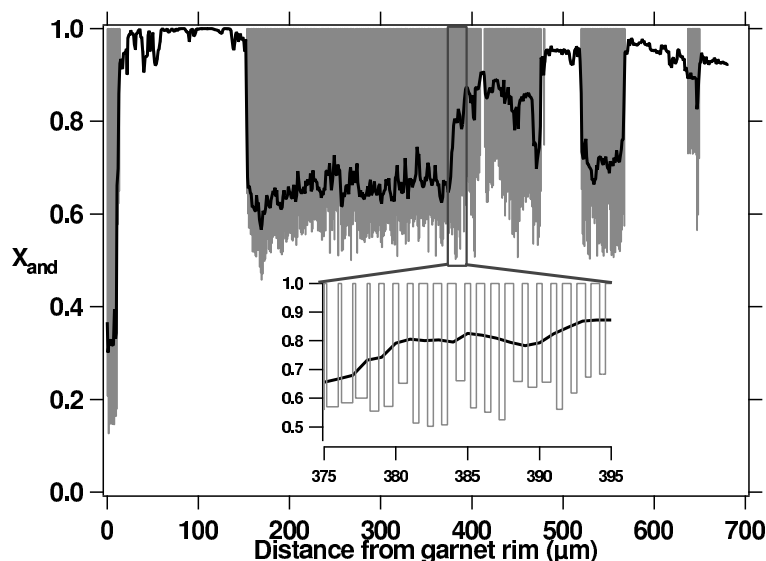


Figure 1.9: Measured (black) and simulated (grey) oscillatory zoning pattern. The simulated fine scale zoning appears as grey area because it is too fine to be displayed discernible. The enlarged part of the pattern shows the interrelation between the original/simulated composition and zone thickness.

intermediate compositions can occur next to each other without a zone of  $X_{and} = 1$  in between. To simplify matters also the thickness of the fine scale zoning have been correlated to the composition so that only one andradite and one intermediate zone occur per old data point. The result of this procedure is shown in Fig. 1.9. The small scale zoning effectively 'covers' the plane. Simply from this observation it can be judged that the  $H$  must be close to zero ( $D \simeq 2$ ) due to equation 1.2. Consequently, the width analysis of the model OZP result in  $H \simeq 0.06$  on shorter length scales (1–30  $\mu\text{m}$ ) and  $H \simeq 0.21$  on longer scales (30–300  $\mu\text{m}$ ).

A main limit of the fractal analysis of OZP becomes apparent here. The compositions of OZPs are strongly bounded, in terms of molar fraction between 0 and 1. To fulfil the premise of self-affine fractal behaviour the oscillation have to be small on small length scale and becoming bigger on larger length scales until the bounding condition is reached. At this length scale the fractal behaviour ends and  $H$  tends to 0. However, the observed fine scale zoning already fills the full compositional range at small scale. Therefore, the upper limit for fractal behaviour is already reached and  $H \approx 0$ . What is then the reason for the reported fractal behaviour in the zoning patterns?

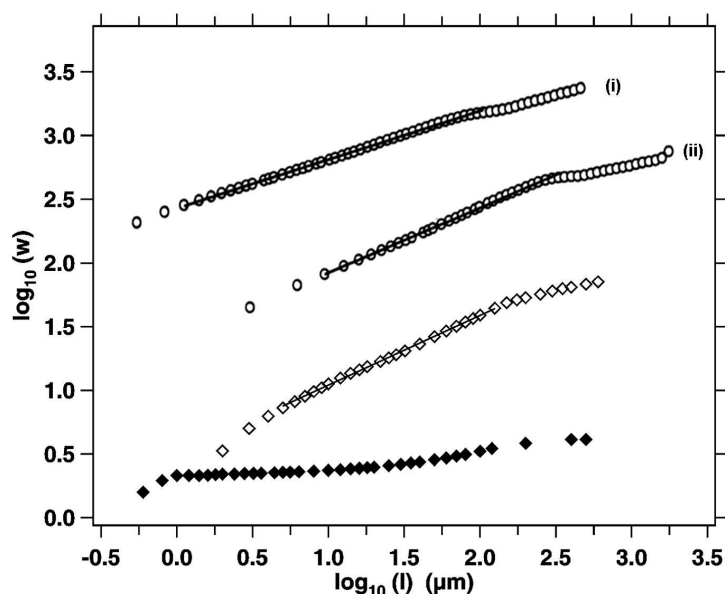


Figure 1.10: The width  $w$  of the measured (open diamonds) and simulated (black diamonds) OZP together with literature data from Holten *et al.* (1997) (open circles). Note that the y-axis is somewhat arbitrary as it depends on the quantity (e.g. greyscale, absolute/fractional composition) that was used in the width calculation. Here, the results were also shifted for illustration purposes. Of course, this does not effect the slope and, therefore, the Hurst exponent  $H$ .

The self-affine behaviour in grandite OZPs is predominantly a result of averaging a heterogeneous, compositional microstructure due to the limited spatial resolution of the applied technique. In that way the OZP is artificially smoothed on small length scales and, therefore,  $H$  increases. Actually, Holten *et al.* (1997) measured varying  $H$  on the same grandite sample using a digitised BSE image ( $H = 0.40$ , (i) in Fig. 1.10) and a EMP line scan ( $H = 0.55$ , (ii) in Fig. 1.10), respectively. The spatial resolution was about  $1 \mu\text{m}$  for the BSE image and  $3 \mu\text{m}$  for the EMP line scan. This observation suggests that  $H$  varies with spatial resolution if a microstructure in the range of or beyond the spatial resolution is present.

### 1.7.3 Criticism and perspective

In this section, it had been shown that small scale zonations strongly limit the use of self-affine fractal geometry to characterise OZPs. Especially, no clues about the underlying mechanisms (internal/external) can be deduced from the fractal behaviour for the oscillatory growth of grandite garnets. Furthermore, the usefulness of fractal analysis on OZPs must be questioned

in general. All analysed oscillatory zoned minerals so far show zoning down to a few microns with usually sharp changes in composition. Also, large jumps in composition because of interrupted growth or even resorption/dissolution are frequently observed (especially in plagioclase and garnet), but cannot be characterised by fractal analysis. In this context the attempt to correlate the Hurst exponent with changes in whole-rock chemistry as done by Hoskin (2000) for zircon must be disapproved because of the comparable scale of fine zoning and spatial resolution. The mathematical simpleness of fractal geometry favours the application to any kind of growth pattern but must be combined with the determination of important boundary values such as smallest scale of zoning and interface characteristics. Notwithstanding all drawback of fractal analysis in determining mechanisms of growth it can be used as a helpful tool to evaluate OZPs generated by growth models.



## Chapter 2

# Molecular simulations of interfacial and thermodynamic mixing properties of grossular–andradite garnets

### 2.1 Introduction

Grossular ( $\text{Ca}_3\text{Al}_2\text{Si}_3\text{O}_{12}$ )–andradite ( $\text{Ca}_3\text{Fe}_2^{3+}\text{Si}_3\text{O}_{12}$ ) solid solutions, commonly termed grandites, typically occur in metamorphic calc-silicate rocks and metasomatic skarns. They are known to exhibit optical birefringence, iridescence, and oscillatory zoning (e.g. Shore & Fowler, 1996), although the origin of these features is still uncertain and the theories about their formation are controversial. Some of the explanations are based on thermodynamic equilibrium conditions, but studies on the thermodynamic mixing properties of the solid solution are scarce. Huckenholz *et al.* (1974) observed complete solid solution up to 1128 K and decomposition into various phase assemblages above this temperature. Engi & Wersin (1987) derived an asymmetric solution model with a miscibility gap in the range of  $X_{and} = 0.02 - 0.42$  at 473 K with a critical solvus temperature of 717 K at  $X_{and} = 0.18$ . Jamtveit (1991) used a symmetric free-energy potential based on the absence compositions with  $X_{and} = 0.20 - 0.35$  and  $X_{and} = 0.65 - 0.90$  to study the dynamics of crystal growth of solid solutions. The bulk compositions of the solid solutions were within one of the two miscibility gaps. His model using miscibility gaps is one possible way to describe the formation of oscillatory zonation. In contrast, Ivanova *et al.* (1998) showed,

by reviewing the data on compositional zoning, that natural compositions found in different studies do not agree with the solution model of Engi & Wersin (1987).

The synthesis of strictly binary garnets with all Fe exclusively as  $\text{Fe}^{3+}$  in octahedral sites is difficult due to the presence of  $\text{Fe}^{2+}$  in dodecahedral sites (that are usually occupied with Ca ions) and due to the incorporation of  $\text{OH}^-$  into the structure (see, e.g., Huckenholz *et al.*, 1974; Huckenholz & Fehr, 1982; Geiger *et al.*, 1987; Geiger, 1999). In addition, it is difficult to obtain equilibrium in low-temperature syntheses and to grow homogeneous crystals that are large enough for structural and compositional analysis (Heuss-Aßpichler & Fehr, 1997). Therefore, the present study shows the value of static lattice energy calculations and subsequent Monte Carlo simulations to calculate the equilibrium mixing properties of the grandite solid solution.

A number of hypotheses have been proposed to explain the birefringence in grandites and to describe the deviation from cubic symmetry (space group  $Ia\bar{3}d$ ). These include (1) ordering of  $\text{Fe}^{3+}$  and Al on octahedral sites (Takéuchi & Haga, 1976; Takéuchi *et al.*, 1982; Akizuki *et al.*, 1984; Allen & Buseck, 1988; Kingma & Downs, 1989; Shtukenberg *et al.*, 2001b), (2) strain from lattice mismatch at compositional, twin, and grain boundaries (Chase & Lefever, 1960; Lessing & Standish, 1973; Kitamura & Komatsu, 1978), (3) substitution of rare-earth cations for Ca (Blanc & Maisonneuve, 1973), (4) noncubic distribution of  $\text{OH}^-$  groups due to the hydrogarnet substitution (Aines & Rossman, 1984; Rossman & Aines, 1986; Allen & Buseck, 1988), or (5) twinning (Ingerson & Barksdale, 1943). Hypotheses 3, 4, and 5 may be applicable for some garnets in the presence of foreign ions or for some extensively twinned grandites, but they do not provide a comprehensive explanation. Hypothesis 1 is supported by XRD refinements, but McAloon & Hofmeister (1993, 1995) found no indication for deviation from cubic symmetry due to cation ordering on octahedral sites in their studies on lattice vibrations using IR spectroscopy. Hypothesis 2 is supported by the presence of compositional interfaces at the nanometer scale in oscillatory zoned and iridescent grandites as observed by TEM (Hirai & Nakazawa, 1986, and previous section) and XRD peak analysis (Ivanova *et al.*, 1998).

The goal of this part is to derive thermodynamic properties for the grossular-andradite solid solution. Based on these thermodynamic data at equilibrium, it can be judged to what degree experimental observations such as compositional lamellae can be explained through non-equilibrium and kinetic effects. In addition to the classical thermodynamic properties

such as enthalpies, entropies, and free energies of mixing, local physical properties such as interface energies, interfacial concentration gradients, and refractive indices parallel and across interfaces were evaluated. By comparing the results with experimental data (where available), it can be estimated if physical properties such as birefringence are influenced by ordering processes or by compositional fluctuations that are often accompanied with strain effects.

## 2.2 Methods

The first step needed to calculate the enthalpy and free energy of mixing is to derive cation–cation interaction parameters for all possible pairs of exchangeable cations in the grossular–andradite solid solution (Al–Fe, Al–Al, Fe–Fe) from atomistic simulations. Using such interaction parameters in combination with a Monte Carlo method allows one to evaluate the energy of millions of configurations which is necessary for calculation of the thermodynamic properties of solid solutions (see, e.g., Myers *et al.*, 1998; Becker *et al.*, 2000; Bosenick *et al.*, 2000, and references therein). Due to the size of the garnet unit cell and the large number of configurations to be analysed, this was done using empirical force-field potentials as incorporated in the program package GULP (Gale, 1998). For these calculations, a  $1 \times 1 \times 1$  conventional unit cell with 16 exchangeable cation sites and a  $2 \times 1 \times 1$  supercell containing 32 exchangeable cations was chosen (Fig. 2.2). These allow one to evaluate the lattice energies of a sufficient number of random and ordered cation distribution at moderate computational cost. The Fe<sup>3+</sup> content of these supercells was varied such that the resulting composition ranged from 0 to 100 % andradite. One such cell with a random cation distribution (Al:Fe<sup>3+</sup> ratio = 1:1) is shown in Fig. 2.3 *a*, one with an ordered distribution in Fig. 2.3 *b*.

### 2.2.1 Derivation of force-field parameters

In general, there are two methodologies for the application and derivation of empirical potentials. One method is to apply a set of potentials that has already been shown to be applicable to a wide range of minerals. In this way, one minimizes the problem that the properties studied are already built into the model (see, e.g., Dove, 1989). In other words, if potentials fit only a limited set of available physical properties (e.g., the structure and elastic constants) of the minerals to be studied, the derived potential set may be applicable only to these properties and not to a wider range of proper-

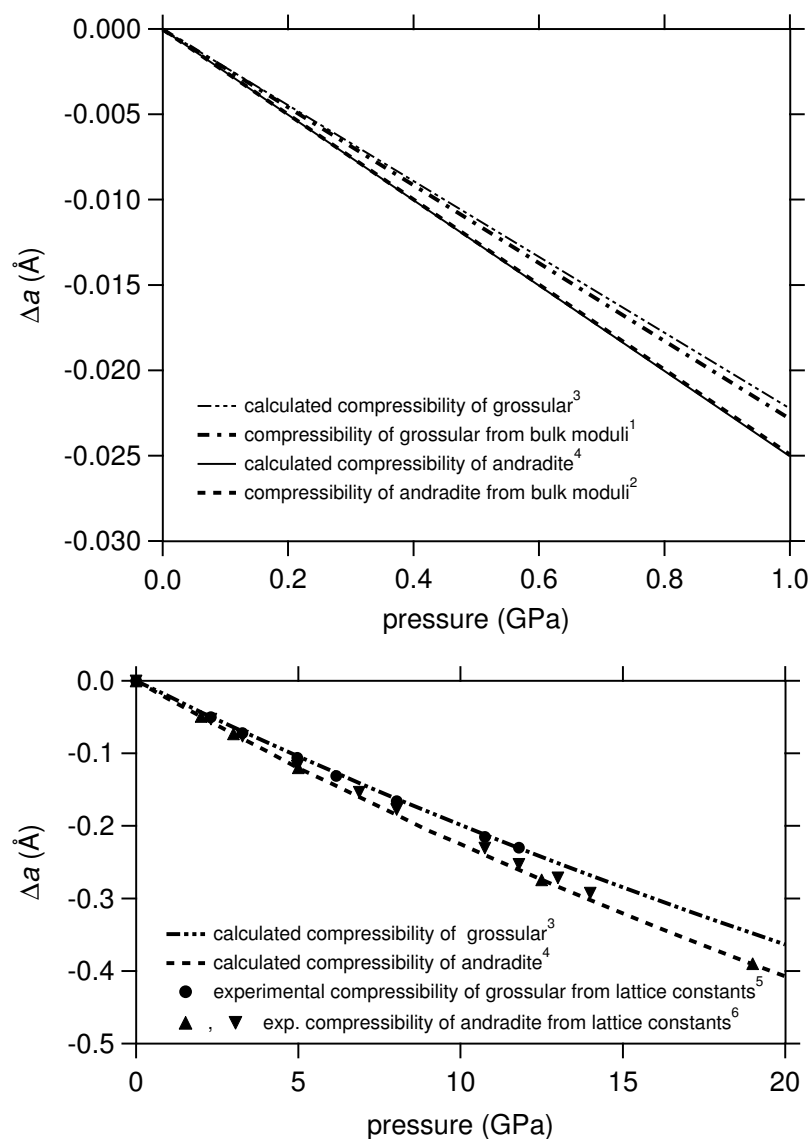


Figure 2.1: **a** Comparison of the compressibility (expressed as the change of the lattice constant as a function of pressure) as derived from the bulk moduli determined by Bass (1989, <sup>1</sup> for grossular) and by Bass (1986, <sup>2</sup> for andradite). The figure also shows the calculated compressibilities using the potential set listed in Table 2.2 (<sup>3</sup> for grossular, <sup>4</sup> for andradite). The potential set is a good representation of the difference in the elastic property measurements. **b** Compressibilities can also be evaluated from the change of the lattice parameters as a function (of a wider range) of pressure. The calculated data are obtained as described in *a*. Experimental lattice constants are from Zhang *et al.* (1999, <sup>5</sup> for grossular) and from Hazen & Finger (1989, <sup>6</sup> for andradite ▲) and from Zhang *et al.* (1999, ▼).

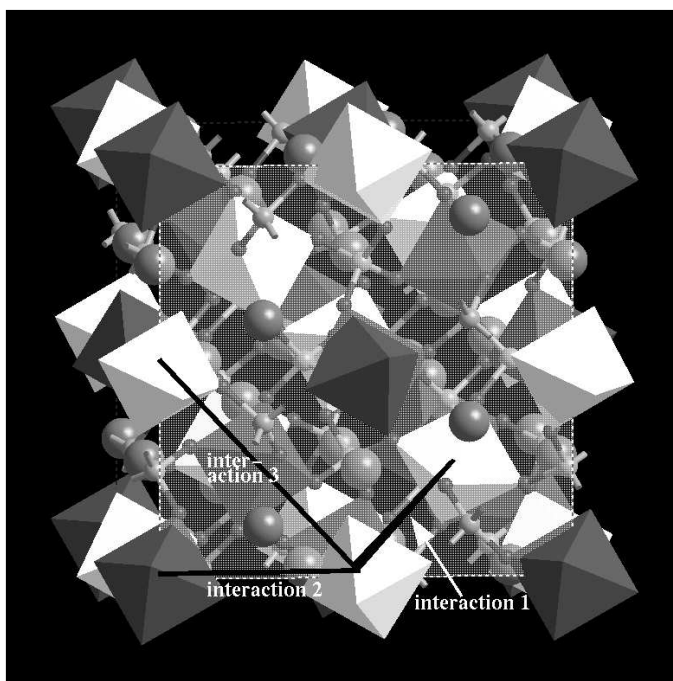


Figure 2.2: Atomic model of one of the conventional unit cells (in this case,  $\text{Fe}^{3+} : \text{Al} = 1 : 1$ ) that were used to calculate the lattice energy of a grossular–andradite mixture. Al octahedra are *dark* and Fe octahedra are *light grey*. The cell has shown an ordered configuration with alternating Al and Fe octahedra in the main crystallographic directions  $[100]$ ,  $[010]$ , and  $[001]$ . The *labels of the interactions* indicated refer to those in Table 2.3. This configuration was found to be the most energetically favourable for a 1:1 composition of  $\text{Fe}^{3+}$  and Al.

ties such as thermodynamic properties. However, the differences in the structure and in the physical properties such as elastic constants between grossular and andradite are very small. For example, the difference between the unit-cell dimension of grossular and andradite is  $0.21 \text{ \AA}$ , whereas the variation in the lattice constant of grossular by using the potential sets of Bush *et al.* (1994), Catlow (1988), and Sanders *et al.* (1984) is  $0.26 \text{ \AA}$ . Therefore, the goal in deriving force-field parameters for the solid solution in this study was to develop a potential set that models the subtle differences in the structure and other physical constants as precisely as possible. In addition, these potentials have to be as similar as possible to sets that have proven to model successfully a whole class of similar minerals. Therefore, the potentials listed in Bush *et al.* (1994), Catlow (1988), and Sanders *et al.* (1984, for a careful review of these potentials, see, e.g., Bosenick *et al.*, 2000) were used as starting parameters. Only for the  $\text{Fe}^{3+}\text{--O}$  interaction a new

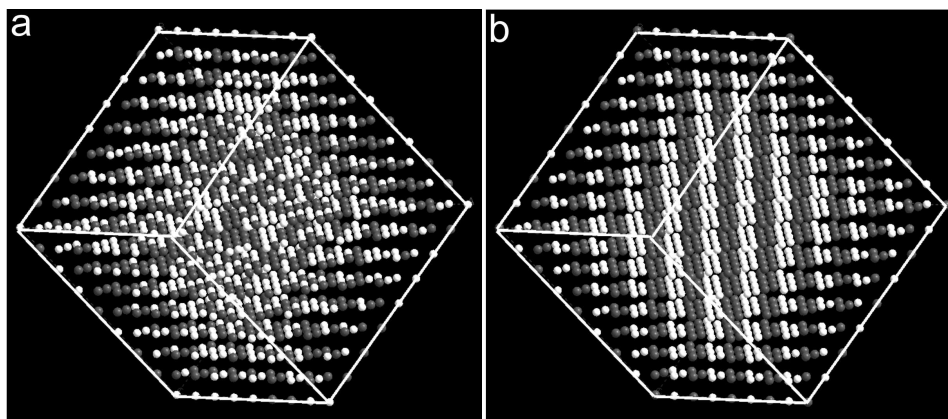


Figure 2.3: **a** Atomic model of one of the  $4 \times 4 \times 4$  supercells (in this case, Al : Fe<sup>3+</sup> ratio = 1 : 1, lattice vectors  $\parallel [100], [010], [001]$ ) that was used in the Monte Carlo simulations to calculate the enthalpy of a grossular–andradite using a disordered configuration. For clarity, only the exchangeable cations in the structure are shown. **b** Model of the supercell with an ordered configuration that was most energetically favorable. This structure is the same as in Fig. 2.2 [structural physical properties in Table 2.4, but this projection depicts more clearly the orientation of consecutive Al and Fe<sup>3+</sup> double layers  $\parallel (111)$ ].

repulsive potential had to be derived. The potential parameters of the Al–O pair potential were used as starting values for the new Fe<sup>3+</sup>–O pair potential, and the fit was performed in such a way that the structure as well as the elastic and dielectric constants of andradite were obtained as closely as possible. The fitting of the potential parameters to the structure and physical properties of grossular and andradite was also performed using the program package GULP.

The potentials that were used for the calculation of cation–cation interaction parameters are listed in Table 2.1 and the resulting calculated structure and physical properties are compared with experimental results in Table 2.2. Bosenick *et al.* (2000) describe that the O–O distances in the shared and unshared edge of the Al or Fe<sup>3+</sup> octahedra can be used as a critical parameter for the quality of a potential. Since we are mainly interested in the difference of the structural parameters between grossular and andradite, we can compare these atomic separations and obtain for  $(\text{O}-\text{O}_{\text{and}}-\text{O}-\text{O}_{\text{gros}})_{\text{shared}} = 0.143 \text{ \AA}$  from the experimental values by Armbruster & Geiger (1993) and Geiger & Armbruster (1997) and  $(\text{O}-\text{O}_{\text{and}}-\text{O}-\text{O}_{\text{gros}})_{\text{shared}} = 0.145 \text{ \AA}$  for the respective optimized structures using our po-

tential set in Table 2.1. The differences of the length of the unshared edge are 0.123 Å (experimental) and 0.120 Å (computational). However, due to the compromise by also fitting the elastic and dielectric constants, the calculated absolute values for these O–O separations can be off by up to 0.1 Å. The deviation from the experimental elastic and dielectric constants are also within the experimental errors as well as the compressibility as a function of pressure (Fig. 2.1). Thus, there are a number of physical properties for which this potential set is an improvement when applied to the grossular–andradite solid solution. However, in terms of the fractional coordinates of the O atom, the used potentials seem to be slightly worse (up to 0.008 fractional units as compared to 0.004 fractional units for the potentials described by Bosenick *et al.* (2000), but the deviation from experiment is acceptable because the difference is in the same direction for grossular and andradite. Therefore, the differences between the two phases are well represented by the potentials in Table 2.1. Finally, the calculated vibrational entropies have been compared with calorimetric measurements (Kolesnik *et al.*, 1979; Westrum *et al.*, 1979; Haselton & Westrum, 1980; Madon & Ibaruchi, 1991). Even though the absolute values are slightly too high by  $\approx 5\%$ , the differences in the vibrational entropies of grossular and andradite is well reproduced.

### 2.2.2 Calculation of cation–cation interaction parameters

For the described range of compositions, 504 random configurations with 16 different  $\text{Fe}^{3+} : \text{Al}$  ratios between 0 and 1 were generated and their relaxed lattice energies calculated using GULP. In addition, we generated five special cases, e.g., with  $\text{Fe}^{3+}$  and Al layers parallel to (100), (111), and the ordering scheme suggested by Takéuchi *et al.* (1982). For all 509 configuration considered, a full geometric optimization with no symmetry restrictions was performed (the lattice constants  $a$ ,  $b$ , and  $c$ , the angles  $\alpha$ ,  $\beta$ , and  $\gamma$ , and all internal coordinates were allowed to vary). Due to the usage of a core-shell model for O atoms, a conventional garnet unit cell contains 160 atoms, 256 core-shell positions, and 771 independent variables.

The next task is to derive cation–cation interaction parameters. The idea behind these interaction parameters is that the energy (Coulomb energy, repulsive and van der Waals contribution, and strain effects in a lattice with a specific cation configuration) of a particular solid solution is expressed by the arrangement of cations. This means that all energy contributions from a full geometry optimization are reflected by the cation distribution. The advantage of this procedure is that the calculation of the energy of one partic-

Table 2.1: Potential parameters for the interactions within grossular and andradite as used for the GULP calculations.

Interaction	Type	Interatomic potentials						Ref. <sup>c</sup>
		This study			Previous studies			
		A	B	C	A	B	C	
O–O	Buck. <sup>a</sup>	22739.2	0.1266	32.756	22764.0	0.1490	27.880	(1)
Ca–O	Buck.	1459.4	0.3003	0	2272.7	0.3000	0	(3)
Al–O	Buck	1333.9	0.3124	0	1460.3	0.2991	0	(2)
Fe <sup>3+</sup> –O	Buck	1213.3	0.3318	0	-	-	-	-
Si–O	Buck.	1548.5	0.3191	9.6262	1283.9	0.3205	10.662	(1)
O–Si–O	Three-body <sup>b</sup>	1.54762	109.47	-	2.09724	109.47	-	(1)
O–Al–O	Three-body	2.32051	90.000	-	2.09724	90.00	-	(1)
O–Fe–O	Three-body	1.39060	90.000	-	-	-	-	-

Charges used for Coulomb potentials

Atom type	Charge
Ca	+2.00
Fe, Al	+3.00
Si	+4.00
O <sub>core</sub>	+0.8482
O <sub>shell</sub>	-2.8482

<sup>a</sup> Buckingham  $A \cdot \exp(-r/B) - C/r^6$  ( $A$  in eV,  $B$  in Å,  $C$  in eV · Å<sup>6</sup>)<sup>b</sup> Three-body  $\frac{1}{2}A(\theta - B)^2$  ( $A$  in eV/rad<sup>2</sup>,  $B$  in degrees)<sup>c</sup> References for previously derived potentials: (1) Sanders *et al.* (1984), (2) Catlow (1988), (3) Bush *et al.* (1994)

ular configuration requires in the order of ms of computer time rather than minutes, as in the case of a full geometry optimization. Interaction parameters are obtained by fitting the energy expression using these parameters to the lattice energies obtained from the 509 GULP optimization calculations according to equation 2.1. Different cation–cation interaction types can be considered during such a fitting procedure. Cation–cation interaction types can be defined by the structural relationship of the cations in the lattice, that is the distance  $\Delta x$ ,  $\Delta y$ , and  $\Delta z$  between them. Symmetry-equivalent structural relationships are described by the same interaction type. Due to the cubic symmetry of garnets, different interaction types need only be distinguished by the distance between the exchangeable atoms. In this study, we chose to include first, second, and third nearest-neighbour interactions, as indicated in Table 2.3. These three interaction types resulted in a sufficient agreement between the excess lattice energies for the fully optimized GULP calculations and the energies using cation–cation interaction para-



meters (regression coefficient of 0.998 between the total GULP versus fitted energies and 0.914 by comparing excess energies).

As described in more detail, e.g., in Becker *et al.* (2000), the fitting procedure can be performed with different combinations of interaction types by applying equation 2.1:

$$E_{GULP} \leftarrow E_{fit} = \sum_i (n_{Al-Fe}^i \cdot E_{Al-Fe}^i + n_{Al-Al}^i \cdot E_{Al-Al}^i + n_{Fe-Fe}^i \cdot E_{Fe-Fe}^i), \quad (2.1)$$

where  $n_{Me-Me}^i$  is the number of cation interaction of that type in a given configuration that was energy-optimised in a particular GULP calculation.  $E_{Me-Me}^i$  is the energy associated with forming an Me–Me pair for a given interaction type  $i$ . Note that there are different ways in the literature to formulate equation 2.1 which may vary by a prefactor of 2 (and may, thus, lead to interaction energy parameters that may differ by a factor of 2) or by the sign of the parameters (see, e.g., Myers, 1998; Myers *et al.*, 1998; Bosenick *et al.*, 2000, and references therein).

Since we are interested in the excess thermodynamic properties of mixing, we need to define only one interaction parameter per interaction type  $i$ :

$$E_{interaction}^i = E_{Al-Fe}^i - \frac{1}{2}(E_{Al-Al}^i + E_{Fe-Fe}^i) \quad . \quad (2.2)$$

Then, the excess energy of mixing can be written as:

$$E_{excess} = \sum_i n_{Al-Fe}^i \cdot E_{interaction}^i \quad . \quad (2.3)$$

### 2.2.3 Determination of thermodynamic properties

The results for the interaction parameters are listed in Table 2.3, indicating that ordering in the solid solution promotes homocationic next and third nearest-neighbour (positive interaction parameters) and heterocationic second nearest-neighbour interactions (negative interaction parameters).

In order to calculate the enthalpy of mixing, Monte Carlo simulations were performed using a code developed at the University of Münster by Udo Becker (Becker *et al.*, 2000, for a general description of the method, see, e.g., Myers *et al.* (1998)). For the Monte Carlo simulations, two different unit cells were used. One cell consisted of a  $4 \times 4 \times 4$  conventional unit cell with the edges parallel to the  $[100]$ ,  $[010]$ , and  $[001]$  crystallographic directions (1024 exchangeable cations), whereas the other had edges parallel to  $[111]$ ,  $[0\bar{1}1]$ , and  $[\bar{2}11]$ , with 1440 exchangeable cations. The two

Table 2.2: Comparison of experimental structural parameters (in Å for lattice constants,  $a$ , fractional units for the O position,  $x_O$ ,  $y_O$ ,  $z_O$ ), elastic constants ( $c_{xy}$  in GPa), static dielectric constants ( $\epsilon_{stat}$ ) and third-law vibrational entropies ( $s^0$  in J/(mol · K)) with calculated ones using the interatomic potentials in Table 2.1.

<sup>a</sup> The experimental values for 0 K were converted from the room-temperature lattice constants (11.847 Å for grossular, Armbruster & Geiger 1993, and 12.063 Å for andradite, Geiger & Armbruster 1997) by using the thermal expansion coefficients in Gillet *et al.* (1992) and Isaak *et al.* (1992).

<sup>b</sup> Position of symmetry unique O atom; all other atoms are at special positions.

<sup>c</sup> Elastic constants for grossular from Bass (1989)/Conrad *et al.* (1999), for andradite from Bass (1986)/Conrad *et al.* (1999).

<sup>d</sup> Static dielectric constants from Shannon & Rossman (1992).

<sup>e</sup> Haselton & Westrum (1980), see also Geiger (1999)

<sup>f</sup> Westrum *et al.* (1979)

<sup>g</sup> Kolesnik *et al.* (1979)

<sup>h</sup> Robie *et al.* (1987)

<sup>i</sup> Madon & Ibaruchi (1991)

	Experimental Grossular	Calculated Grossular	Experimental Andradite	Calculated Andradite
$a$ <sup>a</sup>	11.821	11.823	12.034	12.029
$x_O$ <sup>b</sup>	0.038100	0.030458	0.03986	0.03156
$y_O$ <sup>b</sup>	0.045126	0.052334	0.04885	0.05486
$z_O$ <sup>b</sup>	0.651409	0.651280	0.65555	0.65514
$c_{11}$ <sup>c</sup>	333.41/321.17	333.26	297.71/289	294.74
$c_{12}$ <sup>c</sup>	92.54/91.4	99.61	93.1/92	91.49
$c_{44}$ <sup>c</sup>	107.74/104.6	106.74	85/85	80.61
$\epsilon_{stat}$ <sup>d</sup>	87.10	84.02	105.90	99.62
$s^0$	260.1 <sup>e</sup> /254.7 <sup>f</sup> /256.5 <sup>g</sup>	280.5	316.4 <sup>h</sup> /313.6 <sup>i</sup>	330.8

different supercells were chosen to study the interface energies and concentration gradients at specific crystallographic interfaces. The results for bulk thermodynamic properties of mixing for the two supercells were very similar. The number of swaps in the Monte Carlo calculation were 2 million “accepted” swaps or 10 million overall swaps per composition and temperature. We calculated the configurational free energy and entropy of mixing using the Bogoliubov integration scheme (Yeomans, 1992; Myers, 1998).

The long-range order parameter  $q$  was calculated with respect to the most energetically favourable configuration for a 1:1 composition of Al and Fe<sup>3+</sup> as shown in Fig. 2.2 that is described in the *Results* section. With respect to such an ordered configuration,  $q$  can be defined for any grossu-

lar/andradite composition as:

$$q = \frac{(\sum \text{Fe on Fe sites} - (\sum \text{Fe on Al sites}))}{\sum (\text{Fe on both site types})} . \quad (2.4)$$

There is one difficulty in determining the order parameter because there are two equivalent structures with  $q = 1$ . Therefore, we calculate  $q$  with respect to both structures and defined the order parameter to be the maximum of the absolute values of both  $q$  values.

### 2.2.4 Calculation of the vibrational entropy and the zero-point energy

In order to test if there is a significant contribution of the vibrational entropy to the entropy of mixing (which mainly consists of the configurational entropy), the vibrational entropy was calculated in the harmonic approximation as installed in GULP. For all previously described 509 configurations, zero-point energies (which also contribute to the free energies of mixing) were computed for the energy-optimised relaxed structures and the vibrational entropies at temperatures between 0 and 1000 K in steps of 100 K. In order to understand the role of zero-point energies as a function of composition and temperature in a solid solution, one has to keep in mind that different configurations are likely to occur at different temperatures. For example, at low temperature, the zero-point energies is mainly determined by relatively few ordered configurations, and at high temperatures

Table 2.3: Cation–cation interactions that were considered to describe the energetics of cation ordering and the enthalpy of mixing in the grossular–andradite solid solution. All interactions are defined by their cation–cation distance. The distances listed are derived from the grossular structure. The *third column* lists the number of interactions that occur in a  $1 \times 1 \times 1$  supercell (interactions within the supercell count fully, those reaching outside the cell by one half). The *fourth column* contains the interaction parameters according to equations 2.2 and 2.3 for compositional interactions and the *last column* the respective parameters for the excess vibrational zero-point energy (both in meV/interaction).

Interaction parameter label $i$ and type	Cation–cation distance	No of interactions in convent. unit cell/No of neighbours per cation	Interaction parameter	Interaction parameter for zero-point energy
1 (nearest-neighbour)	5.13 Å	64/8	9.4	-0.15
2 (second nearest)	5.92 Å	48/6	-11.2	0.35
3 (third nearest)	8.37 Å	96/12	2.5	-0.09

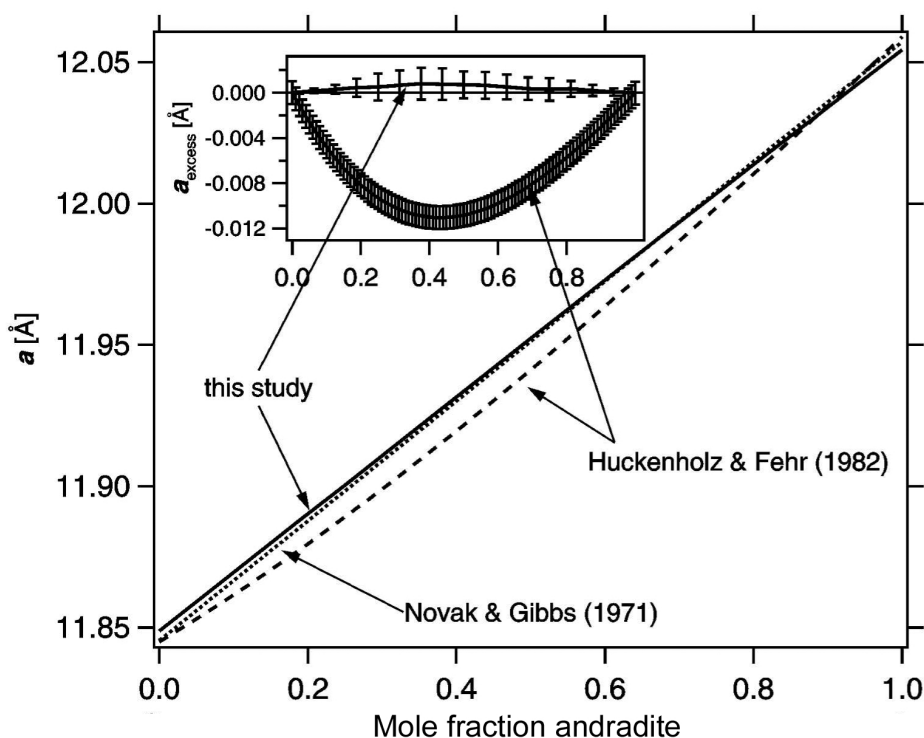


Figure 2.4: Experimental (Huckenholz & Fehr, 1982) and calculated (*points with error bars in the insert*) cell parameters,  $a$ , as a function of the composition of the grossular–andradite solid solution. The *insert* shows the excess cell parameters. The *error bars* of the calculated cell parameters are derived from the variance of these parameters from the GULP calculations with different configurations for each respective composition. The calculated cell parameters  $a$  can be, within the errors, represented by a *straight line* as a function of composition. The theoretical/experimental values by Novak & Gibbs (1971) and the experimental values by Huckenholz & Fehr (1982) are discussed in the text.

by the average of the zero-point energies of many disordered configurations. After calculating the zero-point energies for all 509 configurations that were used for the GULP optimisation runs, it is possible to derive ‘zero-point energy interaction parameters’ (Table 2.3) analogously to the interaction parameters that are used for the calculation of the enthalpies in the Monte Carlo calculations.

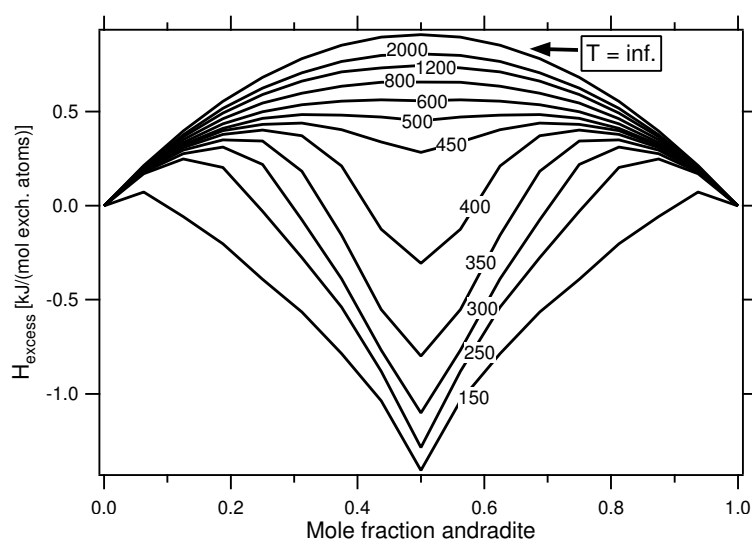


Figure 2.5: Excess enthalpies of mixing for different (annealing) temperatures (temperature labels are in K). Below  $\approx 500$  K and for a 1 : 1 composition of Al and  $\text{Fe}^{3+}$ , the system shows a tendency to order towards ordered grandite (see Figs. 2.2 and 2.3 b and Table 2.4). Below 400 K, the enthalpy of mixing for ordered grandite is  $\approx 1.5$  kJ/(mol exchangeable cations) lower than for an (interface-free) mixture of the two end members grossular and andradite.

## 2.3 Results

### 2.3.1 Comparison of experimental and calculated cell parameters

In order to obtain a first estimate on how ideal the grossular–andradite solid solution is in terms of its volume of mixing, Fig. 2.4 shows the lattice constant of the solid solution as a function of composition. Calculated lattice constants were obtained by averaging the lattice constants from the GULP optimisation for each composition, respectively. Due to the cubic symmetry of garnets, only one lattice parameter is considered in Fig. 2.4. The calculated results are closer to ideality than the experimental results of Huckenholz & Fehr (1982), who measured a negative deviation from ideality of up to  $0.01 \text{ \AA}$  for intermediate compositions. So far, it is not possible to judge if the small difference between experiment and theory is due to non-equilibrated samples or samples with admixtures of small amounts of other atoms (especially for intermediate compositions) or to interatomic potentials that do not perfectly describe the structure of intermediate grandites.

### 2.3.2 Enthalpies of mixing

Figure 2.5 shows the enthalpy of mixing as a function of temperature and composition. The most notable feature of this graph is that below 500 K and at intermediate compositions, the enthalpy shows a significant ‘dip’ towards more energetically stable configurations than disordered grandite with randomly distributed Al and  $\text{Fe}^{3+}$ . At room temperature, the average enthalpy of these structures with partly ordered cation distributions is in the order of 1.2 kJ/(mol exchangeable cations) more energetically favourable than the average of the two end members and  $\simeq 2.1$  kJ/(mol exchangeable cations) more energetically downhill than grandite with a random distribution of Al and  $\text{Fe}^{3+}$  ions. At 0 K, the enthalpy difference between the perfectly ordered grandite and the average of the two end members is on the order of 1.6 kJ/(mol exchangeable cations).

The first question to answer is: what is the distribution of Al and  $\text{Fe}^{3+}$  atoms at a 1 : 1 ratio of the two cations in this energetically stable ordered configuration? The configuration is shown in Figs. 2.2 and 2.3 *b*. This structure is referred to as ‘ordered grandite’ with the calculated structure parameters and physical properties listed in Table 2.4. The configuration of Al and Fe octahedra shown in Fig. 2.2 is a direct consequence of the interaction parameters listed in Table 2.3. The largest absolute value of interactions is parameter 2 which promotes that Al and Fe octahedra alternate along the main crystallographic axes ([100], [010], and [001]) at a distance of half a unit cell. Simultaneously, this results in the most favourable configuration for interaction parameter 3 because, e.g., at the positions  $(1/2, 0, 0)$  and  $(0, 1/2, 0)$  there would be either Al or Fe octahedra only. According to this scheme, each of the two sublattices for octahedrally coordinated cations by itself [one with its origin at  $(0, 0, 0)$ , the other at  $(1/4, 1/4, 1/4)$ ] could be perfectly ordered with respect to interaction parameters 2 and 3. However, once the two sublattices are combined, ordering is less favourable in terms of interaction parameter 1, because there are as many homocationic as heterocationic interactions with distances of  $(\pm 1/4a, \pm 1/4a, \pm 1/4a)$  and its positive value favours homocationic interactions. Nevertheless, this is overall the most energetically favourable ordering scheme which leads to an ordered structure with consecutive double layers of Al and  $\text{Fe}^{3+}$  cations parallel to (111) planes (see Fig. 2.3 *b*, only those cations are shown in the figure that form octahedra with oxygen atoms).

### 2.3.3 Free energies and entropies of mixing

The free energies of mixing are shown in Fig. 2.6 with a focus on lower temperatures in Fig. 2.6a. From these free energies of mixing a phase diagram can be derived that is shown in Fig. 2.7. Only for temperatures lower than about 430 K there are miscibility gaps between grossular and ordered grandite and between ordered grandite and andradite. For example, grossular, (theoretically) equilibrated at room-temperature, can contain up to about 20% of grandite. For temperatures higher than about 400 K, a complete solid solution is calculated. The consequence is that even though there is a significant minimum in the enthalpy and the free energy for a 50:50 composition due to ordering, it will be difficult to find a sample that was equilibrated at temperatures low enough to form large crystals of ordered grandite. However, it may be possible to form small domains with a structure listed in Table 2.4.

A similar trend due to ordering can be observed in the configurational entropy of mixing (Fig. 2.8). For temperatures above 500 K, the entropy lies within 10% of the point entropy (the configurational entropy for  $T \rightarrow \infty$ ). Only for equilibration temperatures below 450 K is the entropy significantly decreased for intermediate compositions (30:70  $\rightarrow$  70:30) due to ordering towards ordered grandite.

Finally, the same ordering tendency is reflected by the long-range order parameter as a function of temperature and composition (Fig. 2.9). The order parameter stays below 0.1 for  $T \leq 500$  K and increases close to 1 only

Atom	Xfrac	Yfrac	Zfrac
Ca	0.995378	0.245378	0.125000
Ca	0.498715	0.748715	0.125000
Al	0.999517	0.999517	0.999517
Fe	0.500382	0.500382	0.500382
Si	0.997755	0.254853	0.375076
O	0.028325	0.050181	0.658262
O	0.972018	0.949818	0.340464
O	0.533701	0.556534	0.148162
O	0.465717	0.443769	0.853274
Elastic constant			
$C_{11}$	309.1 GPa		
$C_{12}$	91.0 GPa		
$C_{44}$	91.2 GPa		
Static dielectric constant	9.0		

Table 2.4: Atomic positions and physical properties of ordered grandite for  $T = 0$  K as calculated using the interatomic potentials in Table 2.1. Space group  $P4_132$ ; Lattice constant: 11.932 Å (0 K), 11.957 Å (300 K).

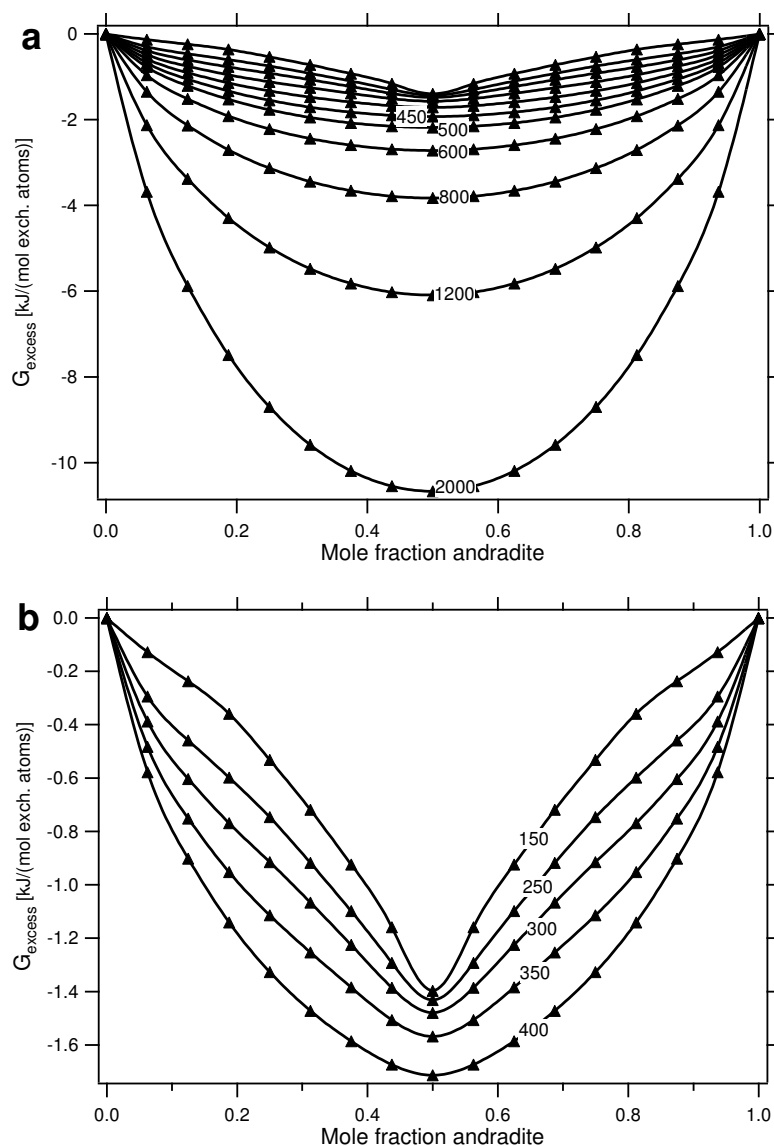


Figure 2.6: **a** Free configurational energies of mixing for different (annealing) temperatures (in K) and compositions. **b** Zoomed version for temperatures  $< 400$  K.

for compositions between 35 : 65 and 65 : 35 and for equilibration temperatures close to or below room temperature.

Figures 2.10 and 2.11 show the excess vibrational entropies of mixing,  $S_{\text{vib}}^{\text{exc}}$ , and the vibrational zero-point energies,  $E_{\text{zp,vib}}$ , (absolute and excess values), respectively. It is interesting to note that  $S_{\text{vib}}^{\text{exc}}$  has its maximum values for temperatures at about 400 K, above and below which these excess entropies decrease to 0 for  $T \rightarrow 0$  K and  $T \rightarrow \infty$ . The vibrational entropies



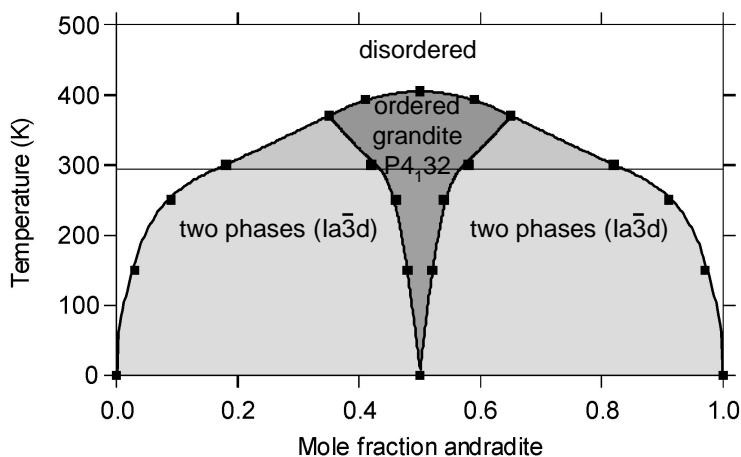


Figure 2.7: Phase diagram for the grossular–andradite solid solution at low temperatures. The calculation includes corrections for vibrational entropies (Fig. 2.10) and zero-point entropies (Fig. 2.11, see also Fig. 2.12). The transition from disordered to ordered grandite can be derived from  $q(T)$  diagrams as in Fig. 2.9 *b*. Such transitions to ordered states with a local  $B_{32}$  symmetry are typical for cubic systems with interaction parameters that have opposite signs for nearest and second nearest-neighbour interactions (Inden & Pitsch, 1991).

of mixing are slightly asymmetric about  $X_{and} = 0.5$  which has partly to do with the different masses of Al and Fe. Even though the absolute values of the zero-point entropies (Fig. 2.11 *a*) appear to be almost linear, there are small excess contributions to the free energies of mixing which are positive for  $T \leq 900$  K and negative for  $T \geq 900$  K (Fig. 2.11 *b*). The contributions of both  $S_{vib}^{exc}$  and  $E_{zp,vib}$  to the overall free energies are relatively small, as shown for the free energies of mixing at 300 and 400 K in Fig. 2.12. At these temperatures, both contributions  $-T \cdot S_{vib}^{exc}$  and  $E_{zp,vib}$  are positive and, therefore, lower the absolute values of the free energies of mixing by up to 10%. However, this effect has only a small influence on the phase diagram, such as the positions of the miscibility gaps.

With the correction of the excess vibrational entropy and zero-point energy of mixing, a phase diagram of the grossular–andradite solid solution has been derived (Fig. 2.7), which shows again the miscibility gaps at temperatures that are lower than most natural crystallisation temperatures.

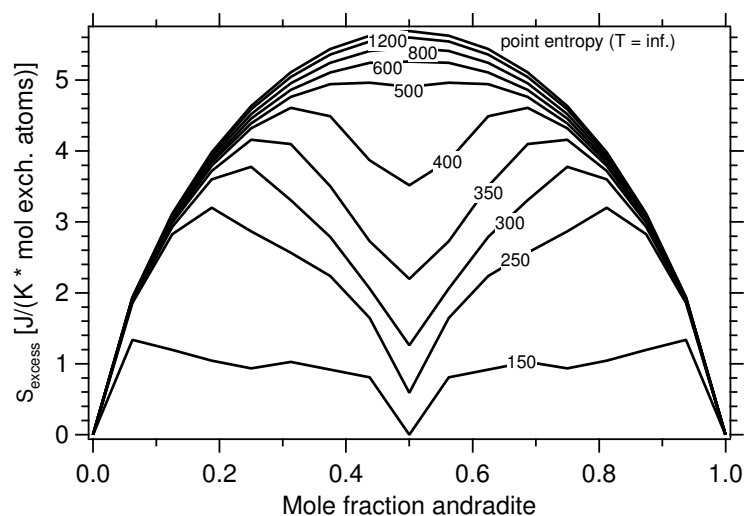


Figure 2.8: Calculated configurational entropies of mixing as derived from the difference of the free energy of mixing using the Bogoliubov integration scheme and the enthalpy of mixing from Monte Carlo runs. For temperatures above 500–600 K (*temperature labels* are in K), the configurational entropy is close to the point entropy at infinite temperature. For temperatures below 500 K and compositions close to 50% andradite the configurational entropy decreases significantly due to ordering.

### 2.3.4 Processes at interfaces

No interfaces can exist between the two end members at equilibrium conditions, as can be deduced from Fig. 2.6 for solid solution that consists of only andradite and grossular. According to the calculations, there can be stable interfaces only between grossular and grandite and between grandite and andradite. Therefore, there would be not much driving force to change compositional oscillations, as described in the previous chapter, where the  $\text{Fe}^{3+}/(\text{Al} + \text{Fe}^{3+})$  ratio does not oscillate between 0 and 1, but rather between an intermediate value and close to unity. How pure the end members on one side of the interface are and how well ordered and of what composition grandite on the other side of the interface is depends on the temperature of equilibration.

In order to evaluate how the cation distribution across an interface could look, Monte Carlo simulations were performed in a supercell with edges parallel to  $[111]$ ,  $[0\bar{1}1]$ , and  $[\bar{2}11]$  that contained 1440 exchangeable cations (see *Methods* section). Figure 2.13 *a* and *b* shows such a unit cell with a configuration of a Monte Carlo simulation at room temperature and an  $\text{Fe}^{3+}/(\text{Al} + \text{Fe}^{3+})$  ratio of 0.75. Note that due to the periodic boundary conditions, there always has to be an even number of interfaces per unit

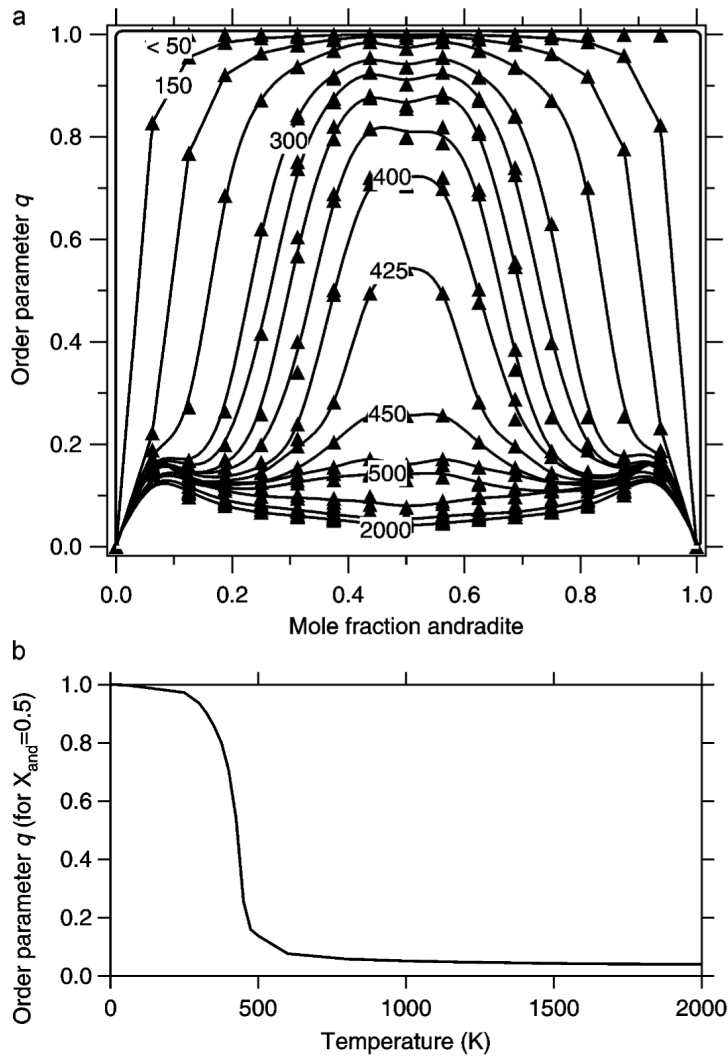


Figure 2.9: **a** Long-range order parameter  $q$  (see equation 2.4) as a function of temperature (in K) and composition. **b** Long-range order parameter  $q$  (for  $x_{\text{and}} = 0.5$ ) as a function of temperature. The tailing out of  $q$  above the transition temperature for ordering  $T_c$  (rather than a faster approach to zero) is due to the limited size of the simulation cell. Only for simulation cells of several thousands of Al/Fe<sup>3+</sup> cations the tailing can be avoided. This would cause a large increase in computer time but negligible changes in the rest of the thermodynamic mixing properties or in  $q$  for  $T \lesssim T_c$ .

cell. For instance, in Fig. 2.13, there are two interfaces parallel to the (111) plane, one in the center of the image (grossular on the left and grandite on the right) and one interface that is centered close to the left/right face of the unit cell. Even if equilibrated at a temperature as low as 300 K (Fig. 2.13 a), the concentration gradient at the interface is not atomically sharp because

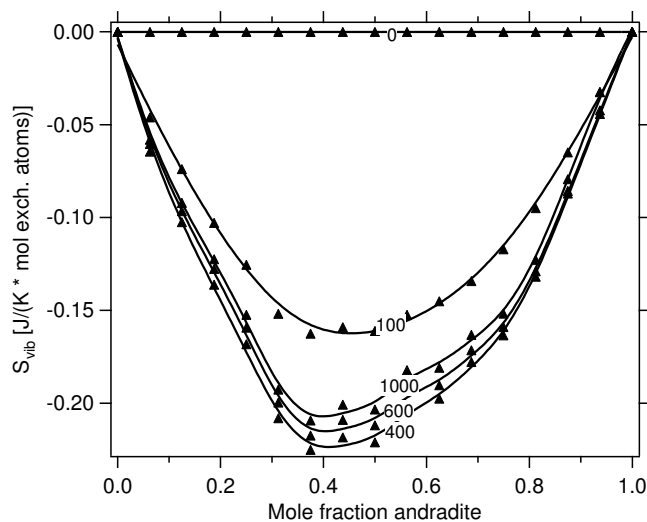


Figure 2.10: Calculated excess vibrational entropies of mixing as derived from a pseudo-harmonic approximation using GULP. The absolute values of the excess entropies have maximum values for temperatures of  $\simeq 400$  K (all *temperature labels* in K).

there are still some  $\text{Fe}^{3+}$  ions in the grossular plane. In order to quantify this, Fig. 2.13 *c* shows the concentration profile for the cells shown in Fig. 2.13 *a* and *b* (300 K and 150 K). For 300 K, there is a gradual concentration gradient that is stretched out over about 20 Å across the interface. Only at  $T \leq 300$  K would one get sharp concentration gradients (Fig. 2.13 *b*).

Another way to look at different interfaces is to evaluate the interface energies for different crystallographic directions (Table 2.5). The interface energy is defined as the energy by which an interface is energetically less favourable than the average of the phases on either side of the interface. Table 2.5 confirms that interfaces between grossular and andradite are not thermodynamically stable. Another finding is that, if no other influences play a role in the formation of interfaces, we would expect to find most interfaces parallel to (100) followed by (110) and (111). The reason for why we find interfaces  $\parallel$  (111) in Fig. 2.13 rather than  $\parallel$  (110) [there is no face  $\parallel$  (100) in the setup in Fig. 2.13] is that the interfacial area  $\parallel$  (111) ( $= 2430 \text{ \AA}^2$ ) is significantly smaller than the area  $\parallel$  (110) ( $= 3572 \text{ \AA}^2$ ) such that the interfacial energy per unit cell is more energetically favourable in the (111) case. The absolute values of the interface energies in Table 2.5 are lower than typical values for incoherent interfaces, showing the epitaxial compatibility between grossular and andradite. The calculated interface energies are comparable to those of ferroelectric domain wall energies in, e.g.,  $\text{LaTiO}_3$  (Yang *et al.*, 2000).

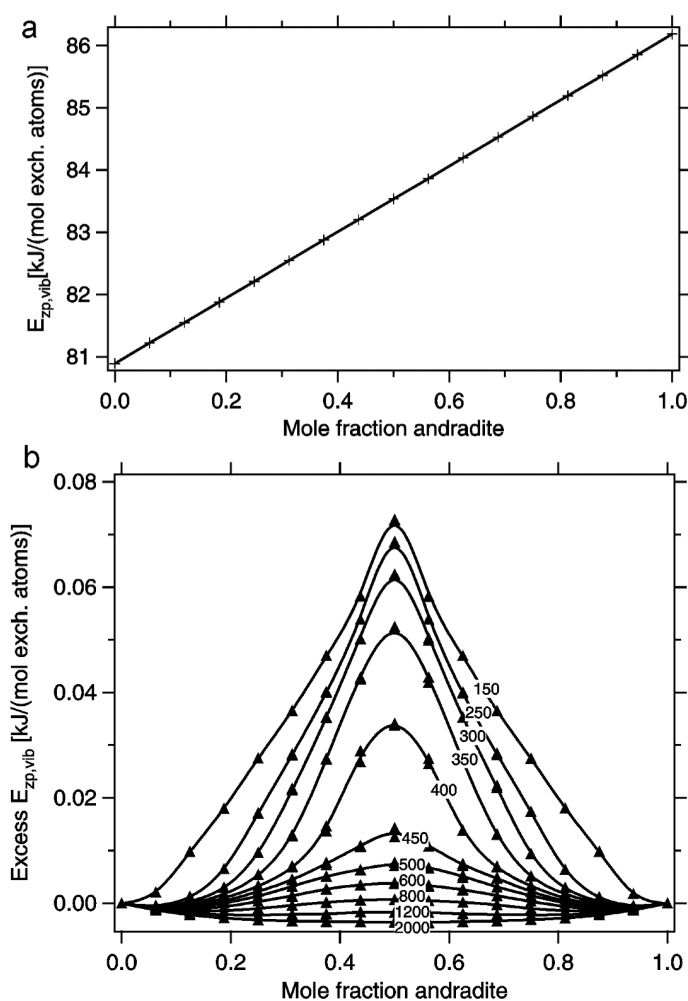


Figure 2.11: Calculated vibrational zero-point energies of mixing. **a** Absolute values and **b** excess values. The temperature dependence (*labels* in K) of the zero-point energies is due to averaging over different configurations that are likely to occur at different temperatures.

In experimental TEM images, one typically observes interfaces  $\parallel(110)$  (previous section, and Hirai & Nakazawa, 1986). With the results of Table 2.5 in mind, it can be assumed that there must be other factors, in addition to the interface energy of an infinite interface in a certain direction, that controls the crystallographic directions of the interfaces. One factor could be the 'edge energy' of the edges that separate the crystallographically equivalent interfaces (e.g.,  $[110]$  and  $[\bar{1}10]$ ). Other factors that are beyond the possibilities of being modelled using molecular simulations (and therefore not extending unit-cell sizes of several tens of Å) may be strain

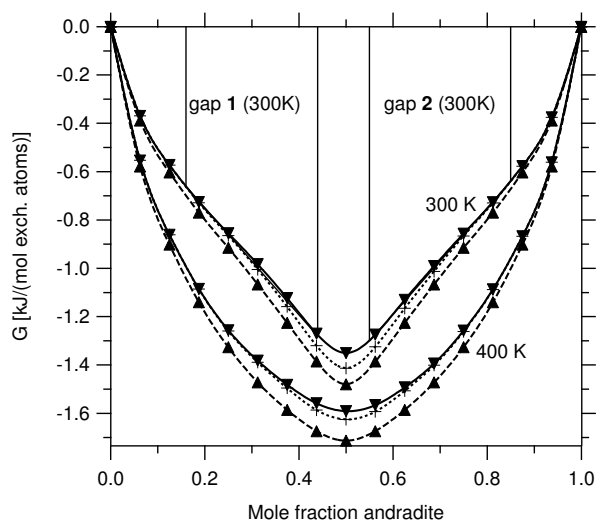


Figure 2.12: Free energies of mixing with contributions from the configurational energy of mixing ( $E_{conf}$ ; *dashed line*) + the contribution from the excess vibrational entropy of mixing ( $E_{conf} - T \cdot S_{vib}^{exc}$ ; *dotted line*) and the excess zero-point energy ( $E_{conf} - T \cdot S_{vib}^{exc} + E_{zp,vib}^{exc}$ ; *solid line*) for  $T = 300$  K and  $T = 400$  K. Both vibrational contributions together can change the total free energies of mixing by up to 10% for these temperatures. For  $T = 400$  K, the miscibility gaps for Al-rich (*gap 1*) and  $Fe^{3+}$ -rich (*gap 2*) garnets are indicated and lead to the miscibility gaps shown in Fig. 2.7.

Table 2.5: Interface energies for grossular–grandite and grandite–andradite interfaces. For these calculations, the interfaces were assumed to be sharp, that means that there is, e.g., no Fe in the grossular phase for a Gro–Gra interface. All values for an interface between the end members are always higher, indicating that andradite and grossular never have a common interface.

Interface	< 100 >	< 110 >	< 111 >
Gro–Gra	0.1557	0.5533	0.6258
Gro–And	0.6179	1.7607	2.1449
And–Gra	0.1557	0.5533	0.6258

effects (previous section, Allen & Buseck, 1988, and references therein) or solid–liquid interface effects occurring during the growth of the garnet oscillatory zones (see, e.g., Jamtveit *et al.*, 1995).

Another argument for why factors other than nearly coherent interfaces may play a role in compositional oscillations or birefringence is the anisotropy of the refractive index that can be caused by these garnet interfaces. The birefringence from the differences in the high-frequency dielectric constant matrix for some model interfaces has been estimated which

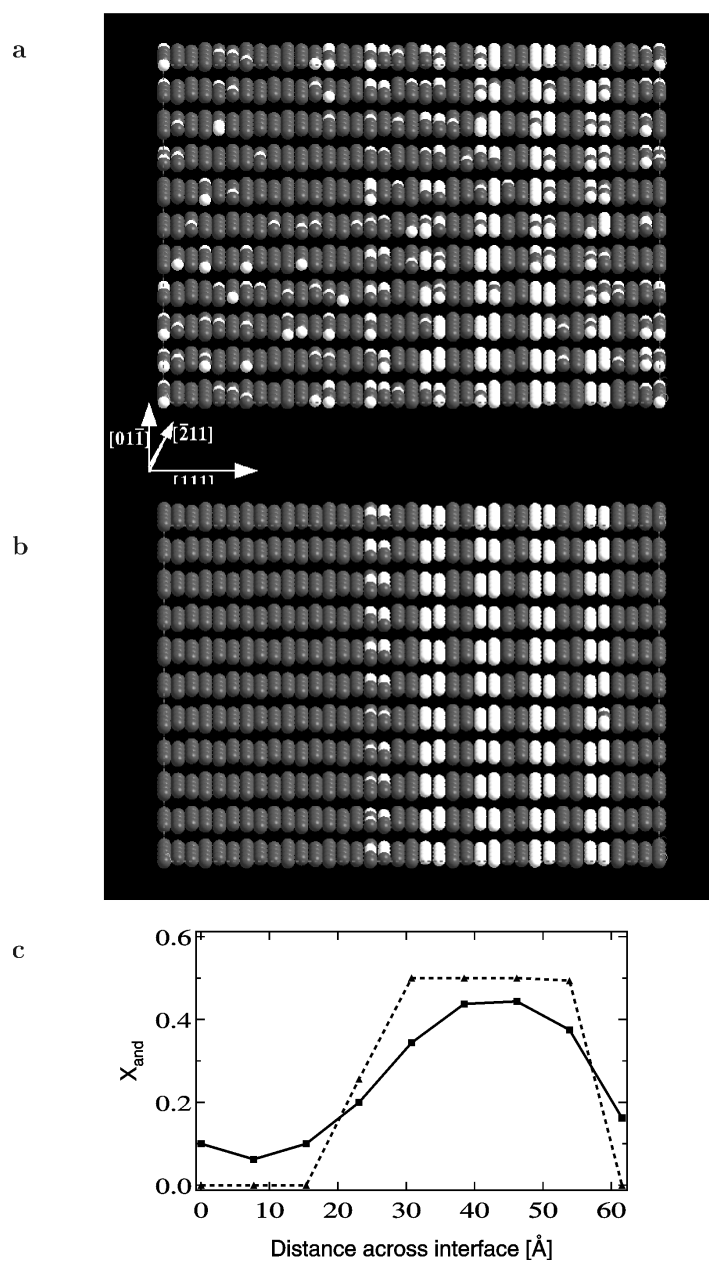


Figure 2.13: Interface  $\parallel (111)$  for an  $\text{Fe}^{3+}/(\text{Al} + \text{Fe}^{3+})$  ratio of 0.75 in a grossular-andradite solid solution (andradite:grandite ratio = 1:1). **a** Modelled at 300 K: there is a gradual change in the  $\text{Fe}^{3+}$  content from close to 0.5 to almost 1. The continuous gradient extends over approximately 20 Å (see also c). **b** Same concentrations as in a but modelled at 150 K. Only at theoretical temperatures below room temperature, could interfaces have an atomically sharp concentration gradient. **c** Concentration profile for the interface shown in a and b.

Table 2.6: Refractive indices for different garnets and garnet interfaces as derived from high-frequency dielectric constants.

Mineral or interface	$n(\perp)$	$n(\parallel)$	$n(\perp) - n(\parallel)$
Pure grossular	1.734	1.734	-
Pure andradite	1.887	1.887	-
Pure grandite	1.819	1.819	-
Grossular–andradite interface ( $\parallel < 100 >$ )	1.8136	1.8125	0.0011
Grossular–grandite interface ( $\parallel < 100 >$ )	1.77613	1.77603	0.0001
Grandite–andradite interface ( $\parallel < 100 >$ )	1.85287	1.85277	0.0001

are listed in Table 2.6. Table 2.6 shows that even for the extreme and unphysical case of a grossular–andradite interface with an infinite periodic setup of alternating grossular and andradite unit cells. However, observed birefringences can be on the order of 0.005 (Allen & Buseck, 1988; Kingma & Downs, 1989) up to 0.01 (Takéuchi *et al.*, 1982). Therefore, there must be additional factors, e.g., defects, noncubic ordering, strain, foreign atoms, that contribute to the optical anisotropy other than coherent interfaces with just compositional oscillations at thermodynamic equilibrium. It is interesting to note that not only the interface energies between grandite and one of the end members is on the order of the domain wall energies for  $\text{LaTiO}_3$  but also the birefringence of  $\approx 0.0001$  that we calculate for such an interface.

## 2.4 Discussion

Some of the thermodynamic and structural properties from our calculations of the solid solution appear to be different from experimental results in previous studies. Therefore, three main points can be addressed: (1) nonideality and miscibility gaps, (2) cation ordering in grandites, and (3) possible influences of formation conditions of natural grossular–andradite garnets in relation to thermodynamic equilibrium.

### 2.4.1 Nonideality and miscibility gaps

Engi & Wersin (1987) described the grossular–andradite solid solution with an asymmetric (subregular) Margules model based on phase equilibrium data from Huckenholz & Fehr (1982). They calculated a single miscibility gap between  $X_{and} = 0.42$  at 473 K with a critical solvus temper-



ature of 717 K at  $X_{and} = 0.18$ . In this study, a similar miscibility gap ( $X_{and} = 0.16 - 0.44$ ) has been determined for an annealing temperature close to room temperature (see gap 1 in Fig. 2.12, see also miscibility gap between grossular and grandite in Fig. 2.7). In addition, the calculations result in another miscibility gap at the same temperature at  $X_{and} = 0.55 - 0.85$ . In the calculations, there is only a small asymmetry of the phase diagram about  $X_{and} = 0.5$  which is caused by the asymmetry of the vibrational entropy, but not by the configurational free energy. The two calculated miscibility gaps have critical solvus temperatures of about 370 K at  $X_{and} \approx 0.25$  and  $X_{and} \approx 0.75$ , respectively.

The experimental and computational results are partly contradictory, but both have different shortcomings that have to be evaluated. The data based on experiments to date are not derived from direct measurements of the free energy of mixing (calorimetric data properties). The phase equilibrium data by Huckenholz & Fehr (1982) depend in a fairly sensitive way on the composition of the garnet solid solution which was determined using XRD measurements. Thus, these compositional data are dependent on a detailed knowledge of the excess molar volume of the solid solution. It has to be noted that two different regression equations were derived by Huckenholz & Fehr (1982) and Heuss-Aßpichler & Fehr (1997) for the lattice parameter of the solid solution (the one by Huckenholz & Fehr (1982) is shown in Fig. 2.4) whereas the synthesis conditions were the same. Thus, it has to be questioned to what degree thermodynamic equilibrium was reached for a given synthesis temperature. The compositional heterogeneity (zonation) within the crystals with intermediate compositions (Heuss-Aßpichler & Fehr, 1997) also hints at some degree of nonequilibrium. Crystals with intermediate compositions also grew to a much smaller size than crystals with end member composition. In contrast, for the computer experiments, one single crystal with periodic boundary conditions is considered. One of the disadvantages of the calculations may be the sensitive dependence of the thermodynamic mixing properties from the interaction parameters. In addition, the fit between the calculated lattice energies using GULP and the interaction parameters in this study was only fairly good with a correlation coefficient of  $\approx 0.91$ . This can cause, e.g., the critical solvus temperatures to be somewhat too low.

In order to resolve the discrepancy between the experiments and computer simulations, it would be desirable to use experimental results where the compositions of the garnets is independently determined, e.g., by using microprobe analysis (as, e.g., in Heuss-Aßpichler & Fehr (1997)) and redo

the phase diagram derivation. In addition, the compositional homogeneity of the crystals has to be carefully analysed.

To improve the quality of the computer results, the thermodynamic relationship between the end members and ordered grandite may have to be reevaluated because these relative energies are crucial for the derivation of a precise phase diagram. Additional information on the relative energies of grossular/ordered grandite/andradite may be gained from highly precise quantum-mechanical calculations. Due to the size of the unit-cell, these are computationally expensive and beyond the scope of this study.

Other future improvements may include temperature-dependent interaction parameters based on a large number of molecular dynamics simulations. In addition, other fitting schemes such as three-body interaction parameters may be considered which can also improve the interaction parameter fit. Three-body interaction parameters give more freedom to describe the asymmetry of the phase diagram about  $X_{and} = 0.5$ .

#### 2.4.2 Ordering in grandites

In the simulations presented, long-range ordering of Al-Fe<sup>3+</sup> on octahedral sites begins at temperatures below 500 K and leads to the noncentrosymmetric cubic space group P4<sub>1</sub>32 for ordered grandite (Table 2.4). In contrast, XRD refinements (Takéuchi *et al.*, 1982; Allen & Buseck, 1988; Kingma & Downs, 1989), assume centrosymmetric pseudocubic spacegroups ( $I\bar{1}$  and  $Fddd$ ) due to ordering even though the unit cells are nearly metrically cubic. A center of symmetry is assumed, because it was found that the average oxygen positions are close to those of a centrosymmetrical crystal. IR data by McAloon & Hofmeister (1993, 1995) did not indicate any deviation from cubic symmetry. Here, the different methods to determine space-group symmetry and ordering have to be considered. In the computer experiment, the ordering scheme and the initial temperature for the ordering depend on the interaction parameters (see Table 2.3) and the ordered grandite described in Table 2.4 is an ideal single crystal.

Akizuki (1984) described optical textures in grandite garnets that can be correlated to internal textures like ordered-disordered sectors or fine lamellae with compositional differences. These textures are thought to form during growth. In addition, very fine lamellae were reported from oscillatory zoned or iridescent garnets (previous section Hirai & Nakazawa, 1986; Ivanova *et al.*, 1998). Due to their spatial extent, these lamellae cannot be resolved using an optical microscope. All these fine structural inhomogeneities may be averaged in XRD refinements and yield an average or-

dering scheme which has not to be in accordance with the ordering in one homogeneous domain.

Many birefringent grandite crystals become isotropic when annealed for several days at about 1100 K (e.g., Takéuchi *et al.*, 1982). Even during slow cooling, they do not revert to anisotropic. The calculations presented here show that ordering takes place at about 500 K, where the kinetics of cation redistribution would be too sluggish to see a measurable effect even in geologic times. In addition, ordering is thought to take place during crystal growth controlled by steps on the growing surface (Gali, 1983; Akizuki, 1984; Allen & Buseck, 1988; Shtukenberg *et al.*, 2001b). This ordering has not to follow the ordering scheme described in this chapter because it occurs under nonequilibrium conditions and under the local symmetry of the growing face which is different from the bulk crystal symmetry. However, it would be preserved due to slow kinetics. Thus, the calculated ordering schemes that represent thermodynamic equilibrium may not be observable at all in natural grandites (presumed that the interaction parameters do not have to be rescaled) and, in addition, birefringence could be taken as an indicator for nonequilibrated crystal. The possible reasons for the birefringence (ordering during growth, strain from compositional interfaces) cannot be examined from this equilibrium-based calculation.

### 2.4.3 Hints to the formation conditions of natural grossular–andradite mixtures in relation to thermodynamic equilibrium

The results suggest that grossular–andradite solid solutions with significant heterogeneities such as inhomogeneous optical properties or oscillatory zoning are not in equilibrium. No exsolution and long-range ordering are expected in grandites grown under equilibrium conditions due to the low starting compositions for these processes. For oscillatory zoned grandites, two different hypotheses for the crystal growth process can be considered: compositional oscillations (1) reflect oscillating growth conditions (near-equilibrium growth) or (2) are caused by kinetic effects at the solid–fluid interface. The critical point for a near-equilibrium process is how to switch an external parameter (like  $p$ ,  $T$ , pH, etc.) to result in discrete compositions of different zones which occur over several length scales down to tens of nanometers. A miscibility gap would make it much easier to form oscillations even with small changes in external influences on the growth conditions, as demonstrated by Jamtveit (1991). Due to the calculations, however, the miscibility gaps would occur at very low temperatures. Thus, kinetic effects turn out to be more likely.



*“Die Natur zeigt sie uns, wir  
können Uebergänge einer  
Substanz in die andere  
nachweisen und haben in der  
Form einen festen Stützpunkt —  
allein wir vermögen nicht den  
Vorgang zu erklären, die  
Erfahrung der Chemie reichen  
nicht aus, die Untersuchungen  
der Geognosten sind in dieser  
Beziehung zu mangelhaft, es  
bleibt nichts übrig als zu  
gestehen, dass es so sey!”*

---

*aus* J. REINHARD BLUM:  
DIE PSEUDOMORPHOSEN DES  
MINERALREICHS (1843)

## Part II

# Replacement reactions



## Chapter 3

# An analytical TEM study on complex zoning patterns in garnets from Bergen Arcs eclogites

### 3.1 Introduction

The re-equilibration of a (metamorphic) mineral assemblages requires the redistribution of the chemical constitutions of the system. In this connection, the replacement of one mineral by another is a fundamental process that has been observed in almost any geological environment and that is most evident in retrograde metamorphism. Such replacement may be loosely termed cation (or anion) exchange reactions although the mechanism of such processes is not well understood. Generally, two types of processes may be expected: firstly, solid state diffusion, in which at least a part of the crystal structure is not affected by the process (not all crystal bonds were broken) and secondly, a coupled dissolution-precipitation process, in which the crystal is completely rebuilt. In the presence of a fluid phase coupled dissolution and reprecipitation is known to be kinetically a more effective process than solid state diffusion and has been demonstrated to occur in many cation and isotope exchange reaction (e.g., O'Neil & Taylor, 1967, 1969; Cardew & Davey, 1985; Cole, 2000; Putnis & Mezger, 2004; see Putnis, 2002, for review).

The transformation of mineral assemblages that occur as rocks are subducted, particularly the formation of eclogites, cause significant changes in

the petrophysical properties and therefore influence the geophysical signature as well as the geodynamics (e.g., Ahrens & Schubert, 1975; Le Pichon *et al.*, 1997). Such regional metamorphism is often viewed as a slow and continuous process that takes place over millions of years with the assumption that the rocks start to readjust to the equilibrium phase assemblage soon after a reaction boundary has passed (e.g., Thompson & England, 1984; Peacock, 1990; Spear *et al.*, 1991; Solelev & Babeyko, 1994). However, there is growing evidence from field observations, geophysical studies, and experimental investigations that quite often crustal rocks resist their transformation predicted by thermodynamic calculation (e.g., Oda *et al.*, 1990; Hori, 1990; Hacker, 1996; Kirby *et al.*, 1996; Baxter & DePaolo, 2000). The role of fluid and deformation for the transformation under eclogite-facies conditions have been emphasised in many studies (e.g., Austrheim, 1987; Wayte *et al.*, 1989; Rubie, 1990; Erambert & Austrheim, 1993; Austrheim *et al.*, 1997; Austrheim, 1998; Engvik *et al.*, 2001). However, the mechanisms of fluid-induced replacement reactions and the way of creating fluid-pathways under ultrahigh-pressure conditions are still poorly understood.

An impressive example of a re-equilibration process involving replacement reactions are the partially eclogised granulites on the island of Holsnøy in the Bergen Arc region of western Norway. The eclogised parts contain garnets that have been inherited from the granulite protolith. Although garnet is a stable mineral phase in both the granulite and the eclogite, it has to readjust its composition with respect to the Fe–Mg content. Various types of compositional zoning and replacement fronts can be observed representing a snapshot of the mineral re-equilibration. Here, an ATEM study on these replacement patterns in garnets is presented. The scope of the present work is to characterise the replacement front on a small scale and to evaluate the mechanisms that control garnet re-equilibration in such rocks. Furthermore, the intracrystalline microstructures of other granulite- and eclogite-facies minerals, which record information on the formation conditions, are described.

### 3.2 Geologic setting

The Bergen Arcs are a series of arcuate Caledonian thrust sheets and nappes centered around Bergen, western Norway. The island of Holsnøy, situated in the northwest part of the Bergen Arcs (Fig. 3.1), is part of the largest and most important of these sheets, Lindås Nappe, and is composed of abundant anorthositic rocks associated with mangerites and charnockites



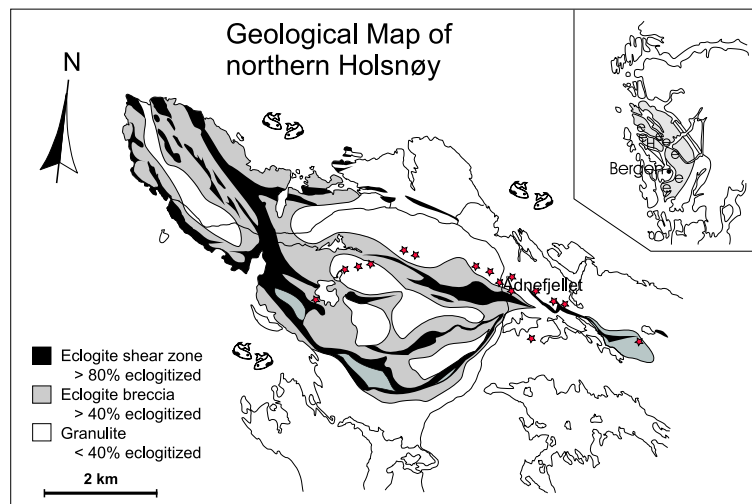


Figure 3.1: Geological map of the NW part of Holsnøy island showing the distribution of granulite and eclogite as well as major occurrences of pseudotachylyte (stars). The inset shows Lindås Nappe, a major tectonic unit of high-grade rocks of the Bergen arcs (grey). After Austrheim *et al.* (1996); Boundy *et al.* (1997), and field notes by A. Kühn, M. Lund, and M. Erambert.

(Austrheim & Griffin, 1985; Austrheim, 1987). It was metamorphosed under granulite facies conditions at temperatures of 800 – 900°C and pressures  $\sim 1.0$  GPa (depth of  $\sim 30$  km) in late Grenvillian time ( $\sim 945$  Ma; Austrheim & Griffin, 1985; Boundy *et al.*, 1997). Metamorphism and deformation produced anhydrous mineral assemblages dominated by garnet, pyroxene and plagioclase ( $An_{45-60}$ ) with noticeable foliation and a strong compositional layering of mafic bands with garnet and pyroxene alternating with layers dominated by plagioclase.

Between  $\sim 945$  Ma and  $\sim 420$  Ma, the complex cooled by an unknown amount. Then, during the Caledonian orogeny, it was subducted to eclogite-facies conditions facing pressures  $> 1.5$  GPa (depth of  $\sim 60$  km) and temperatures of 650 – 700°C (Austrheim, 1987; Boundy *et al.*, 1992; Jamtveit *et al.*, 1990; Van Wyck *et al.*, 1996). However, the ‘dry’ granulite mineral assemblage only partially transformed to a hydrous eclogite assemblages of omphacite ( $Jd_{50}$ ), garnet, amphibole, phengitic muscovite, kyanite, and zoisite/clinozoisite (Austrheim, 1987; Erambert & Austrheim, 1993). Eclogitisation occurred locally and spatially heterogeneous, and was limited by the availability of fluid which has been deduced to be  $H_2O$ -rich from phase equilibria (Jamtveit *et al.*, 1990; Boundy *et al.*, 2002). Thus, the eclogite formation can be considered as a retrograde process as it involves

re-hydration of the rock at temperatures lower than that of the granulite metamorphism.

### 3.2.1 Stages of eclogitisation

On Holsnøy, several stages of eclogitisation can be recognised. Eclogite facies rocks are found along fractures (millimetre–centimetre scale), in finger-like patches and as networked bands (centimetre–meter scale). In the vicinity of shear zones where the portion of eclogite is high, breccias of eclogite matrix surrounding discontinuous blocks of granulite (meter–ten meter scale) and areas of massive eclogite have been observed. The different stages of eclogitisation represent a rough chronology as well as a different relationship between fluid availability and deformation (Bjørnerud *et al.*, 2002). Since we are interested in the process of re-equilibration, the early stages of eclogitisation are of particular relevance as they show ‘metamorphism’ on small scale.

Along planar, meter-long fractures and veins eclogite developed symmetrically to about 1–50 cm thickness (Fig. 3.2). The central parts show the typical eclogite mineral assemblages with some phases symplectically intergrown which may suggest rapid reaction rates at high degrees of overstepping (Jamtveit *et al.*, 2000). However, relicts and pseudomorphs of granulitic minerals are commonly present. Especially, the garnets show a rich variety of replacement patterns as concentric rims, transecting curved bands, and along inclusion trails (see Fig. 3.3) which will be described in detail in section 3.3.1. Beyond the margins of the eclogised areas the granulite texture as well as the mineralogy is unaffected. Jamtveit *et al.* (2000) suggested that the margins represent the limits of self-propagating, fluid-catalysed reaction fronts. The granulitic foliation can be easily traced across the fracture and indicates the more ductile behaviour of the eclogitised part to deformation. Traverse cracks transect the fractures and die out shortly after the margins of the eclogite have been crossed. These cracks have been attributed to the volume decrease of 10–15 % associated with the conversion of granulite to eclogite.

## 3.3 Analytical methods and sample assortment

The garnets of various samples were examined by optical and scanning electron microscopy using polished thin sections. The conditions for BSE-imaging have been optimised for Z-contrast using high currents of 20–100 nA at 20 kV. Selected garnets were removed from the thin section by

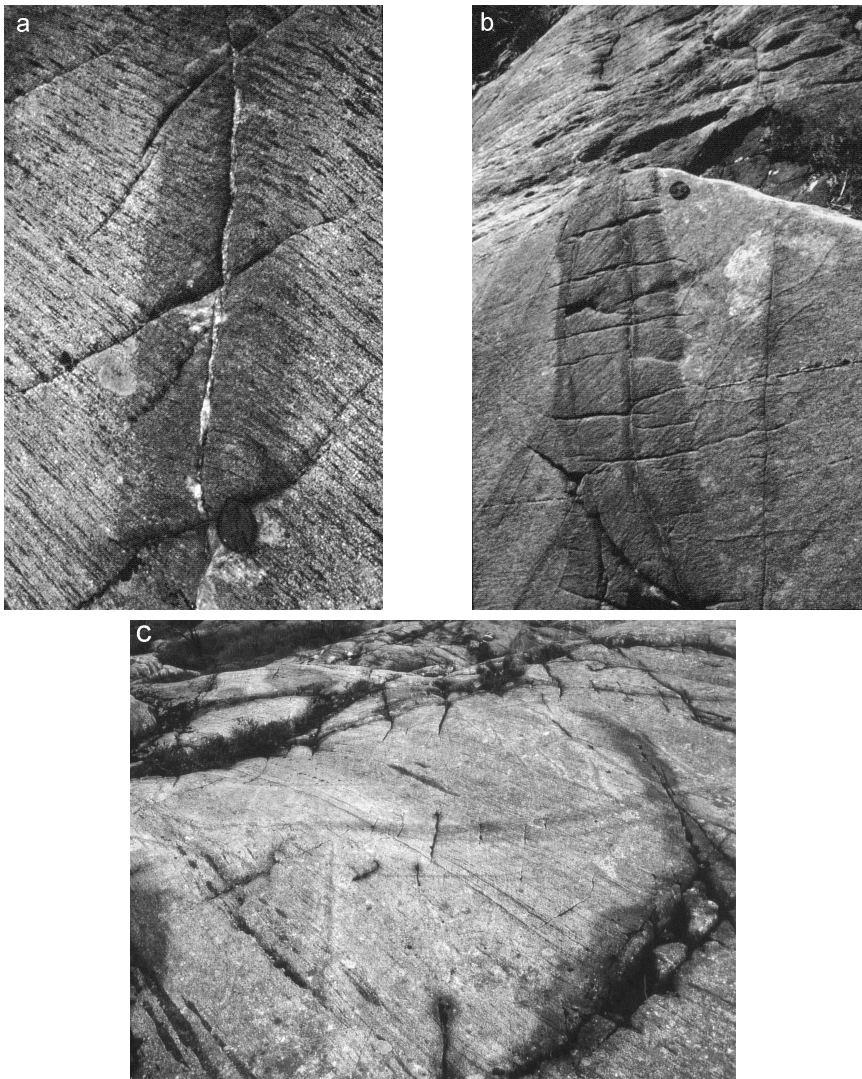


Figure 3.2: Examples for incomplete eclogite formation from granulites. **a, b** Fracture-related eclogite. The darker rock on either side of the fracture contains eclogite-facies mineral assemblages. The foliation in light-coloured granulite can be traced across the fracture. Transverse cracks are typical of these bodies and may be related to volume reduction associated with the conversion to eclogite. Note the different amount of transformed rock along the fracture in *b*. **c** Network of fractures without preferred orientation. Oblique cracks are always associated with the fractures. Field of view is  $\sim 10$  m.

a 3-mm diameter hollow ultrasonic drill and removed from the supporting glass using acetone. Copper grids have been glued on both sides of the sample to maintain its mechanical stability after ion beam thinning. Then, samples were prepared for TEM by ion beam thinning (Gatan Duomill 600)

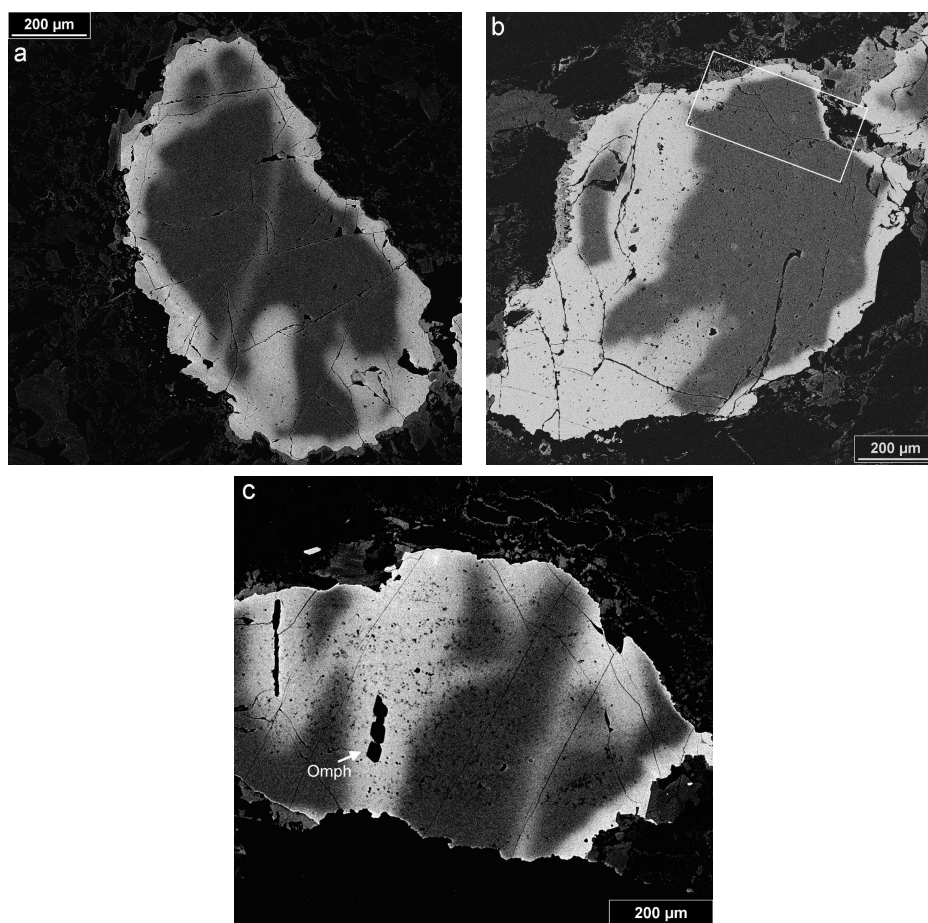


Figure 3.3: **a,b,c** BSE images of replacement patterns in garnets from eclogitic part. Zoning occurred as concentric rim zoning, embayments (*a, b*), transecting zoning bands (*a, c*), and along inclusion trails of predominantly omphacite (*c*). The lighter colour denotes a higher average atomic number of the garnet which is associated lower Mg/Fe ratio relative to the darker parts. The marked area on *b* is equivalent to the area in Fig. 3.6 *a*.

with Ar ions at 5 kV, 1 mA and an angle of incidence of 12–15° to the sample surface. Some sample have been cooled with liquid nitrogen during thinning to potentially decrease the effect of differential thinning of different phases and contamination/amorphisation in general. The positions of holes in each the sample were photographed at the optical microscope to correlate areas of analyses with BSE-images. ATEM was performed using a JEOL 3100 at 300 kV. Energy dispersive X-ray (EDX) analyses were performed using an Oxford Link Isis 300 System. Garnet compositions were calculated using experimental k-values.

### 3.3.1 Patterns in garnets

Various replacement patterns of garnets are shown in Fig. 3.3 and have been described by Erambert & Austrheim (1993) as follows. The composition of the garnet core is identical to the composition of garnet from the granulite facies protolith. In contrast, the rim composition has a lower Mg/Fe ratio that is in equilibrium with omphacite as denoted from the zoning in inclusion trails (e.g., Fig. 3.3c). There is no correlation between the width of the rim and the nature of the adjacent mineral. However, zoning tends to be more developed on the edges that are parallel to foliation than to those in pressure shadows. Inclusion trails as well as transecting bands are interpreted as microfractures that act as channels in which fluids strongly raise the element mobility (Jamtveit *et al.*, 2000). This interpretation highlights the importance of both deformation (formation of fractures) and fluid flows down to the grain-scale. Therefore, re-equilibration of garnets must strongly depend on both the presence of fluid and the density of cracks. However, for a throughout re-equilibration of garnet there still must be other mechanisms involved which can be either volume diffusion or a dissolution-reprecipitation process. An extensive knowledge of compositional changes connected with microstructural observation on the nm-scale is required to estimate the relative extent of these processes.

## 3.4 Results

### 3.4.1 Microstructure and compositional interfaces in garnets

Garnet crystals are relative poor in microstructure. TEM bright-field images show a small amount of dislocations and rarely the appearance of subgrain boundaries (Fig. 3.4). A distinction between the eclogitic and granulitic part by microstructure is not possible. Due to retrograde metamorphism chlorite is partly observed at some garnet rim. Surprisingly, an anastomosing feature has been observed in one sample (Fig. 3.5). This feature separates regions of different thickness but equal composition. Thicker regions are usually almost round and surrounded by the anastomosing "interface". The most likely explanation for this feature is the following. The particular sample has been cooled by liquid nitrogen during the ion thinning. From time to time the thinning progress had to be checked by taking out the sample from the ion mill. Since the sample is very cold ice crystallises immediately on it and often melts while the sample is inspected. Due to the poor mechanical stability of the partially thinned sample, com-

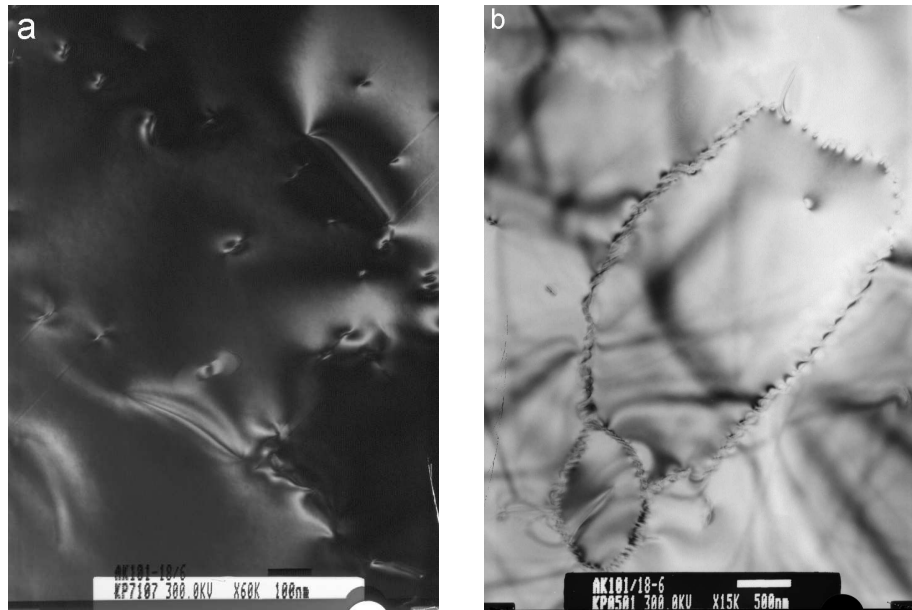


Figure 3.4: TEM micrograph of typical microstructures in garnet. **a** Single dislocations. **b** Dislocations forming a subgrain boundary.

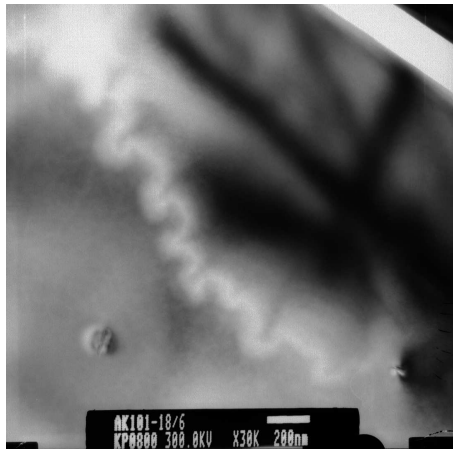


Figure 3.5: TEM micrograph of garnet. The anastomosing feature is most likely related to thickness differences achieved during ion milling. No difference in orientation of the crystal and composition is related to this. Although never reported so far it could concern a preparation artifact during ion thinning under cooled conditions.

plete drying before reinsertion is difficult. Therefore, little drops of water might freeze on the sample surface when the cooling is applied again. Because these part are now protected to thinning by ice they retain a higher thickness while the surrounding is further thinned. Thus, this feature is most likely a preparation artifact which to our knowledge has not yet been reported in the literature.

Systematic EDX-analyses (Fig. 3.6) show the transition from granulite ( $X_{alm} \sim 0.31, X_{pyr} \sim 0.50$ ) to eclogite garnet composition (up to  $X_{alm} \sim$

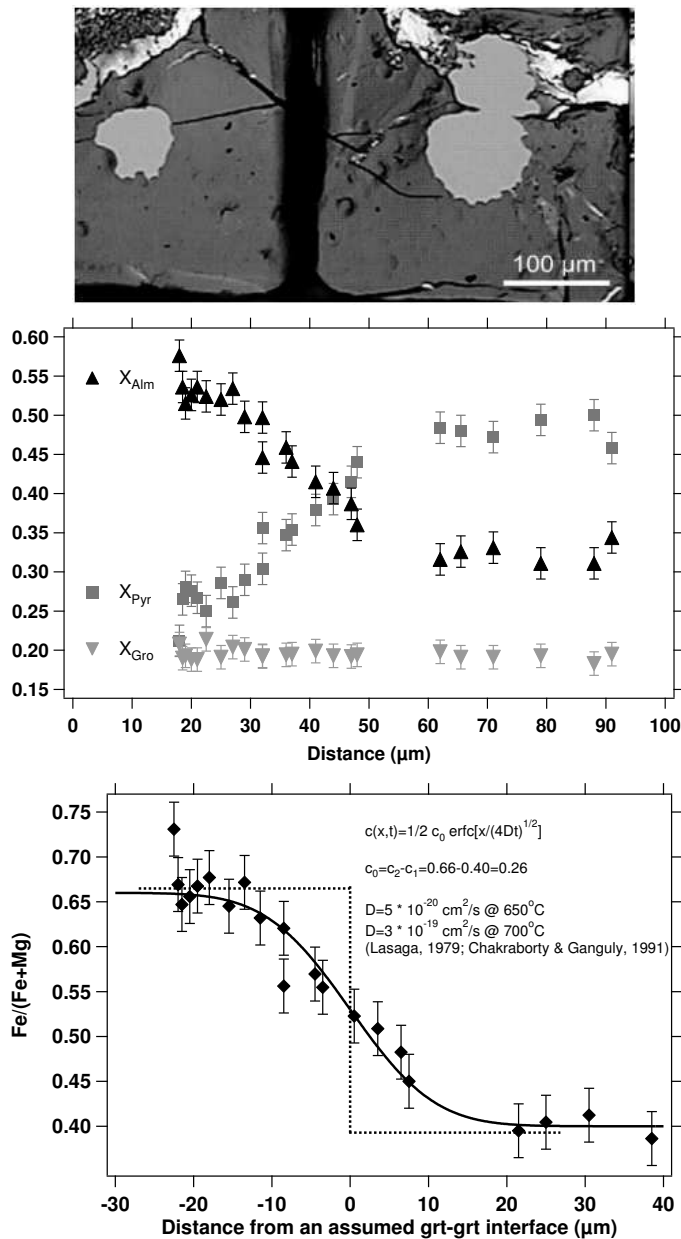


Figure 3.6: **a** Optical micrograph showing the positions of holes within the thinned garnet sample (cf. Fig. 3.3 *b*). **b** Systematic EDX-analyses around the hole on the left were traced back to a line perpendicular to the garnet rim. **c** Binary diffusion model (solid line) using measured boundary concentration ( $c_1, c_2$ ) and assuming a sharp interface between these compositions at time  $t=0$ . The position of the interface is chosen to obtain the best fit between the model and the profile.

0.54,  $X_{pyr} \sim 0.25$ ) within 40  $\mu\text{m}$ .  $X_{gro}$  is constant over the whole profile. The ATEM analyses confirm the width and shape of the compositional profile as previously measured using EMP by Erambert & Austrheim (1993). No distinct interface between the granulite and the eclogite garnet composition has been found.

Assuming the principal process of garnet re-equilibration is diffusion from rim, fractures and veins, time can be estimated using a simple geometry and the available diffusion coefficients. Since volume diffusion in garnet is isotropic, the penetration depths and the shape of the diffusion profiles should be the same at different areas within one crystal. The times calculated from this profile (Fig. 3.6c) are 4 Ma at 700°C and 23 Ma at 650°C, respectively. However, the thickness of the rims is very variable ranging from almost none to at least 200  $\mu\text{m}$  (see Fig. 3.3, especially b and c) whereas the diffusion distances denoted by the profiles are independent from the rim thickness. This could be taken as a hint that diffusion has smeared out an initially sharp interface in the further retrograde metamorphic history of the rock. It is obvious from the outcrop- to micro-scale that only the infiltration of fluid enables the replacement reaction to occur. Therefore, the calculated times cannot represent a thermal (cooling) history but have possibly recorded the timing and duration of the fluid-rock interaction. Due to the heterogeneous patterns of replacement, "classical" volume diffusion could not have been the main mechanism of re-equilibration.

In contrast, the replacement patterns of garnets show substantial similarities to those most likely caused by a dissolution-precipitation process (cf. Putnis, 2002). Such mechanism would imply dissolution of the parent crystal and precipitation of the replacement at a moving interface that proceeds from the rim to the core. Using dissolution constants for silicates at metamorphic conditions provided by Walther & Wood (1986) suggests that a replacement rim with a thickness of 50  $\mu\text{m}$  in garnet could be formed within a few thousand years. Such a duration of the fluid-induced metamorphic event is in line with results from a quasi-quantitative model for the various metamorphic processes leading to eclogitisation that limits the duration of the complete process at the Holsnøy rocks to a few ten-thousand years (Bjørnerud *et al.*, 2002). The mass transport for a coupled dissolution-precipitation process involves a fluid phase which has to be in contact to both the dissolving and precipitating sites of the crystal. The most obvious sign that such fluid-solid interaction at a moving interface is possible is the generation of porosity. Harlov *et al.* (2003) has shown that porosity generation in apatite is possible under conditions of 900°C and 10 kbar. However, porosity in the replaced parts of the garnets has not been ob-



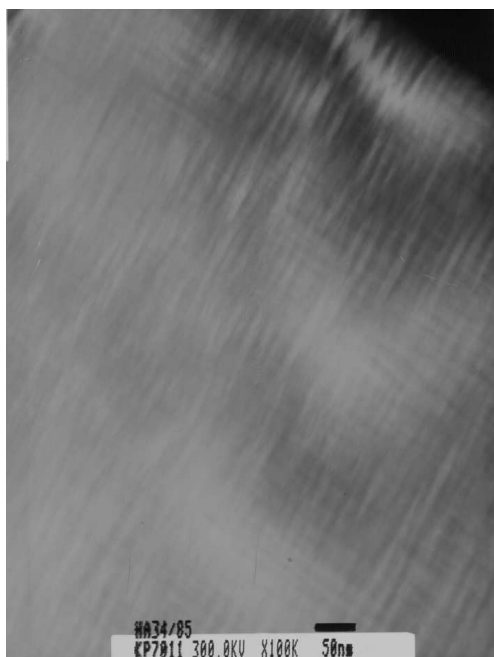


Figure 3.7: TEM micrograph of plagioclase (An<sub>45</sub>) showing exsolution within the Bøggild intergrowth known as 'tweed' structure. The lamellae are too small to be analysed without interference of adjacent parts.

served by ATEM. Conversely, it can not be concluded from this observation that there has not been any. Due to the further retrograde metamorphic history that has been gathered from the limited diffusion at the interface, sealing of pores and micro-fractures would be also possible. Hitherto, there are neither detailed studies on the local processes of the dissolution-precipitation reaction nor a profound knowledge on the textural characteristics associated with this process and their durability to, for example, temperature, pressure, deformation, and time.

### 3.4.2 Microstructures in plagioclase and omphacite

In plagioclase (An<sub>45</sub>) a characteristic 'tweed' pattern has been observed. This pattern is interpreted as begin of exsolution within the Bøggild intergrowth. The Bøggild intergrowth ranges from An<sub>40</sub> to An<sub>60</sub> and leads to incommensurate structures with compositions that differ up to 20% An (Putnis, 1992). Although the lamellae are too small to be analysed, the patterns are comparable to the observation of Olsen (1979) who reported similar 'tweed' structures for plagioclases with relatively low An-content.

The omphacite that has been grown after fluid infiltration under eclogite-facies conditions shows nice antiphase boundaries (APBs) which can be imaged using the  $h + k$  odd reflections. The antiphase bound-

ary is an interface within a crystal across which a mistake in the translational symmetry occurs (Putnis, 1992). The interface is generally curved and arises when a crystal transforms from a higher to a lower symmetry (in omphacite from  $C2/c$  to  $P2/n$ ) retaining a similar structure but with some transitional symmetry elements lost. The domain boundary therefore is a defect in the ordering pattern of such crystal. Carpenter (1981) emphasised that the size of regular equidimensional antiphase domains in omphacites appears to show a distinct trend such that the size increases with 'peak' metamorphic temperature (Fig. 3.9). He noted that this relationship could be used as a 'strange' geothermometer because only the temperature of growth is recorded and will not be reset during cooling. However, Van Roermund & Lardeaux (1991) showed that the size of the domains can be modified by deformational processes which causes coarsening and a wide variation in domain size. The domain sizes from omphacites of the Holsnøy eclogites fit the general trend by Carpenter (1981), although it must be emphasised that 'peak' metamorphic conditions can only be recorded where fluid and deformation caused the transition of the metastable granulite mineral assemblages.

Both the Bøggild intergrowth in plagioclase and the antiphase domains in omphacite suggests formation temperature lower than  $700^{\circ}\text{C}$ . Especially in regions of fracture-related eclogites (Fig. 3.2) substantial deformation after the formation of omphacite can be excluded. Thus, the microstructural observations are in line with temperature estimates for eclogites based on Fe-Mg exchange reaction between garnet and omphacite (Boundy *et al.*, 1992), heterogeneous phase equilibria (Jamtveit *et al.*, 1990), and  $\delta^{18}\text{O}$  equilibria between coexisting eclogite facies minerals (Van Wyck *et al.*, 1996).

### 3.5 Discussion

The Holsnøy rocks provide a fascinating window into the evolution of a rock system through a metamorphic transition. The anhydrous Holsnøy granulites may have existed metastably at eclogite-facies conditions for about  $10^5 - 10^6$  years prior to the onset of fluid-activated metamorphism (Bjørnerud *et al.*, 2002). Then, the eclogitisation takes place simultaneously by fracturing the rock even down to the grain-scale and fluid infiltration. Thus, introduction of fluids led to initially self-perpetuating eclogitisation processes involving amplifying feedbacks between deformation and metamorphism, with the duration of the main period of metamorphism lasting only tens to hundreds of thousands of years (Bjørnerud *et al.*, 2002).

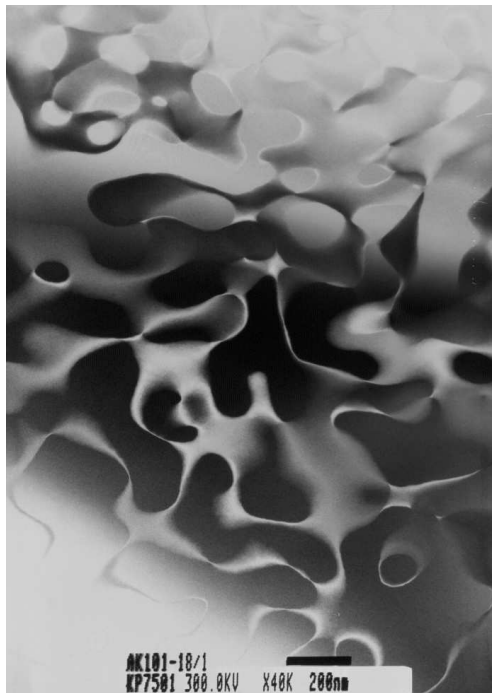


Figure 3.8: TEM micrograph showing antiphase domains in omphacite. Dark field image using a diffracted beam with  $h + k$  odd.

Both processes are mutually autocatalytic, i.e., fractures give pathways for fluids which by hydrofracturing and volume deficit reactions create new pathways. Therefore, these reactions can be described as producing ‘reaction enhanced’ permeability (Rumble & Spear, 1983; Cartwright, 1997) that trigger metamorphic reactions.

The re-equilibration mechanism at the grain-scale is also influenced by these processes, however since fractures not pervade down to any atom in a mineral, there must be other reactions involved. From the garnet replacement patterns it becomes obvious that diffusion can only be an accompanying process as the eclogitisation is not isochemically and fluid is necessary to make the mineral reactions possible. Furthermore, the calculated times for diffusion are in contradiction with the recent findings from large-scale eclogitisation simulation.

While the rocks on Holsnøy are an outstanding illustration of pervasive metastability, there is growing evidence that they are not exceptional. As summarised by Austrheim (1998), incomplete metamorphism is reported from a number of eclogite-bearing terranes. Recent studies in the Western Gneiss region of Norway (Engvik *et al.*, 2001; Krabbendam *et al.*, 2000) document incomplete reactions in gabbroic and mangeritic rocks which experienced pressure of at least 20–23 kbars. Some of these partly preserved bod-

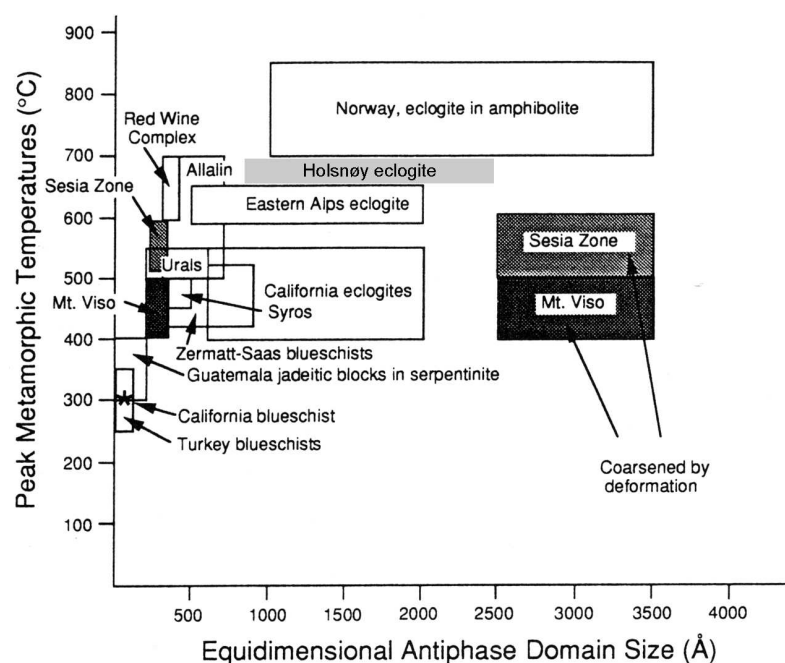


Figure 3.9: A graph relating the measured size of equidimensional APDs to the estimated peak temperature. The size of APDs in omphacites from Holsnøy island eclogites is marked in grey. Modified after Carpenter (1981) and Van Roermund & Lardeaux (1991).

ies in the Western Gneiss region may have been exposed to ultrahigh pressure (UHP) conditions ( $P > 25$  kbar) (Austrheim, 1998), but this question remains unresolved. Zhang & Liou (1997), however, report partial transformation of gabbro to coesite-eclogite in the Sulu UHP belt of eastern China, where metamorphic pressures in excess of 30 kbars have been estimated. This suggests that in some circumstances gabbroic rock can be subducted to depths of 90 km without reacting to eclogite. Ongoing work in the Western Gneiss region has further shown that the preserved gabbros are partially transformed to eclogite where fluids were introduced along fractures, in a manner resembling fracture-controlled eclogitisation on Holsnøy (Austrheim *et al.*, 1997). Furthermore, pseudotachylyte-like veins and fractures occur in these partially transformed bodies (Lund & Austrheim, 2001), suggesting that in the unconverted gabbros, as in the Holsnøy granulites, the eclogitisation process may have been triggered by seismic events.

The widespread persistence of metastable rocks at depth has significant implications for many fields in the solid earth sciences. Seismic interpretations of the deep crust, for example, are based on assumptions about

the relative importance of compositional versus metamorphic transitions in dictating seismic velocities (e.g., Solelev & Babeyko, 1994), and the undetected existence of buried but untransformed (or partially transformed) crustal rocks may lead to spurious conclusions. Geodynamic models of subduction, mountain building, and basin evolution often invoke densification of crust at prescribed depths, but these may need to be reexamined if large volumes of rock can resist thermodynamic re-equilibration. Incomplete acclimation of rocks to deep crustal conditions may also influence their subsequent uplift and exhumation (perhaps incompletely converted deep crustal complexes are returned to the surface more frequently than those that have equilibrated). The reconstruction of pressure-temperature histories and the very concept of metamorphic facies also become problematic if rocks can 'ignore' their deep crustal environments.

A growing amount of literature (e.g., Rubie, 1990; Zhang & Liou, 1997; Engvik *et al.*, 2001; Bjørnerud *et al.*, 2002; John & Schenk, 2003) documenting the importance of fluids and/or deformation in catalysing otherwise sluggish metamorphic reactions. A clearer understanding of the interactions among deformation, fluid migration, and metamorphic reactions is needed if we try to resolve the circumstances under which significant metastability is favoured. Therefore, an estimate on the parameter that control the kinetics of mineral reactions (isostructural as well as more heterogeneous one) is obviously required. Especially the connection between volume change during reaction and the way in which element are redistributed in complex system (fluid pathways) are critical in understanding any kind of mineral reaction and therefore metamorphism itself. Such a comprehensive approach considering small scale processes, kinetics, textural evolution, and thermodynamics can only be conducted by reducing the complexity of the system by using simple model systems and manageable experimental conditions.



## Chapter 4

# Volume changes of replacement reactions in solid solution-aqueous solution systems: Theoretical considerations on the example of the KBr – KCl – H<sub>2</sub>O system

### 4.1 Introduction

The replacement of one mineral by another is an important and striking phenomenon of mineral reaction in many geological environments. Thereby, the new mineral occupies the space and sometimes also the textural peculiarities of the former mineral. In the special case of pseudomorphism, the replacement is also recognised by preserving the euhedral shape of the former mineral. Although there are various scenarios for replacement reactions, we focus here on the replacement of a mineral by another with which it forms a solid solution.

Natural and experimental examples of replacements are commonly characterised by a sharp replacement front which proceeds as a moving interface. The preservation of the outer shape and, therefore, volume of the replaced crystal is a prerequisite to build a pseudomorph. The textural

inheritance implies that the rates of dissolution and precipitation should have been equal (Carmichael, 1986; Maliva & Siever, 1998; Merino & Dewers, 1998, and references therein). On the other hand, Ferry (2000) combined the molar volume change of the replacement reaction and the force of crystallisation concluding that a negative molar volume change as often observed in retrograde mineral reactions is a relevant factor to stabilise the replacing mineral. In general, volume changes associated with mineral reactions are of great importance in terms of the kinetics of re-equilibration. Negative volume changes have the ability to produce 'reaction enhanced' permeability (Rumble & Spear, 1983; Cartwright, 1997) that could create pathways for fluid and, therefore, might trigger and catalyse metamorphic reactions (see discussion in Chapter 3). In fact, microporosity was recognised in many cases [e.g transformation of leucite to analcime (Putnis *et al.*, 1994); cryptoperthite to coarse patch perthite (Walker *et al.*, 1995); chloro-, hydroxy-, fluoroapatite system (Yanagisawa *et al.*, 1999; Rendón-Angeles *et al.*, 2000a,b,c)] but in all these studies the cause of microporosity cannot be explained merely by a change in molar volume of the reactants.

The initial conditions for replacement reactions and the fluid compositions are usually unknown. The solubilities of the solid phases are generally affected by a number of variables, e.g., temperature, pressure, pH and, for solid solutions, by composition. To evaluate the effect of solubility changes, here, volume changes of replacement reactions will be calculated using a combination of Lippmann phase diagrams (Lippmann, 1977, 1980; Glynn & Reardon, 1990; Putnis *et al.*, 1995) and solubility diagrams (also called concentration or Schreinemaker's diagrams). The KBr – KCl – H<sub>2</sub>O system was chosen as a model system because of the relative simplicity and the available thermodynamic data.

Solubility diagrams are commonly used to describe experimental solubility data for simple salt systems (e.g., Glikin & Sinai, 1991, 1993; Glikin, 1995; Reeves *et al.*, 2000; Glikin *et al.*, 2003). Korzhinskii (1970) showed the use of this kind of diagram to describe metasomatic processes. It has the advantage that changes in relative amounts of phases can be determined simply and quantitatively.

In this study, the use of solubility diagrams is illustrated for the case of salt-water systems without solid solutions and relevant terms regarding the type of reaction are introduced. The description is then extended to systems with complete binary solid solution such as KBr – KCl. Here, equilibrium states in solid solution-aqueous solution (SS-AS) systems are represented in a modification of Lippmann phase diagrams, the *solubility phase diagram* (also called Treivus diagrams in the Russian literature (e.g.,



Azimov & Shtukenberg, 2000)), which consistently links the solubility diagram with the thermodynamic SS-AS description. General equations for reaction paths and the associated volume changes will be related. The calculated reaction paths in the KBr – KCl – H<sub>2</sub>O system will be analysed with particular regard to the evolution of the solid and aqueous composition and volume changes of the replacement as well as the kinetic constraints for the reaction. Subsequently, replacement experiments in the KBr – KCl – H<sub>2</sub>O with well defined starting conditions will be described. The experimental findings will be compared to and interpreted by the model to yield an estimate on the applicability of the model and a further insight on what parameters are important to understand replacement reactions a simple salt SS-AS system. The chapter closes with concluding remarks on the wider implications of the theory presented in regard to common features and aspects of natural replacement reactions.

## 4.2 Solubility and equilibrium in SS-AS systems: I. System without solid solution

Solubility diagrams are frequently used to visualise experimental solubility data in salt-water-systems (like NaCl – KCl – H<sub>2</sub>O) at a fixed temperature. The change of the solubility for one component (AB) depending on the amount of the second component (AC) is shown (Fig. 4.1). For phases which do not form a solid solution, each point on the solubility curve represents the composition of a saturated solution with respect to one solid phase, either AB or AC. At the isothermal invariant point *E* (eutonic point) the solution is saturated with respect to both phases. The intersections with the axes are the solubilities of pure AB (point *B*) and pure AC (point *C*) in water, respectively. Points below the curve represent undersaturated solutions.

A dissolution-precipitation reaction path of a AB crystal in a dilute solution ( $P_0$ ) is illustrated in Fig. 4.1. Dissolution of AB leads to an intersection with the solubility curve ( $P_1$ ) and the solution is now saturated with respect to AC. Further dissolution of AB must now be accompanied by the precipitation of AC and, therefore,  $P_1$  will be termed the start-point of the dissolution-precipitation reaction. The dissolution-precipitation reaction changes the solution composition and, therefore, approaches the eutonic point *E*. At this point, additional AB will not dissolve since the solution is saturated with respect to both AB *and* AC and is in equilibrium with

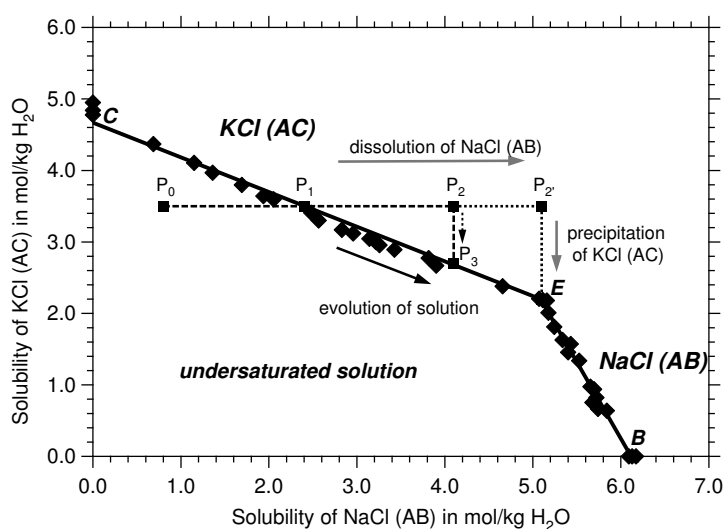
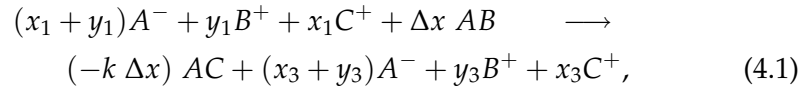


Figure 4.1: Solubility diagram of the NaCl – KCl – H<sub>2</sub>O system. Experimental solubility data were taken from Silcock (1979) and regressed linearly. Two dissolution-precipitation paths are shown ( $P_0$  to  $P_3$  and  $P_0$  to  $E$ ). The amount of material dissolved and precipitated depends only on the slope of the solubility curve.

respect to the two solids. This would be the end-point for the dissolution-precipitation reaction.

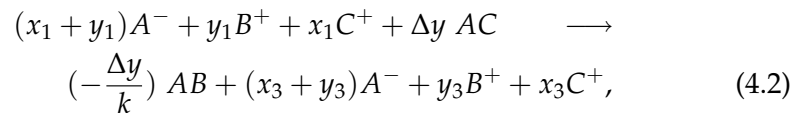
The amount of AC that will precipitate from a (super-)saturated solution is determined by the slope of the solubility curve. In the simplest case that the solubility curve is a line, the ratio of dissolved to precipitated material is constant and does not depend on how far the reaction proceeds. In terms of Fig. 4.1 the reaction can stop at some intermediate point  $P_3$  (e.g., by removing the solution) or end in equilibrium at the eutectic point  $E$  without changing the ratio of dissolved to precipitated material. This ratio is also not affected by the degree of supersaturation which is needed to precipitate a solid, i.e., the reaction can be seen as a virtual one-step dissolution-precipitation path from  $P_1$  via  $P_2$  to  $P_3$  or  $P_1$  via  $P_2'$  to  $E$ . Note that the real reaction path may never reach point  $P_2$  if a certain (lower) supersaturation leads to precipitation. Therefore, the real reaction path may follow the solubility curve more closely. If the solubility curve is not linear the ratio of dissolved to precipitated material depends on the end-point of the reaction (e.g.,  $P_3$  or  $E$ ) and is given by the slope of the line connecting the two points intersecting the solubility curve ( $P_1$  and  $P_3/E$ ). Again, the reaction can be considered as a one-step path since on the path towards  $E$  only AB dissolves and AC precipitates.

Therefore, the reaction can be written generally as



where  $\Delta x = (x_3 - x_1)$  and  $x_1, y_1$  and  $x_3, y_3$  are number of moles referring to the start-point  $P_1$  and the end-point  $P_3$  of the dissolution-precipitation reaction, respectively.  $k$  is the medial slope of the solubility curve between  $P_1$  and  $P_3$ .

For  $k > -1$  the number of moles of solid has decreased and the reaction will be termed a *deficit reaction*, for  $k < -1$  it has increased and the reaction is termed *excess reaction*. Referring to the solution the situation is vice versa. If a solution composition, due to the dissolution of AC, moves into the AB stability field the reaction can be written as



and consequently  $k < -1$  denotes now the *deficit* and  $k > -1$  the *excess reaction*.

The advantage of a solubility diagram is that changes of a coupled dissolution-precipitation reaction can be read off directly from the axes of the graph in absolute values such as number of moles (mol/kg H<sub>2</sub>O) or mass (g/100 g H<sub>2</sub>O) of the dissolved solid. Furthermore, the molar volume of a phase can be used to convert the axes to cm<sup>3</sup>/100 g H<sub>2</sub>O. Naturally, the slope changes by changing the units of the axes (e.g., from mol/kg to cm<sup>3</sup>/100 g H<sub>2</sub>O) depending on the ratio of the molar parameters of the two phases and it is possible that a reaction is a deficit-reaction in terms of the number of moles but is an excess-reaction in terms of volume or mass. Therefore, the slope of the solubility curve has different meanings when the units are changed. Note that volume units which can be read directly from the axes only refer to the dissolution and precipitation of the considered phase but do not refer to the chemical compound since polymorphs have generally different solubilities.

### 4.3 Solubility and equilibrium in SS-AS systems:

#### II. System with complete solid solution

In systems with complete solid solution every point on the solubility curve, i.e., any composition of a saturated solution, represents equilibrium with a

certain solid solution composition. However, the dissolution-precipitation paths cannot simply be deduced from the solubility diagram, because there is no information about the solid phase and its composition. A Lippmann phase diagram is commonly used to visualise SS-AS equilibrium states (Lippmann, 1977, 1980; Glynn & Reardon, 1990; Putnis *et al.*, 1995).

### 4.3.1 The Lippmann phase diagram

Thermodynamic equilibrium in a SS-AS system with binary solid solution is defined by:

$$[A^+][B^-] = K_{AB}a_{AB} = K_{AB}\chi_{AB}\gamma_{AB} \quad (4.3)$$

$$[A^+][C^-] = K_{AC}a_{AC} = K_{AC}\chi_{AC}\gamma_{AC}, \quad (4.4)$$

where  $[A^+]$ ,  $[B^-]$ , and  $[C^-]$  are the activities of  $A^+$ ,  $B^-$ , and  $C^-$  in the aqueous phase,  $K_{AB}$  and  $K_{AC}$  are the solubility products for pure AB and AC solids,  $a_{AB}$  and  $a_{AC}$  are the activities of the components AB and AC,  $\gamma_{AB}$  and  $\gamma_{AC}$  are the solid-phase activity coefficients, and  $\chi_{AB}$  and  $\chi_{AC}$  are the mole fractions of components AB and AC in the solid.

In a SS-AS system equilibrium is represented by two curves: the ‘solidus’ and the ‘solutus’ express the ‘total solubility product’ variable,  $\sum \Pi$ , as a function of solid composition and aqueous activity, respectively. The ‘total solubility product’ variable was introduced by Lippmann (1977, 1980, 1982) as

$$\sum \Pi = [A^+]( [B^-] + [C^-] ). \quad (4.5)$$

At equilibrium, the total solubility product as functions of the solid composition and the aqueous activity, respectively, is:

$$\sum \Pi_{eq} = K_{AB}a_{AB} + K_{AC}a_{AC} = K_{AB}\chi_{AB}\gamma_{AB} + K_{AC}\chi_{AC}\gamma_{AC} \quad (\text{solidus}) \quad (4.6)$$

and

$$\sum \Pi_{eq} = \frac{1}{\left( \frac{\chi_{B,aq}}{K_{AB}\gamma_{AB}} + \frac{\chi_{C,aq}}{K_{AC}\gamma_{AC}} \right)} \quad (\text{solutus}), \quad (4.7)$$

where  $\chi_{B,aq}$  and  $\chi_{C,aq}$  are the aqueous activity fractions.

Regular and sub-regular solid solution behaviour can be considered by introducing solid-phase activity coefficients  $\gamma_{AB}$  and  $\gamma_{AC}$  with the form of an expansion series (Guggenheim, 1937; Redlich & Kister, 1948):

$$\ln \gamma_{AB} = \chi_{AC}^2 [a_0 - a_1(3\chi_{AB} - \chi_{AC}) + a_2(\chi_{AB} - \chi_{AC})(5\chi_{AB} - \chi_{AC}) + \dots] \quad (4.8)$$

and

$$\ln \gamma_{AC} = \chi_{AB}^2 [a_0 - a_1(3\chi_{AC} - \chi_{AB}) + a_2(\chi_{AC} - \chi_{AB})(5\chi_{AC} - \chi_{AB}) + \dots], \quad (4.9)$$

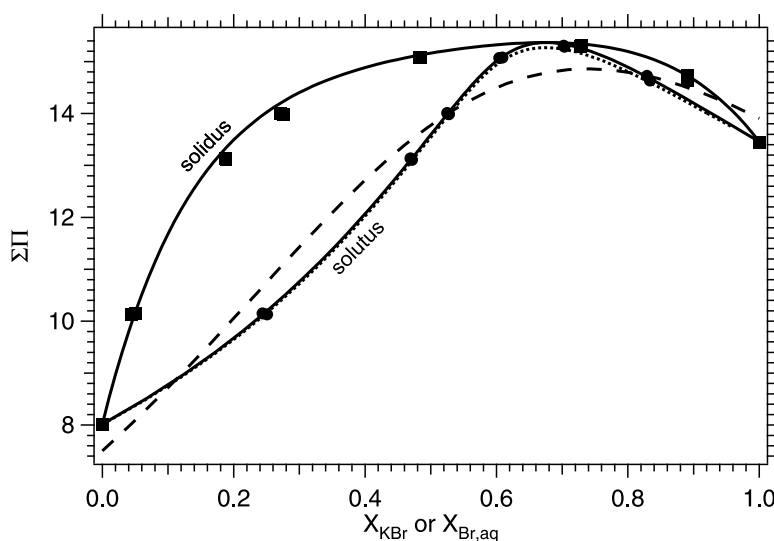


Figure 4.2: Lippmann diagram of the KBr-KCl-H<sub>2</sub>O system. The solid curves are the solidus and solutus curve fitted to the experimental data of Durham *et al.* (1953) ( $a_0 = 1.40$  and  $a_1 = -0.08$ ). The dotted curve (nearly indistinguishable from the solutus curve) is the solutus curve of the solubility phase diagram (Fig. 4.3 a) and the dashed curve is the polynomial fit (2. order) to the solubility data in the solubility diagram (Fig. 4.3 b) both converted to the Lippmann diagram using PHRQPITZ.

where  $a_i$  are dimensionless coefficients.

$\sum \Pi_{eq}$  is the value of the  $\sum \Pi$  variable which defines equilibrium for a given solid solution composition. In the Lippmann phase diagram (Fig. 4.2, for KBr – KCl), the  $\sum \Pi$  variable is represented on the ordinate whereas on the abscissa both the mole fraction of the solid and the aqueous activity fraction are given on a double scale. The solutus curve represents saturated solutions that are in equilibrium with a certain solid composition on the solidus curve. Horizontal tie-lines connect aqueous solution and solid solution compositions at equilibrium. The solidus and solutus expression have a strict thermodynamic meaning and can be fitted to experimental SS-AS data in cases where the activities of the aqueous complexes can be calculated. Fit parameters are the  $a_i$  coefficients. Several (commercial and free) programs are available to model solutions with different ionic strengths and within certain temperature intervals. However, care must be taken to the precision and internal consistency of the implemented thermodynamic data.

Because both the solutus curve *and* the solubility curve of the solubility diagram represent saturated solutions every point on the solutus curve corresponds to a unique point on the solubility curve and vice versa. Thus,

fitting of the solutus curve also determines the solubility curve. Unfortunately, the solutus curve cannot simply be converted into a solubility curve for the following reasons. Firstly, activities of the species in solution can only be determined with the assumption of  $[A^+] = [B^-] + [C^-]$  which may be true for some solutions but not generally. Secondly, from known activities of the species in solution one cannot simply calculate the concentrations of the elements because the ionic strength of the solution is not known a priori.

An apparently easy solution to the problem might be to fit the experimental data using a polynomial of second (or higher) order to obtain the solubility curve. However, due to the limited number of experimental data points this procedure does not lead to a good representation of the solutus curve (see Fig. 4.2). Moreover, it is theoretically not recommendable because the solutus curve has already been fitted using the Lippmann equations and, therefore, also the solubility curve is theoretically determined.

### 4.3.2 The solubility phase diagram

In the following, a modification of the Lippmann model is presented which uses experimental solubility data and does not require the calculation of the aqueous activities. It provides internally consistent expressions for the solubility and the solutus curve at the cost of introducing an additional empirical parameter which has to be fitted for every AB – AC – H<sub>2</sub>O system.

Rewriting of equations 4.3 and 4.4 using  $a_i = \gamma_i c_i$  leads to:

$$[A^+][B^-] = \gamma_{A^+}\gamma_{B^-}m_{A^+}m_{B^-} = K_{AB}\chi_{AB}\gamma_{AB} \quad (4.10)$$

$$[A^+][C^-] = \gamma_{A^+}\gamma_{C^-}m_{A^+}m_{C^-} = K_{AC}\chi_{AC}\gamma_{AC}, \quad (4.11)$$

where  $m_i$  and  $\gamma_i$  are the molality and aqueous activity coefficient of species  $i$ . Therefore, the molality of the anions is:

$$m_{B^-} = \frac{K_{AB}\chi_{AB}\gamma_{AB}}{\gamma_{A^+}\gamma_{B^-}m_{A^+}} \quad (4.12)$$

$$m_{C^-} = \frac{K_{AC}\chi_{AC}\gamma_{AC}}{\gamma_{A^+}\gamma_{C^-}m_{A^+}}. \quad (4.13)$$

If the solution is made by the dissolution of phases of the AB – AC solid solution, equal molalities of cations and anions ( $m_{B^-} + m_{C^-} = m_{A^+}$ ) are realized. With this assumption one can express the molality of  $m_{A^+}$  as

$$m_{A^+} = \sqrt{\frac{K_{AB}\chi_{AB}\gamma_{AB}}{\gamma_{A^+}\gamma_{B^-}} + \frac{K_{AC}\chi_{AC}\gamma_{AC}}{\gamma_{A^+}\gamma_{C^-}}}. \quad (4.14)$$

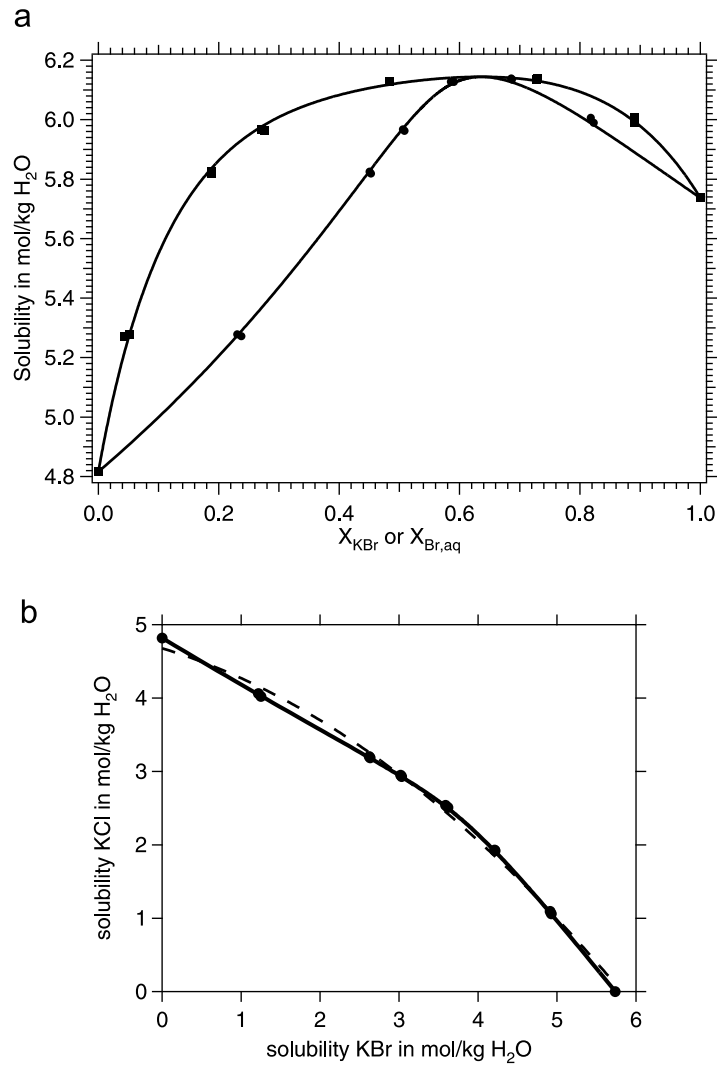


Figure 4.3: **a** Solubility phase diagram of the KBr – KCl – H<sub>2</sub>O system. Solidus and solutus curves have been fitted to the experimental data of Durham *et al.* (1953). The parameter of the fit are  $\Psi = 2.42$ ,  $a_0 = 1.40$  and  $a_1 = -0.08$ . **b** Solubility diagram of the KBr – KCl – H<sub>2</sub>O system. The solid curve accord with the solutus curve in **a**. The dashed curve is a polynomial fit (2. order) to the experimental data (cf. Fig. 4.2).

Referring to a solution saturated only with pure AB or AC leads to relationships of the end member solubilities  $s_{AB}$  and  $s_{AC}$ :

$$m_{A^+}^0 m_{B^-}^0 = \frac{K_{AB}}{\gamma_{A^+}^0 \gamma_{B^-}^0} = s_{AB}^2 \quad (4.15)$$

$$m_{A^+}^0 m_{C^-}^0 = \frac{K_{AC}}{\gamma_{A^+}^0 \gamma_{C^-}^0} = s_{AC}^2 \quad (4.16)$$

The aim is now to originate a connection between the molalities in the mixed solution and the solubility of the end members (i.e., between equations 4.12 – 4.14 and equations 4.15 and 4.16. To correct empirically for the differences of ionic strengths and the ion activities in pure and mixed solutions, Azimov & Shtukenberg (2000) replaced the exponent 2 and  $\gamma_i \neq \gamma_i^0$  in equations 4.15 and 4.16 by an empirical exponent  $\Psi$  and set  $\gamma_i = \gamma_i^0$ :

$$m_{A^+} m_{B^-} = \frac{K_{AB}}{\gamma_{A^+} \gamma_{B^-}} = s_{AB}^{\Psi} \quad (4.17)$$

$$m_{A^+} m_{C^-} = \frac{K_{AC}}{\gamma_{A^+} \gamma_{C^-}} = s_{AC}^{\Psi}. \quad (4.18)$$

At equilibrium the molality of  $A^+$  in the solution is equal to the total solubility of the solution since  $m_{B^-} + m_{C^-} = m_{A^+}$ . Rewriting equation 4.14 with equations 4.17 and 4.18 gives an analogue to the solidus in the Lippmann model:

$$s_{eq} = m_{A^+_{eq}} = \sqrt[\Psi]{s_{AB}^{\Psi} \chi_{AB} \gamma_{AB} + s_{AC}^{\Psi} \chi_{AC} \gamma_{AC}} \quad (4.19)$$

Equally, there is an analogous expression of the solutus:

$$s_{eq} = \sqrt[\Psi]{1 / \left( \frac{\chi_{B,aq}^m}{s_{AB}^{\Psi} \gamma_{AB}} + \frac{\chi_{C,aq}^m}{s_{AC}^{\Psi} \gamma_{AC}} \right)} \quad (4.20)$$

where  $\chi_{B,aq}^m$  and  $\chi_{C,aq}^m$  are the aqueous mole fractions. They are defined as:

$$\chi_{B,aq}^m = \frac{m_{B^-}}{(m_{B^-} + m_{C^-})} = \frac{s_{AB}^{\Psi} \chi_{AB} \gamma_{AB}}{s_{AB}^{\Psi} \chi_{AB} \gamma_{AB} + s_{AC}^{\Psi} \chi_{AC} \gamma_{AC}} \quad (4.21)$$

$$\chi_{C,aq}^m = \frac{m_{C^-}}{(m_{B^-} + m_{C^-})} = \frac{s_{AC}^{\Psi} \chi_{AC} \gamma_{AC}}{s_{AB}^{\Psi} \chi_{AB} \gamma_{AB} + s_{AC}^{\Psi} \chi_{AC} \gamma_{AC}}. \quad (4.22)$$

The molalities of  $B^-$  and  $C^-$  at equilibrium which are necessary to calculate the solubility curve from the solutus are given by:

$$m_{B^-_{eq}} = \chi_{B,aq}^m s_{eq} \quad (4.23)$$

$$m_{C^-_{eq}} = \chi_{C,aq}^m s_{eq} \quad (4.24)$$

Azimov & Shtukenberg (2000) report exponents of  $\Psi$  in the range of 1.5–2.5 for various systems of well-soluble salts. Note that these authors have not used an expansion series to describe subregular solid solution. To make the results of the Lippmann and the solubility model as comparable as possible the expressions shown in equations 4.8 and 4.9 should be used. Using different forms for the solid-phase activity coefficient naturally affects the value of the exponent  $\Psi$ .



**Example: The KBr – KCl – H<sub>2</sub>O system**

For the KBr – KCl – H<sub>2</sub>O system experimental data (Durham *et al.*, 1953; Dejewski & Szymański, 1998) on the solubility (Fig. 4.3) and the coexisting SS-AS is available. The Lippmann phase diagram (Fig. 4.2) was calculated using equations 4.6 and 4.7 with the end member solubility products ( $K_{KBr} = 10^{1.129}$  and  $K_{KCl} = 10^{0.904}$ ) and the solid-phase non-ideality parameters ( $a_0 = 1.40$  and  $a_1 = -0.08$ ). They have been fitted previously by Glynn *et al.* (1990) to the data of Durham *et al.* (1953) using the PHRQPITZ aqueous speciation model (Plummer *et al.*, 1989) to calculate the the aqueous activities of  $K^+$ ,  $Cl^-$ , and  $Br^-$ .

For the solubility phase diagram (Fig. 4.3 a) the best fit to the experimental data was reached with an exponent  $\Psi = 2.35$  and non-ideality parameters  $a_0 = 1.36$  and  $a_1 = -0.10$  using end member solubilities of  $s_{KBr} = 5.74$  mol/kg H<sub>2</sub>O and  $s_{KCl} = 4.82$  mol/kg H<sub>2</sub>O. The non-ideality parameters are very similar to those of the Lippmann model and should, in fact, have identical values, since the models differ only in their description of the aqueous speciation. Therefore, using the non-ideality parameters  $a_0 = 1.40$  and  $a_1 = -0.08$  of the Lippmann model and fixing them during the fit results in  $\Psi = 2.42$  with no significant decrease in goodness of fit. For straightforwardness with respect to the Lippmann model the solubility phase diagram was constructed using the latter values of  $\Psi$ ,  $a_0$  and  $a_1$ . With equations 4.23 and 4.24 the solubility curve (Fig. 4.3 b) is calculated. Converting the solubility curve back into the Lippmann phase diagram (using PHRQPITZ) shows an excellent match to the Lippmann solutus curve (Fig. 4.2).

The solubility phase diagram now allows to describe reaction paths in the solubility diagram because it provides internally consistent information about the composition of a solid in equilibrium with an aqueous solution of certain composition. It must be emphasised that this is the prerequisite to deduce volume changes of replacement reactions quantitatively.

**Limitations of the solubility phase diagram**

Although the solubility phase diagram includes a semi-empirical parameter it reproduces the equilibrium relation in a Lippmann diagram very well. However, there are drawbacks which limit the wider use of such diagrams for complex systems: (1) as noted before, the molality of cations and anions in aqueous solution which form the solid solution must be equal, i.e., ( $m_{B^-} + m_{C^-} = m_{A^+}$ ). Hence, there must be stoichiometric portions of cation and anions in the solution. This problem can be easily avoided experimen-

tally but will be rarely fulfilled in 'real' solutions; (2) non-stoichiometric portions of elements as well as further species in a multicomponent solution affect the solubility of the solids. For multicomponent solutions the solubility data has to be determined for precisely the solution composition under consideration. For many systems it is difficult to obtain such equilibrium solubility data due to kinetic effects (e.g., in carbonate systems, Plummer & Busenberg, 1987); (3) solubility is also affected by textural properties such as grain size and microstructure as well as by the amount of trace elements and defects in the crystal structure.

The explicit use of solubility phase diagrams is limited to systems of well-soluble salts for which SS-AS equilibrium is achieved in relatively short times. For such systems the solubility phase diagram has the advantage over the Lippmann model that the ion activity must not be determined, thus, avoiding the problem of missing thermodynamic data for many elements (e.g., Si and Al).

#### 4.4 Volume change

A set of equations is presented to calculate the volume changes in SS-AS systems based on reaction paths in a solubility diagram with axes in mol/kg H<sub>2</sub>O (cf. Fig. 4.1 and 4.4a). The volume change of a dissolution-precipitation reaction is given by:

$$\Delta V_{d-p} = V_p - V_d = n_p V_p^M - n_d V_d^M, \quad (4.25)$$

with a change in number of moles of

$$\Delta n_{d-p} = n_p - n_d. \quad (4.26)$$

The subscripts d and p refer to dissolution and precipitation, respectively, and d-p refers to the whole reaction. The volume change can be subdivided into two contributions, namely the change in number of moles during the reaction and the volume change due to the difference in molar volume, respectively:

$$\Delta V_{d-p} = V^{\Delta n} + \Delta V^M. \quad (4.27)$$

For a deficit reaction ( $\Delta n_{d-p} < 0$ ) they are

$$V^{\Delta n, def} = \Delta n_{d-p} V_d^M, \quad (4.28)$$

$$\Delta V^{M, def} = n_p (V_p^M - V_d^M), \quad (4.29)$$

and the volume change of an excess reaction ( $\Delta n_{d-p} > 0$ ) is by analogy given by

$$V^{\Delta n, exc} = \Delta n_{d-p} V_p^M \quad (4.30)$$

$$\Delta V^{M, exc} = n_d (V_p^M - V_d^M). \quad (4.31)$$

Note that deficit and excess reactions can both lead to a decrease or increase in volume depending on the molar volume of the considered phases. A deficit reaction is always a volume deficit reaction when the molar volume of the precipitated phase is smaller than that of the dissolved phase. An excess reaction is always a volume excess reaction when the molar volume of the precipitated phase is greater than that of the dissolved phase. In all other cases it depends on which contribution (see equation 4.27) is dominant.

To estimate the extent of a volume deficit or excess reaction the absolute volume change given by equation 4.25 is not very meaningful since the volume change is not related to the volume dissolved. For that the relative volume change  $\Delta V_{d-p}^r$  can be expressed in % as

$$\Delta V_{d-p}^r = \frac{V_p}{V_d} \cdot 100 - 100 = \frac{n_p V_p^M}{n_d V_d^M} \cdot 100 - 100, \quad (4.32)$$

whereby a positive value denotes volume excess and a negative denotes volume deficit. Note that in the case of a volume deficit reaction the relative volume change can be texturally denoted as porosity  $\phi$  which has the same absolute value but positive sign.

Furthermore, dissolution of the initial crystal takes place in a dilute solution to reach the solubility curve ( $P_0$  to  $P_1$ ). The volume dissolved to get a saturated solution and start the dissolution-precipitation process is

$$V_{diss} = \Delta n_{P_0 \rightarrow P_1} V_d^M. \quad (4.33)$$

In a system without solid solution or ideal solid solution the axes of the solubility diagram can be easily converted to the solubility of the phases in  $\text{cm}^3/\text{kg H}_2\text{O}$  using the end member molar volume to deduce the volume change of the reaction. If so, the dissolved and precipitated volumes,  $V_d$  and  $V_p$  (equation 4.25), as well as the volume dissolved to reach a saturated solution,  $V_{diss}$  (equation 4.33), can be directly read off from the solubility diagram as the length of the different paths. The slope of the solubility curve defines then the region in which a volume deficit or a volume excess reaction occurs. In systems with non-ideal solid solution the excess volume of mixing has to be considered, i.e. the solubility curve must be corrected

by the deviation from the additivity rule of molar volumes (Retgers' rule). The lattice parameter of the KBr – KCl solid solution are consistent with Vegard's rule, i.e., the solid solution is thus ideal in terms of the molar volume (Dejewska, 1999).

## 4.5 Reaction paths in the AB – AC – H<sub>2</sub>O system

In this section possible reaction paths for a generalised system (AB – AC – H<sub>2</sub>O) will be described. These reaction paths will be exemplary illustrated for the KBr – KCl – H<sub>2</sub>O system in Fig. 4.4. Point  $P_0$  represents a solution of certain composition which is undersaturated with respect to any solid. A crystal (AB) in contact with this solution will dissolve until the solubility/solutus curve is reached (at  $P_1$ ). This point is termed a 'primary saturation state' (e.g., Glynn *et al.*, 1990) which by definition lies on the solubility/solutus curve. From the solubility phase diagram the solid coexisting with this saturated solution can be determined using a horizontal tie-line to the solidus which gives the first (intermediate) composition precipitated. Since the initial solid (e.g., AB) is still not in equilibrium it will still dissolve. The ongoing dissolution of AB shifts the aqueous solution towards a more AB-rich composition on the solubility/solutus curve and a further solid precipitates with a higher  $X_{AB}^{repl}$ . Simultaneously, the first precipitate is no longer in equilibrium with the solution and has to readjust its composition. Therefore, both the composition of the solution and the precipitated solid will shift towards the dissolved component.

Assuming a reaction end-point at  $P_3$  at which equilibrium between the solution and all the precipitated solid has been reached (i.e., they can be connected by a horizontal tie-line in the solubility phase diagram and is compositionally homogeneous) a balance of the reaction in terms of the relevant components can be determined. The various dissolution/precipitation steps in which the solution closely follows the solubility/solutus curve can be summed up to an *effective* path where only the initial crystal (AB) dissolves up to  $P_2$  and the solid which is in equilibrium with  $P_3$  precipitates. Note that in general a certain supersaturation is necessary to precipitate any solid from a solution. For replacement reactions in the KBr – KCl – H<sub>2</sub>O system this overstepping is assumed to be small as both the initial crystal and the replacement can act as substrate for heterogeneous nucleation. Limits for the overstepping of the solubility curve have been reported to be 0.25 mol/l for KBr and 0.39 mol/l for KCl at 20°C (Tovbin & Krasnova, 1951). Therefore, the solution may not exactly

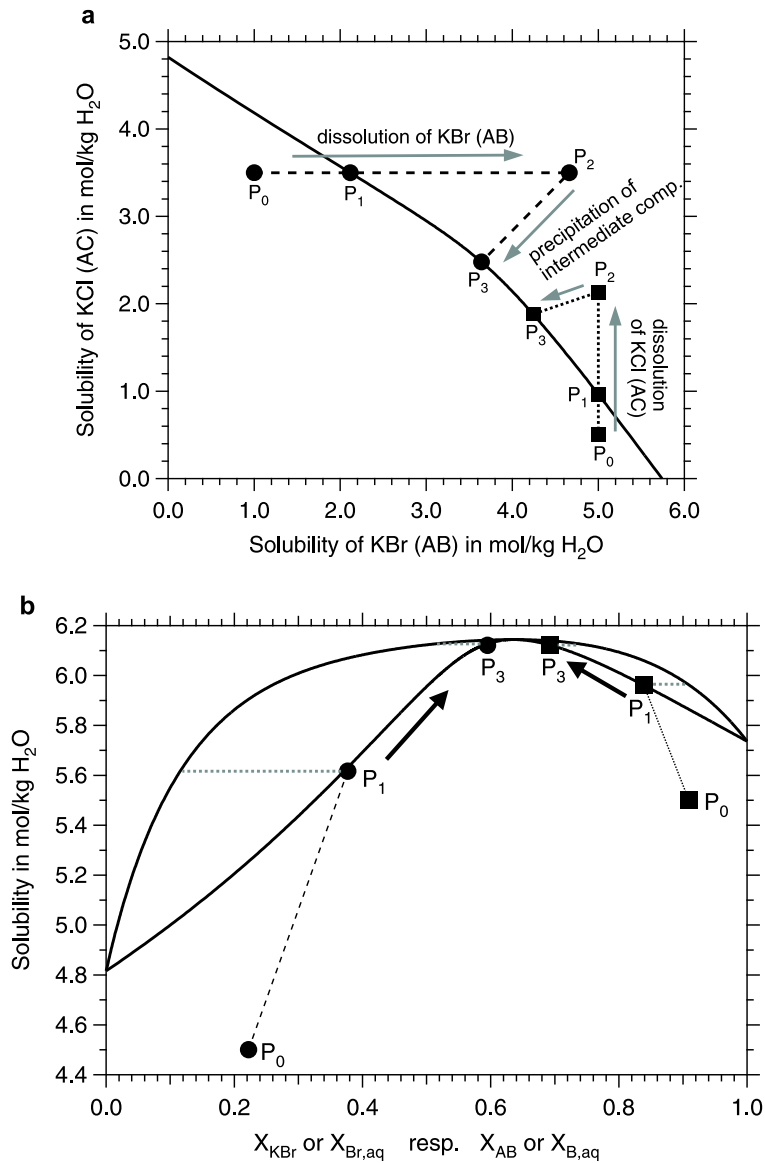
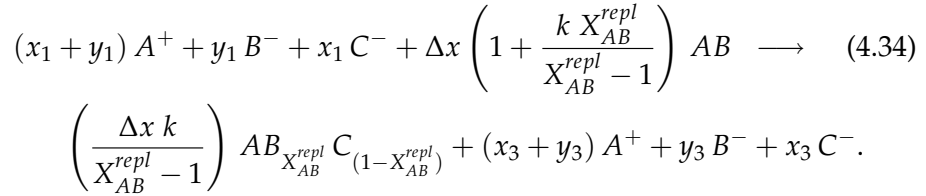


Figure 4.4: **a** Solubility diagram with reaction path samples for KBr (AB) dissolution ( $X_{Br}^{init} = 1.0$ , dashed line and circles) and KCl (AC) dissolution ( $X_{Cl}^{init} = 0.0$ , dotted line and squares). The replacement compositions (in equilibrium with solutions at  $P_3$ ) defining the slope from  $P_2$  to  $P_3$  are  $X_{AB}^{repl} = 0.50$  and  $X_{AB}^{repl} = 0.75$ , respectively. **b** The solubility phase diagram shows the compositional evolution of both solution and solid as the dissolution of the initial crystal proceeds.  $P_2$  is not shown in this diagram since this point is only needed for calculation purposes in the solubility diagram but will never be reached by a solution. The real reaction path is assumed to be always close to the solutus curve.

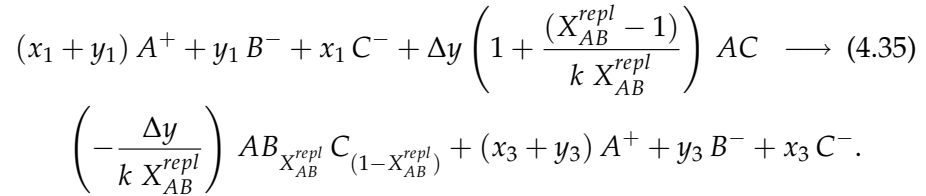
follow the the solutus line. Furthermore, the solid precipitating from a supersaturated solution may have not the same composition as the solid in equilibrium with the saturated solution (Prieto *et al.*, 1997). However, this effect is small for highly soluble substances and will not affect the effective reaction path for the replacement reaction.

If a compositionally homogeneous product is considered, the composition of the replacement,  $X_{AB}^{repl}$ , defines the path back to the solubility curve and, therefore, the slope of the line  $P_2$  to  $P_3$ . In addition, the composition of the initial crystal ( $X_{AB}^{init}$ ) and the initial concentration of the species in aqueous solution (at  $P_0$ ) are necessary to quantify the reaction path and the volume change.

A general reaction for the dissolution of AB in aqueous solution can be written (complementary to reaction 1) for a reaction path as in Fig. 4.4.



For the dissolution of AC the general reaction is:



The amount of solid dissolving and precipitating (i.e. the volume change) depends now on the medial slope of the solubility curve between  $P_1$  and  $P_3$  as well as on the composition of the solid precipitating, which can be determined by the solubility phase diagram (tie-line to  $P_3$ ). However, the general definition of the deficit and excess reaction (depending on the sign of  $k$ ) is still valid.

The equilibrium end-point of the reaction where the initial crystal is completely dissolved and the replacement is in equilibrium with the solution depends on the initial solution/solid ratio. A low ratio ( $n_{solution}/n_{solid} \Rightarrow 0$ ) leads to an end-point near to the composition of the initial solid. The composition of the solution changes substantially and therefore also the composition of the replaced solid changes significantly with time as the reaction proceeds. Considering the dissolution of AB the solution can only evolve towards higher B-content (because AB dissolves

and an intermediate solid precipitates) whereas for dissolution of AC the situation is vice versa. At high solution to solid ratio ( $n_{solution}/n_{solid} \Rightarrow \infty$ ) the solution composition is not affected by the dissolution of the crystal and remains unchanged. An almost fixed composition will precipitate during the whole dissolution-precipitation reaction. In cases of comparable amounts of solid and solution the aqueous composition shifts towards the composition of the highest solubility.

Where the reaction stops depends on the solution to solid ratio (equilibrium end-point) or on the time the reaction can occur (due to the availability of fluid). The latter can be seen as a non-equilibrium end-point because the initial crystal is not dissolved completely. In any case the calculated volume change refers to a compositionally homogeneous replacement which is in equilibrium with the current solution composition.

#### 4.5.1 Local volume change

In the previous analysis the dissolution-precipitation pathway from  $P_1$  to  $P_3$  was treated as a single step, neglecting the effect of progressive changes in the solution and replacement composition. To determine the volume change at the replacement front, the volume change of infinitesimally small reaction steps must be considered. This analysis is of great importance because it gives information about the relative kinetics of the replacement reaction especially in cases where the sign of  $k$  changes between the start and end-point of the reaction (i.e. that the reaction may change from a volume deficit reaction to a volume excess reaction or vice versa).

In this case  $P_1$  and  $P_3$  (see Fig. 4.4) virtually coincide and the volume change can be determined from the derivative of the solubility curve. It is based on the assumption that the solution composition is not affected by the dissolution of an (infinitesimal) small amount and the crystallization of the equilibrium replacement composition. This assumption is at least true in case of infinite solution to solid ratio for which the solution composition stays constant for the whole reaction. Therefore, the local volume change describes the volume change at the replacement front neglecting all contributions from former dissolution-precipitation substeps.

## 4.6 Reaction paths and volume changes in the KBr – KCl – H<sub>2</sub>O system

### 4.6.1 Dissolution of KBr in various solutions

Volume changes for reactions of KBr crystals in saturated solution of different composition have been calculated (equations 4.25-4.32 and 4.34). Fig. 4.5 a shows the volume change as a function of the composition of the replacement depending on the initial solution composition. As explained previously for dissolution of KBr the replacement composition and the solution composition always evolves towards higher Br-contents.

For pure KCl solution ( $X_{Br,aq}^{init} = 0.0$ ) the volume deficit can be over  $-40\%$  relative volume change (see Fig. 4.5 a) whereas the molar volume of KBr is only  $15.5\%$  higher than the molar volume of pure KCl. That clearly shows that most of the relative volume change is due to a loss of material to the solution as a result of the different solubilities of initial crystal and replacement. A significant negative relative volume change is always found for solutions with  $X_{Br,aq}^{init} < 0.7$ . However, with increasing  $X_{Br}^{repl}$  and increasing  $X_{Br,aq}^{init}$  the extent of the volume deficit decreases. For solutions with  $X_{Br,aq}^{init} \geq 0.7$  the relative volume change is positive (volume excess) but the extent is relatively small (up to  $0.3\%$ ). With increasing  $X_{Br}^{repl}$  the difference in molar volume between initial crystal and replacement becomes smaller (see Table 4.1), but will be always negative since the molar volume of KBr is always higher than the molar volume for any intermediate composition. However, for solutions with  $X_{Br,aq}^{init} \geq 0.7$  the negative change in molar volume is completely consumed by the mol excess reaction leading to a volume excess. For all solution compositions the calculated relative volume change converges towards zero for  $X_{Br}^{repl} \rightarrow 1$  because in the limiting case there is no compositional difference (i.e. no difference in molar volume and solubility) between the initial crystal and the replacement. As an example of the calculation of the data in Fig. 4.5 a, all parameters describing the volume change for KBr dissolution in pure KCl solution ( $X_{Br,aq}^{init} = 0.0$ ) are presented in Table 4.1.

#### Local volume change

Here, the volume change at the replacement front is calculated for the dissolution of KBr and represented as local volume change curve in Fig. 4.5 a. Note that all curves which describe the evolution of the relative volume



Table 4.1: Calculated parameters of volume change for the dissolution of KBr in initially pure saturated KCl solution ( $X_{Br,aq}^{init} = 0$ ).

$X_{Br}^{repl}$	$X_{Br,aq}$	$V_d^M$	$V_p^M$	$\Delta V_{d-p}$	$\Delta n_{d-p}$	$V^{\Delta n}$	$\Delta V^M$	$\Delta V_{d-p}^r$	$m_{KBr}^d$
		$\frac{\text{cm}^3}{\text{mol}}$	$\frac{\text{cm}^3}{\text{mol}}$	$\frac{\text{cm}^3}{\text{kg H}_2\text{O}}$	$\frac{\text{cm}^3}{\text{kg H}_2\text{O}}$	$\frac{\text{cm}^3}{\text{kg H}_2\text{O}}$	$\frac{\text{cm}^3}{\text{kg H}_2\text{O}}$	%	$\frac{\text{g}}{\text{kg H}_2\text{O}}$
0.050	0.231	43.27	37.75	-23.36	-0.4392	-19.00	-4.35	-43.96	146.1
0.100	0.350	43.27	38.04	-38.23	-0.7232	-31.29	-6.94	-43.09	244.0
0.150	0.422	43.27	38.33	-48.02	-0.9103	-39.39	-8.64	-41.74	316.4
0.200	0.470	43.27	38.62	-54.68	-1.0364	-44.84	-9.83	-40.09	375.1
0.250	0.503	43.27	38.91	-59.31	-1.1228	-48.58	-10.73	-38.24	426.6
0.300	0.529	43.27	39.20	-62.62	-1.1830	-51.19	-11.43	-36.24	475.2
0.350	0.548	43.27	39.49	-65.05	-1.2257	-53.04	-12.01	-34.12	524.3
0.400	0.565	43.27	39.78	-66.89	-1.2567	-54.38	-12.52	-31.89	576.9
0.450	0.580	43.27	40.07	-68.36	-1.2795	-55.36	-12.99	-29.55	636.1
0.500	0.594	43.27	40.36	-69.56	-1.2964	-56.09	-13.46	-27.10	705.8
0.550	0.609	43.27	40.66	-70.58	-1.3084	-56.61	-13.96	-24.53	791.2
0.600	0.625	43.27	40.95	-71.45	-1.3157	-56.93	-14.52	-21.83	900.2
0.650	0.644	43.27	41.24	-72.18	-1.3175	-57.01	-15.18	-19.00	1045.0
0.700	0.666	43.27	41.53	-72.75	-1.3123	-56.78	-15.97	-16.05	1246.3
0.750	0.692	43.27	41.82	-73.10	-1.2978	-56.15	-16.94	-13.03	1542.4
0.800	0.725	43.27	42.11	-73.14	-1.2704	-54.97	-18.17	-10.00	2011.5
0.850	0.768	43.27	42.40	-72.76	-1.2257	-53.03	-19.72	-7.05	2839.0
0.900	0.823	43.27	42.69	-71.81	-1.1572	-50.07	-21.73	-4.30	4589.1
0.950	0.897	43.27	42.98	-70.08	-1.0564	-45.71	-24.37	-1.90	10107.0

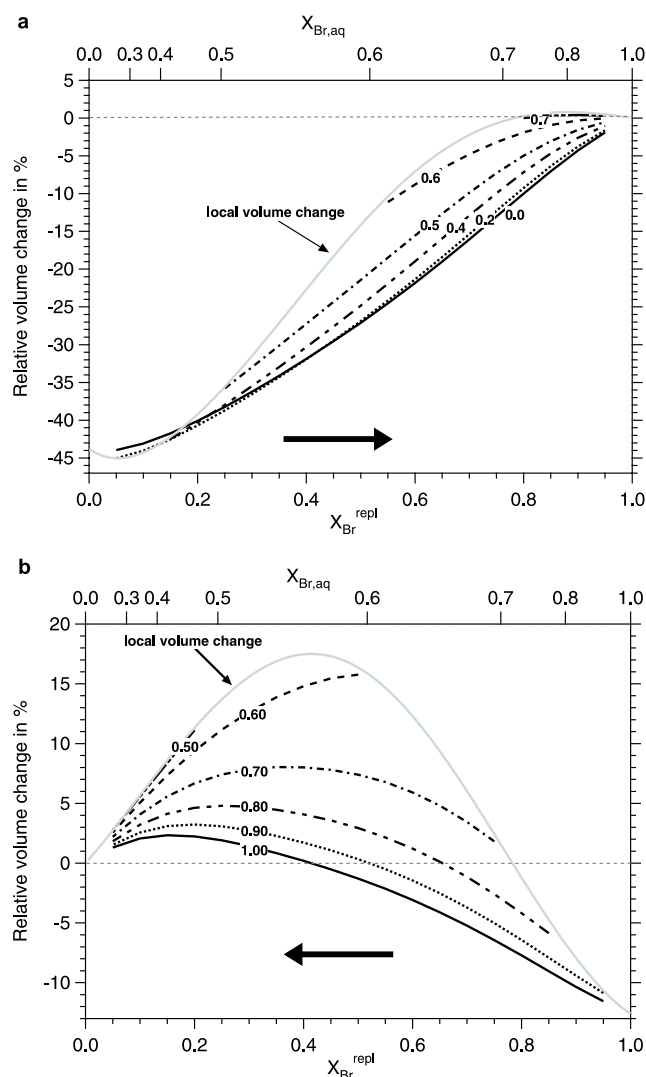


Figure 4.5: **a** Relative volume change for KBr dissolution in various solutions. During reaction the replacement composition will evolve to higher bromium contents as denoted by the arrow. The 'local volume change' curve represents an envelope from which all other curves emerge. **b** Relative volume change by KCl dissolution in various solutions. The compositional evolution of the replacement is opposite to *a*

change with changing solution composition have their starting point on this local volume change curve.

The differences between the calculations (local and compositional homogeneous) can be best explained by an example. The reaction path for KBr dissolution in a pure KCl solution ( $X_{Br, aq}^{init} = 0.0$ ) results at a replacement composition of  $X_{Br}^{repl} = 0.80$  in a relative volume change of  $-10\%$  denot-

ing a volume deficit reaction (Fig. 4.5 a and Tab. 4.1). This volume deficit is calculated for the whole reaction. Due to the limited supersaturation possible in the solution the reaction cannot be done in one step but must be subdivided in several reaction substeps. These involve the dissolution of the initial crystal and precipitation of the replacement plus a simultaneous re-adjusting of the replacement composition. The  $-10\%$  volume deficit is calculated over all these substeps if it results in a homogeneous replacement. Considering infinitesimal substeps the local slope of solubility curve controls the extent of volume deficit or volume excess *at the replacement front* and does not take into account a change of composition in the rest of the replacement (i.e. no re-adjusting of the former replacement compositions). In the first reaction substep (solution composition  $X_{Br,aq} = 0.00$ ) the relative volume change that is created is very high ( $\sim -44\%$ ). After some time the solution composition reaches  $X_{Br,aq} = 0.58$  (in equilibrium with replacement composition  $X_{Br}^{repl} = 0.45$ ). Considering the substep at this composition the relative volume change created *at the replacement front* is about  $-18\%$ . In contrast, the whole reaction from  $X_{Br}^{repl} = 0.0$  to  $0.45$  with all intermediate substeps and the averaged relative volume change for the whole replacement (if compositionally homogeneous) is on average about  $-30\%$ . At the end-point of  $X_{Br}^{repl} = 0.80$  the substep even provides a relative volume excess of  $0.3\%$  in contrast to the  $-10\%$  for the whole reaction. Generally, for dissolution of KBr the reaction type of the substep (at the replacement front) changes from volume deficit to volume excess when the solution composition reaches  $X_{Br,aq} = 0.71$  which is in equilibrium with  $X_{Br}^{repl} = 0.78$  independent of the initial solution composition.

#### 4.6.2 Dissolution of KCl in various solutions

The evolution of the relative volume change in various initial solution compositions is shown in Fig. 4.5 b. In the case of KCl dissolution the solution and replacement composition will always shift towards a more chlorine-rich composition. For an initially pure KBr solution ( $X_{Br,aq}^{init} = 1.0$ ) a negative relative volume change is calculated for  $X_{Br}^{repl} > 0.4$  starting with a volume deficit of over  $10\%$ . This is remarkable because the molar volume of the replacement is up to  $15\%$  higher than that of the dissolving KCl. For this replacement composition the extent of the deficit reaction widely exceeds the effect of differences in molar volume. The zero-crossing shifts with decreasing initial solution composition towards higher  $X_{Br}^{repl}$  and for solutions with  $X_{Br,aq}^{init} \leq 0.7$  the reaction has always a volume excess. The

Table 4.2: Calculated parameters of volume change for the dissolution of KCl in initially pure saturated KBr solution ( $X_{Br,aq}^{init} = 1$ ).

$X_{Br}^{repl}$	$X_{Br,aq}$	$V_d^M$ $\frac{\text{cm}^3}{\text{mol}}$	$V_p^M$ $\frac{\text{cm}^3}{\text{mol}}$	$\Delta V_{d-p}$ $\frac{\text{cm}^3}{\text{kg H}_2\text{O}}$	$\Delta n_{d-p}$ $\frac{\text{cm}^3}{\text{kg H}_2\text{O}}$	$V^{\Delta n}$ $\frac{\text{cm}^3}{\text{kg H}_2\text{O}}$	$\Delta V^M$ $\frac{\text{cm}^3}{\text{kg H}_2\text{O}}$	$\Delta V_{d-p}^r$ %	$m_{KCl}^d$ $\frac{\text{g}}{\text{kg H}_2\text{O}}$
0.950	0.897	37.46	42.98	-2.74	-0.1452	-5.44	2.70	-11.55	47.3
0.900	0.823	37.46	42.69	-4.47	-0.2460	-9.22	4.75	-10.35	86.0
0.850	0.768	37.46	42.40	-5.42	-0.3145	-11.78	6.36	-9.04	119.4
0.800	0.725	37.46	42.11	-5.80	-0.3592	-13.46	7.66	-7.72	149.6
0.750	0.692	37.46	41.82	-5.76	-0.3866	-14.48	8.72	-6.44	178.0
0.700	0.666	37.46	41.53	-5.42	-0.4011	-15.03	9.61	-5.23	206.1
0.650	0.644	37.46	41.24	-4.85	-0.4063	-15.22	10.37	-4.11	235.0
0.600	0.625	37.46	40.95	-4.12	-0.4045	-15.15	11.03	-3.08	266.1
0.550	0.609	37.46	40.66	-3.24	-0.3972	-14.88	11.64	-2.14	301.1
0.500	0.594	37.46	40.36	-2.22	-0.3852	-14.43	12.21	-1.29	342.0
0.450	0.580	37.46	40.07	-1.02	-0.3683	-13.80	12.78	-0.52	391.8
0.400	0.565	37.46	39.78	0.44	-0.3455	-12.94	13.38	0.19	455.0
0.350	0.548	37.46	39.49	2.29	-0.3146	-11.78	14.07	0.84	539.3
0.300	0.529	37.46	39.20	4.72	-0.2718	-10.18	14.90	1.43	657.5
0.250	0.503	37.46	38.91	8.02	-0.2116	-7.93	15.95	1.91	834.5
0.200	0.470	37.46	38.62	12.66	-0.1252	-4.69	17.35	2.24	1122.3
0.150	0.422	37.46	38.33	19.31	0.0009	0.04	19.28	2.33	1649.0
0.100	0.350	37.46	38.04	29.10	0.1880	7.15	21.95	2.06	2816.5
0.050	0.231	37.46	37.75	43.98	0.4720	17.82	26.16	1.30	6713.0

extent of volume excess can be up to 15 % and is caused by a combination of (positive) molar volume change and the mol excess reaction. Naturally, the relative volume change converges again towards zero when the replacement composition reaches the composition of the initial crystal.

### Local volume change

The volume change at the replacement front for KCl dissolution (Fig. 4.5b) shows both volume deficit (up to -12.5 %) and volume excess (up to 18 %). At  $X_{Br}^{repl} > 0.78$  ( $X_{Br,aq} > 0.71$ ) the deficit reaction dominates over the positive difference in molar volume whereas at  $X_{Br}^{repl} < 0.75$  the excess reaction and the molar volume change work in the same direction although the contribution of molar volume changes decreases to low  $X_{Br}^{repl}$ .

### 4.6.3 Kinetic considerations

Consider a replacement reaction (both dissolution and precipitation) that takes place on the surface of the original crystal. Then, only a part of the initial surface can be covered by the precipitated material, which provides pathways for the solution to stay in contact with the initial crystal. This pathway is commonly observed as porosity in the replaced part (e.g., Putnis, 2002, for review). Hence, as long as there is sufficient volume deficit the reaction can be assumed to be relatively fast. The dissolution of the initial crystal and the dissolution/precipitation of the replacement (due to the continuous change in the solution composition) take place simultaneously and should, therefore, result in a sharp replacement front. Further, the rate of compositional readjusting of the replacement itself must be autocatalytically correlated with the relative volume change because the higher the volume deficit the more surface area is in contact with the solution.

In contrast, in case of a volume excess reaction, the reaction stops completely because the initial crystal is armored to the solution. To proceed with the reaction solid state diffusion must be involved. Any diffusion into the replacement layer will bring this layer out of equilibrium with the solution and it has to readjust its composition. This could be done by dissolving the layer and precipitating a new phase in equilibrium with the current solution composition or by diffusion at the solid/fluid interface. The exact mechanism is not yet clear, but clearly the kinetics of a volume excess reaction must be very slow.

If the reaction type changes from volume deficit to volume excess *at the site of the replacement front* the rate of replacement should decrease significantly and also the ability of the replaced part to reequilibrate with the solution decreases. Hence, the kinetics of any reaction which traverses this composition (for the KBr – KCl – H<sub>2</sub>O system at  $X_{Br}^{repl} = 0.78/X_{Br,aq} = 0.71$ ) will change drastically independent from the earlier relative volume change. Taking this into account, calculated volume changes must be analysed with care when considering their role in constraining the kinetics of the reaction and the likelihood that the replaced part will recrystallize homogeneously.

Another kinetically important parameter is the amount of crystal (substrate) which has to be dissolved to reach a certain solution composition,  $m_{subs}^d$ . It is simply given by

$$m_{subs}^d = n_d m_d^M, \quad (4.36)$$

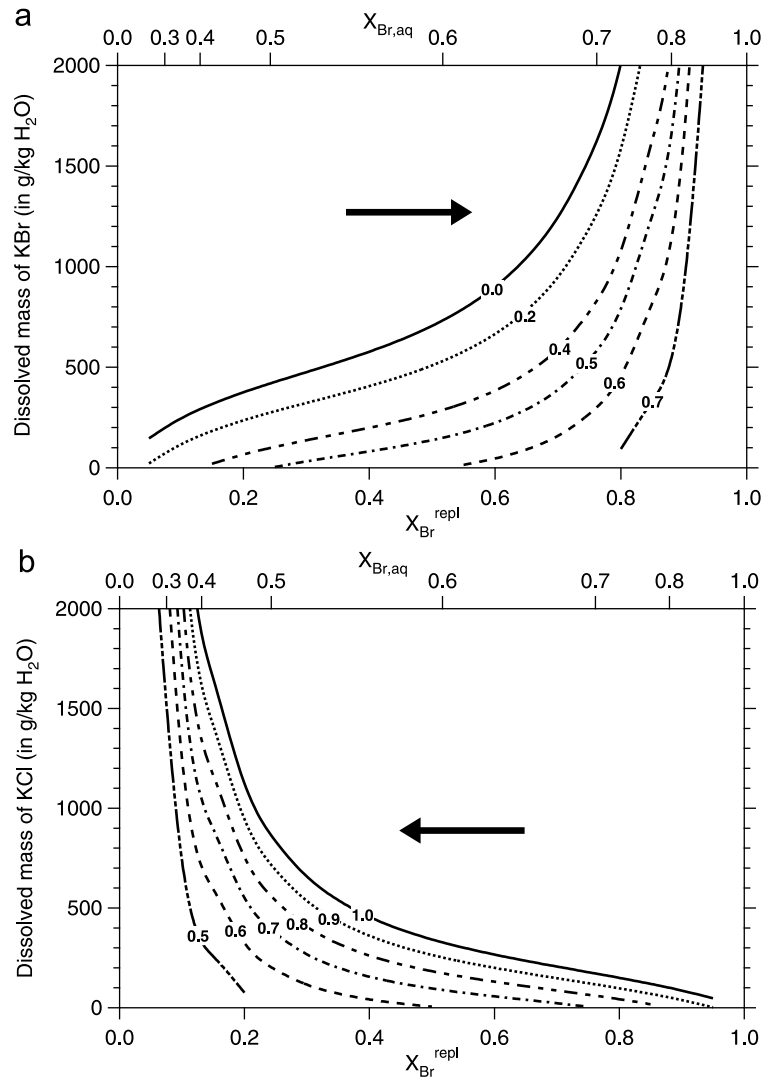


Figure 4.6: **a** Mass of KBr which has to be dissolved to reach a certain  $X_{Br, aq}$ . The compositional evolution of solution and replacement is denoted by the arrow. Up to  $X_{Br, aq} = 0.6$  relatively small amounts of dissolved KBr lead to a significant change in solution composition. The further evolution of the solution towards bromium-rich composition needs large amounts of KBr to be dissolved. **b** Mass of KCl which has to be dissolved to reach a certain  $X_{Br, aq}$ . The compositional evolution of the solution and replacement is opposite to **a**. From  $X_{Br, aq} = 0.5$  large amounts of KCl have to be dissolved to make the solution composition more chlorine-rich.

where  $m_d^M$  is the molar mass of the solid dissolving. Clearly, this amount is dependent on the initial solution composition and increases immensely when the solution composition transcends the alyotropic maximum towards the dissolving component (Fig. 4.6). In case of KBr dissolution, for higher

$X_{Br,aq}$  most of the dissolved bromium will be incorporated back into the replacement. Therefore, an initial solution with low  $X_{Br,aq}$  will change its composition significantly although only a small amount KBr is dissolved, whereas dissolving the same small amount of KBr in a solution with higher  $X_{Br,aq}$  changes the solution composition only lightly. Clearly, how fast the composition changes depends not only on the kinetics of dissolution but also on the solution to solid ratio. For the reaction path of KBr dissolution in pure KCl solution this implies that the replacement rate is fast at the beginning due to the volume deficit reaction but will slow down after some time since in addition to the decreasing volume deficit higher amounts of KBr must be dissolved to shift the reaction towards its equilibrium endpoint. In case of dissolution of KCl in KBr solution again the rate must be relatively fast at the beginning due to the volume deficit reaction but slows down quickly since the change in solution composition generates a switch to a volume excess reaction.

#### **4.7 Replacement experiments in the KBr – KCl – H<sub>2</sub>O system: Results and comparison with theory**

In this section results for replacement experiments in the KBr – KCl – H<sub>2</sub>O system will be described and interpreted in terms of the theory presented. In fact, the experimental observations and compositional analyses of the replacements were the stimulus to develop a theoretical description based on both the SS-AS relationships that in turn may explain the compositional evolution and the volume changes of a replacement that may explain the kinetic evolution of the system. A comparison between experiment and theory will be made to evaluate the feasibility of the theory presented in the previous chapters.

##### **4.7.1 Experimental procedure**

A series of replacement experiments were conducted by placing 50  $\mu$ L of KBr – KCl aqueous solutions of various compositions (Table 4.3) on freshly cleaved <100> surfaces of pure KBr and KCl, respectively. Such crystals were grown by evaporating KBr or KCl solutions and then cleaved to about  $3 \times 3 \times 1$  mm size. The solutions were in contact with the crystals for 5, 15, 25, and 60 minutes. Then the solutions were removed by blowing

Table 4.3: Starting solutions used in the replacement experiments.

Solution	[Cl] mol/l	[Br] mol/l	[K] mol/l	$X_{\text{Br,aq}}$
E1	4.052	0.0	4.052	0.0
S1	3.29	1.03	4.32	0.3284
S2	2.74	1.78	4.52	0.4167
S3	1.75	2.74	4.48	0.6116
S4	0.44	3.88	4.33	0.8961
E2	0.0	4.764	4.764	1.0

pressurised air on the crystal surface. All experiments were carried out at room temperature by Carlos Pina and Christine Putnis.

Partially replaced crystals were cleaved perpendicular to the replaced surfaces in order to study the texture of the replaced part as well as the advancement of the reaction and the replacement/substrate interface with the scanning electron microscope (JEOL 8600 MXA) at 20 kV. To obtain information about the kinetics of the replacement reaction rates were determined by measuring the thickness of the replaced part perpendicular to a  $\langle 100 \rangle$  surface on back scattered electron (BSE) images. Compositional profiles across the interface of the 25 minutes samples were measured on cleaved surfaces with the electron microprobe (JEOL 6300F SEM) at 15 kV and 10 nA. Cleaved surfaces were used because of mechanical brittleness of the (often porous) replaced part and the high solubility of the crystals which precludes polishing of the surfaces. Microanalysis of cleaved and porous surfaces presents several analytical problems: (a) non-flat surface influences the focus of the WD-spectrometers, (b) porosity and steps may lead to lower or higher totals depending on varying excited volumes and absorption paths (Knižek & Jurek, 1994) and (c) sample and standard orientation may deviate. As standards the unreacted cores (which are either KBr or KCl) were used. Therefore, at least for 2 of the 3 elements the orientation of standard and sample is identical. Analyses with totals of 95-102% were accepted if the cation to anion ratio was  $\sim 1 : 1$ . Remeasurement of the standard resulted in 100 wt. % with ideal stoichiometry and confirmed the reliability of the standardisation procedure.



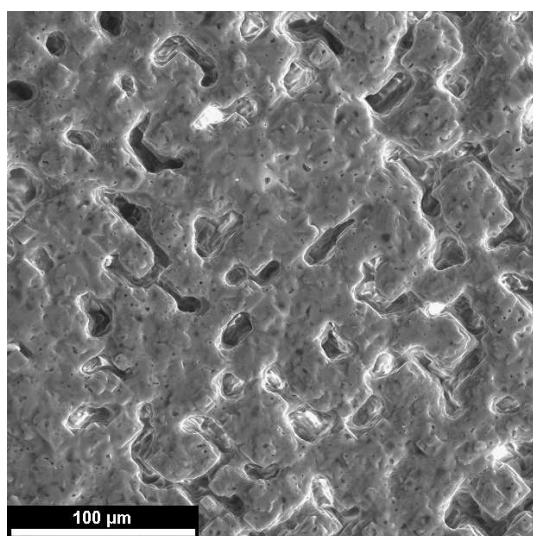


Figure 4.7: Texture of a replaced surface of a KBr crystal. The surface shows high porosity with a systematic arrangement of big pores and smaller pores in between. The edges of the pores are generally parallel to the faces of the crystal, i.e., parallel to  $\langle 100 \rangle$ . E1 on KBr substrate for 25 minutes

#### 4.7.2 Experimental results: Texture, composition and replacement rate

##### Replacements on KBr

KBr crystals which were placed in the Cl-rich solutions E1, S1, and S2, respectively, show a significant porosity in the replaced parts which can be observed on surfaces as well as in cross section (Fig. 4.7 and 4.8). Although the porosity cannot be easily determined from SE or BSE images, it is obvious that the porosity exceeds 10%. The porosity depends on the composition of the initial solution (Table 4.3) and increases with increasing chlorine content (from S2 to E1). At the surface major pores have often formed in regular distance to each other whereas smaller pores are distributed over the surface. The big pores commonly have edges oriented parallel to  $\langle 100 \rangle$ , i.e., parallel to idiomorphic faces of the used KBr crystals. Indeed, the crystallographic orientation of substrate has been found to be preserved in the replacement by single crystal XRD on a partly replaced KBr crystal (Putnis & Mezger, 2004). The crystal has been produced in an equivalent experimental setup as described here but with a solution enriched in  $^{40}\text{K}$ . By measuring the isotopic ratio in the initial crystal and the replacement these authors demonstrated that the mechanism of the replacement reaction is dissolution-precipitation/recrystallisation.

Fig. 4.8 shows the cross section of a partly replaced KBr crystal with high porosity. In the backscattered electron (BSE) image the compositional boundary between initial (bright) and replaced part (dark) can clearly be

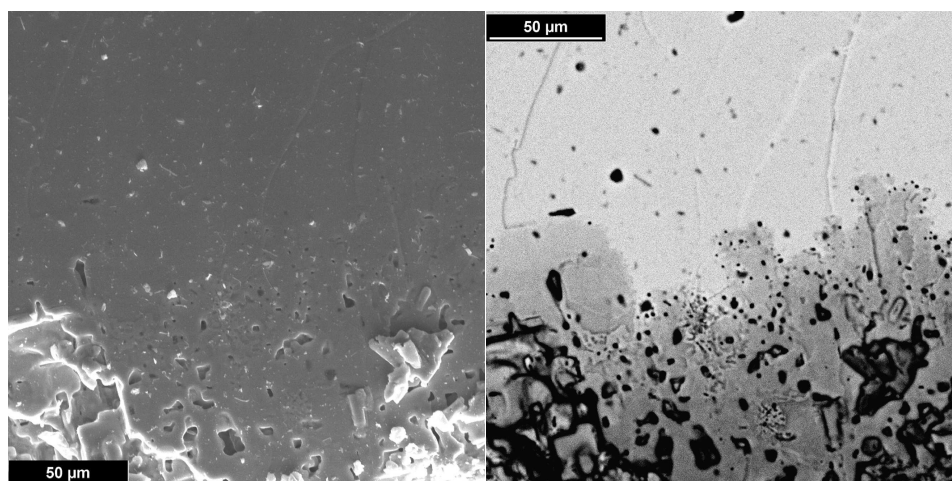


Figure 4.8: SE (*left*) and BSE (*right*) image of the interface between replacement and unreacted core. Note the wavylike run of the interface with clearly defined change in texture. To obtain the cross section the crystal has been cleaved after reaction which causes some damage on the highly porous replaced part. Note that pores and particles on the surface as well as the damaged areas at the lower corners give a similar signal in BSE image which makes it more complicate to determine the porosity. E1 on KBr substrate for 25 minutes

seen. The run of the boundary is wavelike and pores are usually found along this boundary but they are smaller than the pores on the surfaces. Replacements on KBr from the less Cl-rich solutions S3 and S4 show no porosity. Furthermore, the interface between the host and the replaced part is rather straight.

The compositions of the replacements,  $X_{Br}^{repl}$ , depend only partly on the initial solution composition (Fig. 4.9 and Table 4.4). For solutions E1 to S3 the compositions of the replacements (after 25 min.) lie within the same interval whereas the replacement due to solution S4 has a significant higher bromium content. The boundary between the substrate and the replacement range from sharp ( $< 5 \mu\text{m}$ ) for S4 to fairly extended ( $\sim 30 \mu\text{m}$ ) for E1. The width depends partly on the waviness of the interface which is more pronounced in replacements from Cl-rich solutions.  $X_{Br}^{repl}$  decreases from the interface to the rim/surface whereby the change in composition becomes smaller with increasing distance from the interface. S4 even leads

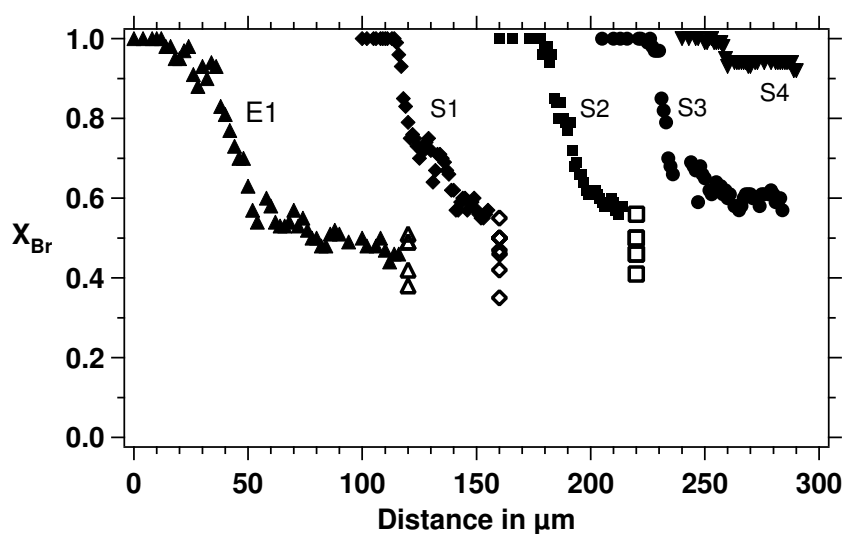


Figure 4.9: EMP line scans over unreacted core, interface, and replacement of partly replaced KBr crystals reacted with different solutions. The line scans have been arbitrarily shifted on the x-axis for better comparison of the replacement compositions and the shape of the profile. Open symbols represent repeated measurements on the outermost rims.

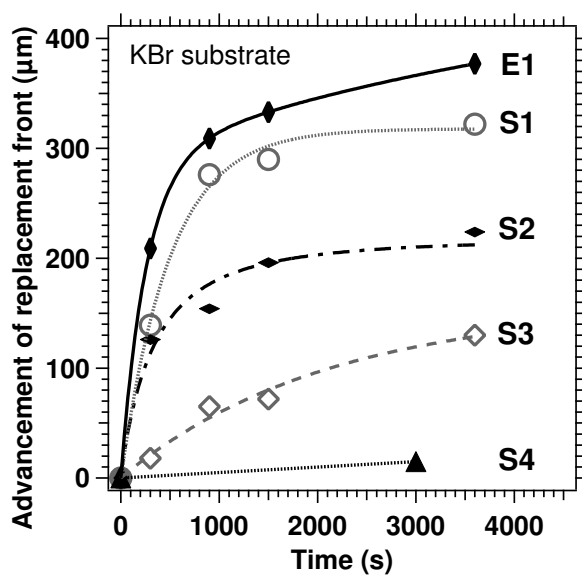


Figure 4.10: Advancement of replacement front for various solutions and KBr substrate. With increasing chlorine content of the solution the reaction is faster. Note the pronounced dip to slower reaction rates after  $\sim 600$  s. Lines between the points have been drawn to guide the eye.

to a replaced part with constant composition. For Cl-rich solutions the lowest compositions were analysed at the outermost rim of the replacements.

The replacement rate (Fig. 4.10) depends strongly on both the composition of the solution and on the duration of the experiment. Cl-rich solutions

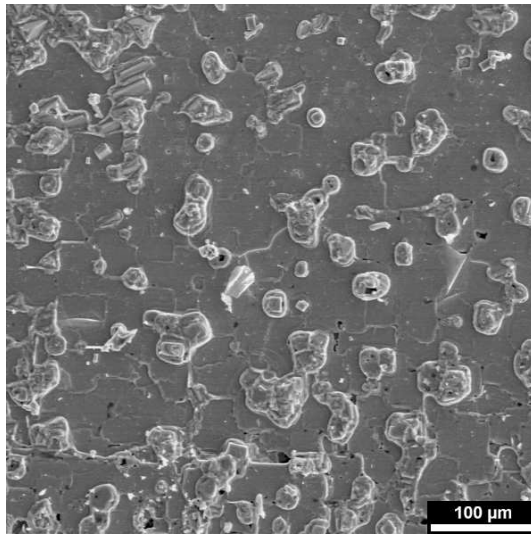


Figure 4.11: Texture of a replaced surface of a KCl crystal in solution with  $X_{Br,aq} = 1.0$ . The porosity of the replacement is very low. In addition, growth hillocks can be observed. E2 on KCl substrate for 25 minutes. (Micrograph from C. Putnis)

lead to a very high replacement rate of about  $30\text{-}40 \mu\text{m}/\text{min}$  at the start of the experiment. After about 10 minutes the rate starts to drop to about  $1 \mu\text{m}/\text{min}$  independent from the initial solution composition. For S3 the rate is about  $3 \mu\text{m}/\text{min}$  and decreases only little with time. In contrast, the rate for S4 is significantly smaller with about  $\sim 0.5 \mu\text{m}/\text{min}$ .

### Replacements on KCl

The replacement generated by solution E2 shows only some porosity along with growth hillocks on the replaced surface (Fig. 4.11). The hillocks are small new crystals that grew on top of the replaced surface obviously by 3-dimensional nucleation and growth. In cross section the interface between the substrate and the replacement appears quite straight but show also some waviness on a small scale.

For the solutions S1 to S4 the surface of the partly replaced crystals is similar to that of the initial crystal and no porosity has been observed at all. In addition, new crystal have been grown on the surface that sometimes show a crystallographic misorientation with respect to the substrate. The BSE cross section images show a layer of intermediate composition which has grown on the surface of the original crystal (Fig. 4.12). This newly formed layer is texturally not distinguishable from the substrate, it has a straight boundary with the substrate and looks like an overgrowth on the initial crystal. This decreasing  $X_{Br,aq}$  of the solution the interface becomes

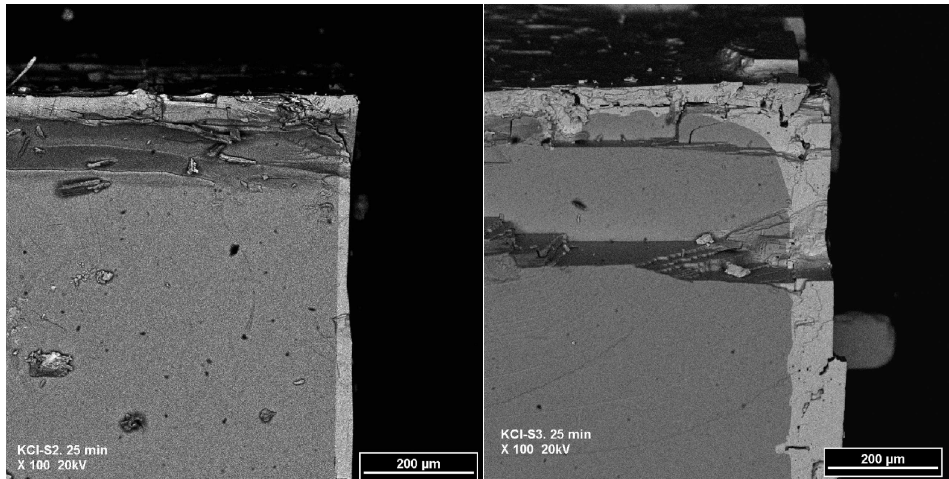


Figure 4.12: Two BSE images of the interface between the replacement and the unreacted core of KCl. The interface is straight and its thickness depends on the composition of the solution and the time of the experiments (cf. Fig. 4.14). Note that imperfections of the initial substrate like cracks have been completely covered by the replacement. (Micrographs from C. Putnis)

sharper. Initial imperfections of the cleaved surfaces, such as cracks and steps, are filled with new grown material.

The composition of the replacements correlates strongly with the initial composition of the solutions leading systematically to higher  $X_{Br}^{repl}$  with increasing Br-content of the solutions (Fig. 4.13). The boundary between substrate and replacement is extremely sharp ( $< 2 \mu\text{m}$ ) and cannot be clearly resolved by electron microprobe analyses. Only for solution E2 the boundary is more expanded ( $\sim 10 \mu\text{m}$ ). A slight increase in  $X_{Br}^{repl}$  was analysed towards the rim/surface of the new grown layer which becomes more pronounced the higher the Br-content of the initial solution.

Generally, the replacement rate of KCl (Fig. 4.14) is much lower than for KBr substrate and the advancement of the replacement front decreases with increasing Cl-content of the solution. Note that this behaviour is similar to the KBr substrate where the advancement was also smaller with increasing Br-content of the solution. At the beginning of the experiments the rate is as high as  $15 \mu\text{m}/\text{min}$  for solution E2 but significantly smaller for the other solutions. After 15 minutes the rate drops off to about  $0.5 \mu\text{m}/\text{min}$  (for S4 to  $1.5 \mu\text{m}$ )

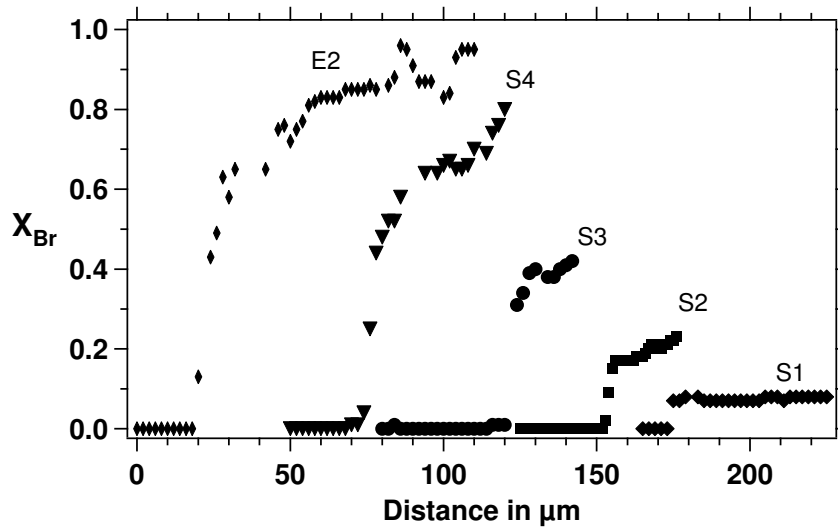


Figure 4.13: EMP line scans over unreacted core, interface, and replacement of a partly replaced KCl crystals. The line scans have been arbitrarily shifted on the x-axis for better comparison of the replacement compositions and the shape of the profile. Note the sharp increase in  $X_{Br}^{repl}$  within one or two analyses at the interface of core and replacement.

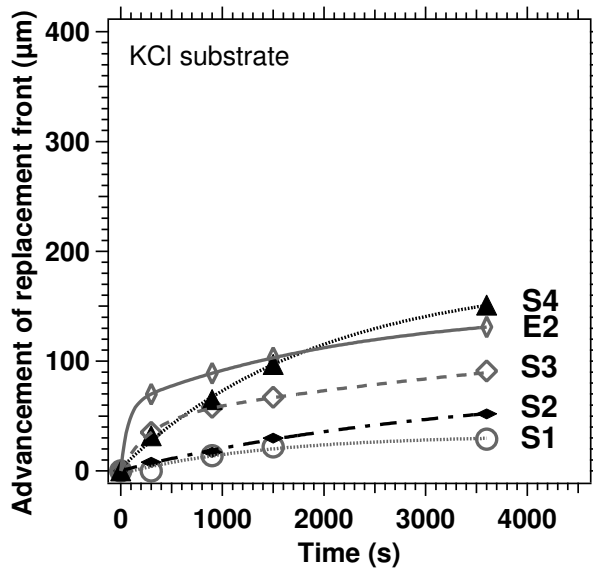


Figure 4.14: Advancement of replacement front for various solutions and KCl substrate. The rates are generally slower than in Fig. 4.10, but the dependence on the composition of the solution is comparable.

#### 4.7.3 Calculated results: reaction paths and volume changes

The composition of the starting solutions and the measured composition of replacements are needed to calculate the reaction pathways and volume

changes using the *solubility diagram* and the *solubility phase diagram* as described in detail in section 4.5. A number of useful parameters can be obtained from the calculation (Table 4.4) that will be explained separately. Then, the calculated values will be compared to the experimental findings. Finally, strengths and shortcomings of the theory in terms of the application to other systems will be discussed.

#### **Intersection with the solutus ( $P_1$ ) and first replacement composition**

Due to the dissolution of the substrate (either KBr or KCl) the undersaturated experimental starting solutions approach and finally intersect the solutus/solubility curve. The dissolution traces are shown in the solubility phase diagram (Fig. 4.15). The intersection is called  $P_1$  and is the starting point of the calculated dissolution-precipitation reaction because any solution is now saturated with respect to a certain solid composition. The composition of this first replacement is given by the tie-line of  $P_1$  to the solidus curve. Further dissolution of the substrate now shifts the composition of both solution and replacement towards the dissolved component, i.e., for KBr substrate to higher bromium content and for KCl to lower bromium content.

**Volume change at  $P_1$**  The difference in both solubility and molar volume between the initial crystal and the first replacement leads to a relative volume change,  $\Delta V_{d-p}^r$ . Although the absolute amount of replacement at  $P_1$  is negligible (strictly speaking it is infinite) the sign of  $\Delta V_{d-p}^r$  at this point is very important as it predicts the texture and kinetic of the replacement reaction. As it will be shown later by the comparison of experiment and theory a negative  $\Delta V_{d-p}^r$  can be texturally denoted as porosity in the replacement whereas a positive will cause an overgrowth on the initial crystal.

**End-point of the replacement reaction  $P_3$**  Two kinds of end-points have been considered in the theory part, an equilibrium or a non-equilibrium end-point, respectively. The equilibrium end-point would be achieved when the initial crystal has been completely replaced, is homogeneous, and stays in equilibrium with the solution. If there is still a part of the initial crystal present because the time of reaction was too short and/or the solution has been removed (as in the experiment) it can be described as a non-equilibrium end-point of the replacement reaction. The composition of the solution at this end-point  $P_3$  can be determined by the measured composition of the replacement. Assuming that the replacement is compositionally

homogeneous and that it was in equilibrium with the surrounding solution the composition of the solution can be calculated by a tie-line from solidus to solutus (cf. Fig. 4.4). However, compositional homogeneity of the replacement is seldom achieved as shown by EMP line scans (Fig. 4.9 and 4.13). Furthermore, it cannot be ascertained from the experiments whether any equilibrium relationship between solution and solid was reached at all since most experiments show the replacement reaction as 'caught in the act'. Nevertheless, to specify the possible range of solution compositions that may coexist with the replacements the lower and upper limit of EMP measurements has been considered for considerably zoned replacements (E1 and S1 to S3 on KBr).

**Mean and local volume change** Relative volume changes have been calculated for two different scenarios, the mean and the local  $\Delta V_{d-p}^r$ , respectively. As the dissolution-precipitation process started at  $P_1$  both the solution and the replacement have to change their composition continuously. Thus, to obtain a compositional homogeneous replacement in equilibrium with  $P_3$  the precipitated material has to recrystallise repeatedly. Averaging the volume changes of every reaction step gives the mean  $\Delta V_{d-p}^r$ . This mean value will also be obtained by calculating the whole reaction as one step with the substrate dissolving and the replacement in equilibrium with  $P_3$  precipitating. In contrast, the local  $\Delta V_{d-p}^r$  gives the volume change *at the replacement front* and does not involve any contributions from former reaction steps (cf Fig. 4.5). Therefore, the mean and local values are the two extremes which that bracket the possible  $\Delta V_{d-p}^r$  realised in the experiments and should at least provide the right sign.

**Mass of substrate dissolved** To continuously change the composition of replacement and solution during the reaction the substrate has to be dissolved. Therefore, the mass of the substrate,  $m_{subs}^d$ , needed to reach a certain  $X_{Br}^{repl} / X_{Br,aq}$  (from  $P_1$  to  $P_3$ ) is a parameter that couples the kinetics of the replacement reaction to the kinetics of the substrate dissolution. However,  $m_{subs}^d$  has only an effect on the replacement rate but not on the texture of the replacement.

### Comparison of experiment and theory

**Replacements on KBr** The calculated reaction paths for solutions E1, S1, and S2 predict a considerable negative  $\Delta V_{d-p}^{repl}$  i.e., a volume deficit, for the replacement. This finding is in excellent agreement with the high porosity



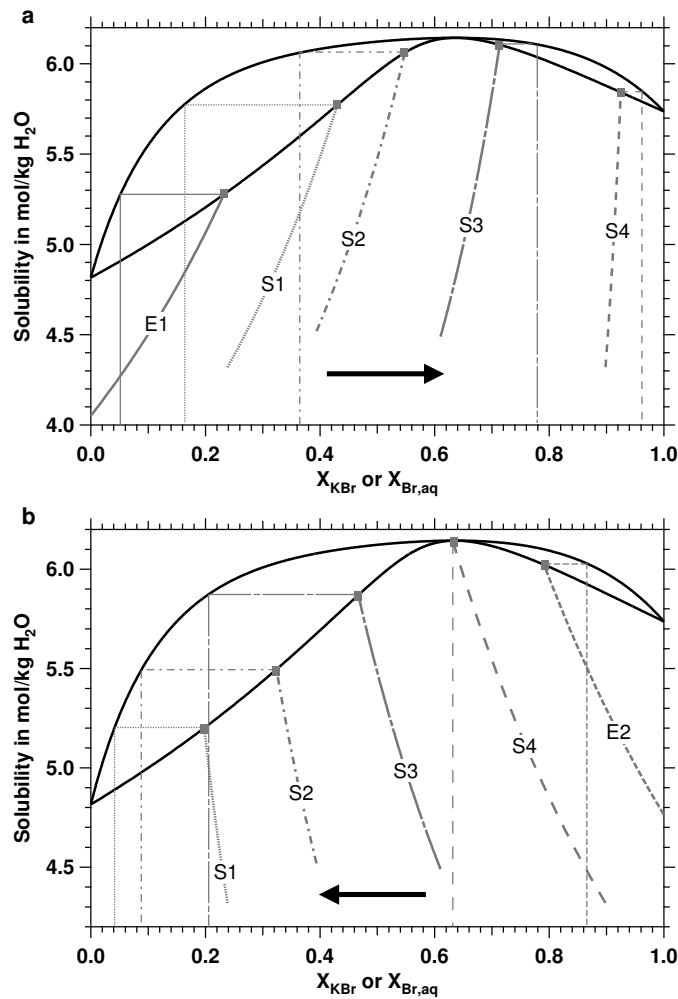


Figure 4.15: Evolution of solutions due to the dissolution of the substrate. The intersection with the solutus curve (point  $P_1$ ) is denoted by a square, respectively. The horizontal tie-line to this point gives the expected composition of the first replacement on the solidus curve (cf. Table 4.4). The compositions of both the replacements and the solutions evolve towards the dissolving component as denoted by an arrow, respectively **a** KBr substrate. Note the large difference between the expected composition for S2 and S3 because of the SS-AS relationships. **b** KCl substrate. Here the expected compositions for the first replacement due to S3 and S4 are very different whereas they are close for S1 and S2.

observed in the replacements from these solutions. Due to the high porosity the substrate stayed in contact with the solution and dissolved further after the replacement process has already started. Consequently, there is a large difference between the calculated composition of the first replacement and the measured one since the solution and replacement composi-

Table 4.4: Parameters of the replacement reaction calculated with the initial solution and the measured replacement compositions (*lower/upper* limit).  $X_{Br}^{repl}$  @P<sub>1</sub> is the calculated first solid composition precipitated on the substrate.  $\Delta V_{d-p}^r$  is the relative volume change for different point and scenarios on the dissolution-precipitation reaction. A negative sign on  $\Delta V_{d-p}^r$  denotes a volume deficit texturally noticeable as porosity and a positive  $\Delta V_{d-p}^r$  denotes a volume excess which causes an overgrowth.  $m_{subs}^d$  is the amount of substrate which has to be dissolved to reach the solution composition in equilibrium with measured replacement composition. Values which cannot be calculated for theoretical reasons are noted by *n.c.*

Solution	Substrate	$X_{Br}^{repl}$ meas.	$X_{Br}^{repl}$ calc.	$\Delta V_{d-p}^r$ in %			$m_{subs}^d$ calc. in g/100g H <sub>2</sub> O
				@P <sub>1</sub>	mean@P <sub>3</sub> <sup>EMP</sup>	local@P <sub>3</sub> <sup>EMP</sup>	
see Tab 4.3		P <sub>3</sub> <sup>EMP</sup>	@P <sub>1</sub>	@P <sub>1</sub>	mean@P <sub>3</sub> <sup>EMP</sup>	local@P <sub>3</sub> <sup>EMP</sup>	
E1	KBr	0.46/0.70	0.05	-44.5	-28.7/-15.1	-17.9/-2.1	43.2/89.8
S1	KBr	0.56/0.79	0.165	-42.0	-20.6/-7.2	-9.6/+0.1	29.3/93.3
S2	KBr	0.57/0.79	0.36	-26.7	-14.4/-3.9	-8.9/+0.1	11.7/58.6
S3	KBr	0.56/0.70	0.78	0.0	<i>n.c.</i>	<i>n.c.</i>	<i>n.c.</i>
S4	KBr	0.94	0.97	+0.3	~+0.3	~+0.3	21.8
S1	KCl	0.07	0.04	+2.2	~ +2.2	~ +2.2	1.1
S2	KCl	0.17	0.085	+4.8	<i>n.c.</i>	<i>n.c.</i>	<i>n.c.</i>
S3	KCl	0.4	0.205	+11.1	<i>n.c.</i>	<i>n.c.</i>	<i>n.c.</i>
S4	KCl	0.67	0.63	+11.4	<i>n.c.</i>	<i>n.c.</i>	<i>n.c.</i>
E2	KCl	0.85	0.87	-6.1	-5.4	-4.7	1.2

tion evolves towards higher  $X_{Br,aq}$  and  $X_{Br}^{repl}$ , respectively (from  $P_1$  to  $P_3^{EMP}$ ). The calculated porosity (the negative  $\Delta V_{d-p}^r$ ) is decreasing with increasing  $X_{Br}^{repl}$ . Note that for the highest measured  $X_{Br}^{repl} = 0.79$  the local  $\Delta V_{d-p}^r$  just changed the sign to positive which may vastly change the kinetic of the reaction. This result is in agreement with the observation that the pores become smaller from the surface to the interface and the compositional profile on these replacements. Moreover, the replacement rate can be qualitatively understood by the calculated parameters. The porosity calculated for the first replacement correlates positively with the initial replacement rate, i.e., the higher the porosity the more surface of the substrate is in contact with the solution and the higher the rate. Then, the porosity decreases with time and simultaneously the amount of substrate that has to be dissolved to change the solution composition,  $m_{subs}^d$ , increases (cf. also Fig. 4.5 and 4.6). Both effects lead to a significant decrease of the replacement rate.

For solution S3 most parameters cannot be calculated because the measured  $X_{Br}^{repl}$  is lower than the calculated  $X_{Br}^{repl}$  at  $P_1$ . This finding is not consistent with the theory because from  $P_1$  the compositions can only evolve

to higher not the lower  $X_{Br}^{repl}$  and the initial solution is the only source of Br. Furthermore, the measured composition of the replacement and the initial replacement rate rather suggest a volume deficit reaction as for the previously described cases. However, no porosity has been observed in the replacement in agreement with the calculated  $\Delta V_{d-p}^r$  at  $P_1$ . The reason for this ambiguous behaviour remains unclear.

For S4 the calculated  $\Delta V_{d-p}^r$  is positive, i.e. the replacement reaction has a volume excess and no porosity will be formed which is exactly what has been observed experimentally. The surface of the substrate is covered by an overgrowth in the first reaction step and the initial crystal is armoured against the solution. Therefore, the measured composition of the replacement is in agreement with calculated composition at  $P_1$ . The most obvious difference of the volume excess reaction can be seen on the replacement rate which is almost zero because after the formation of the overgrowth the replacement reaction is almost stopped. In addition to the textural reaction hindrance, a large amount of initial crystal,  $m_{subs}^d$ , has to be dissolved to effectively change the solution composition.

**Replacements on KCl** A positive  $\Delta V_{d-p}^r$  has been calculated for the solutions S1 to S4 which suggests an overgrowth formation for the replacements. Therefore, it is predicted by the theory that the composition of the replacement is close to the composition of the first precipitated composition because in this reaction step the complete surface of the initial crystal will be covered by the replacement. For solutions S1 and S4 the calculated  $X_{Br}^{repl}$  are in very good agreement with measured values whereas for S2 and S3 the measured compositions are somewhat too high in  $X_{Br}^{repl}$ . Note that the solution and replacement composition should evolve to more Cl-rich compositions after reaching the solutus at  $P_1$ . Compositions of the replacements with a  $X_{Br}^{repl}$  higher than the calculated value are theoretically not possible since there is no other source of Br except the solution. Thus, there might be a kinetic effect that shifts the compositions to the measured value which cannot be specified further either from theory or experiments. Due to the overgrowth formation the interface between replacement and substrate is expected to be sharp and the replacement rate must be lower than for the volume deficit reaction. Both is clearly observed experimentally (Fig. 4.13 and 4.14). The extent of volume excess for solutions S1 to S4 increases with increasing  $X_{Br,aq}$  of the solution. Therefore, the thickness of the replacement layer is also expected to increase. This is reflected in the systematically different replacement rates which after a certain time run more

or less parallel. As a consequence the replacement reaction is effectively stopped when the volume excess material has precipitated on the substrate covering and armouring it to the solution.

For solution E2 the observation of small pores in replacements and a more extended interface is in good agreement with the calculated volume deficit. In addition, the replacement rate decreases with time because the porosity decreases as explained for the other volume deficit reactions. Comparing the replacement rates of all volume deficit reactions (E1, S1 to S3/S4? on KBr and E2 on KCl) then the positive correlation between porosity generated and the rate becomes obvious.

## 4.8 Conclusion and broader impact

In this chapter, a model has been presented for quantitative analysis of volume change in a coupled dissolution-precipitation (replacement) reaction with special emphasis on the SS-AS relationships. The basis for the quantitative analysis of reaction paths is the combined use of solubility and SS-AS equilibrium data consistently. With the KBr – KCl – H<sub>2</sub>O system as an example it was theoretically shown that the volume change due to a replacement reaction is not only dependent on the difference in molar volume of the initial and replacing phase but is also influenced significantly by the difference in solubility of the involved phases. Furthermore, experiments in the same systems have been performed and the comparison with results calculated by the theory lead to at least a qualitatively sound interpretation of the replacement reaction. Especially the prediction of the sign of the volume change (deficit/excess) that largely controls the replacement texture and kinetics can be regarded as successfully.

As emphasised by Putnis (2002), a predominant number of natural and experimental replacement reactions proceed via a moving front suggesting a dissolution-reprecipitation mechanism. Porosity in the replacing phase has been often observed and, therefore, the reaction mechanism and texture are in general comparable to those modelled for the KBr – KCl – H<sub>2</sub>O system. Since the solubility of minerals is usually unknown for replacement reactions in geological environments, volume changes due to differences in solubility are seldom discussed. However, the microporosity observed in various natural and experimental samples can be qualitatively understood by the assumption of solubility differences (e.g., the leucite to analcime transformation (Putnis *et al.*, 1994) and the chloro-, hydroxy-, fluoroapatite system (Yanagisawa *et al.*, 1999; Rendón-Angeles *et al.*, 2000a,b,c)).

Furthermore, difference in solubility due to strain could also provide an explanation for the microporosity observed in the reaction such as cryptoperthite to coarse patchy perthites (Walker *et al.*, 1995), where there is no overall molar volume change. Furthermore, the model presented here is qualitatively in line with the metasomatic replacement of Y-REE enriched apatite by 'depleted' apatite plus newly formed (Y+REE)-phosphate minerals (Harlov *et al.*, 2002; Harlov & Förster, 2003; Harlov *et al.*, 2003) and the recrystallisation of pristine zircon to porous and trace element depleted zircon plus the nucleation of Y-REE-Th phases (Tomaschek *et al.*, 2003). The latter examples show that differences in minor and trace elements have a considerable influence on the solubility and, thus, on the SS-AS relationships and the textural evolution under metasomatic conditions.

In conclusion, the theoretical description of a replacement reaction as dissolution-precipitation reaction in SS-AS systems has proven itself to be a valuable tool that helps to understand volume change in general and porosity generation in particular.



# Acknowledgement / Danksagung

I would like to thank Andrew Putnis as my supervisor for his incitement to work on these interesting mineralogical topics, oscillatory zoning and replacement reactions, for his support and supervision.


Udo Becker has motivated me to learn, use and see into molecular simulation and Monte Carlo techniques. Thank you for that and the time we spent with discussions.

Josema Astilleros, Thorsten Geisler-Wierwille, Ute Golla-Schindler, Carlos Pina, Christine Putnis, and Viktor Vinograd are thanked for various discussions regarding, e.g., solid solution-aqueous solution systems, electron microscopy, modelling and thermodynamics...

Bjørn Jamtveit (Oslo) has kindly provided the oscillatory zoned garnet samples, Håkon Austrheim and Alexander Kühn provided the granulite/eclogite samples from Holsnøy. I am particularly grateful to Håkon and Mats Lund that they gave me the opportunity to accompany them on field work on Holsnøy. You have been outstanding hosts.

On his visit in Münster, Arkady Glikin shared with us the idea of *deficit* and *excess* replacement reactions and the use of solubility diagrams. Thank you for stimulating discussions.

Ein weiterer Dank geht an die Mitarbeiter der Präparationswerkstatt, Paul Löbke und Ulla Heitmann, für die hervorragende Erstellung der Dünnschliffe und die Hilfen bei der TEM-Probenpräparation. Ferner danke ich allen Mitarbeiterinnen und Mitarbeitern des Institutes für Mineralogie, die mit Rat und Tat Anteil am Gelingen dieser Arbeit hatten.

Vielen Dank an *den* Chor: Piano 22/30 . Und zwar nicht nur fürs Singen! Meinen Eltern danke ich von Herzen für all ihre Unterstützung, ohne die das Studium der Mineralogie und damit die Promotion nicht möglich gewesen wäre. Vor allem aber möchte ich mich aber bei meiner Frau Steffi sowie meinen Kindern Jakob und Silas bedanken. Danke für Eure Liebe und Geborgenheit, für Eure Geduld und Eurer Verständnis, und für die lachenden Augen, wenn ich nach Hause komme.





# Bibliography

- Ahrens, T.J. & Schubert, G. (1975): Rapid formation of eclogite in a slightly wet mantle. *Earth Planet Sci Lett*, **27**, 90–94.
- Aines, R.D. & Rossman, G.R. (1984): Water content of mantle garnets. *Geology*, **12**, 720–723.
- Akizuki, M. (1984): Origin of optical variations in grossular–andradite garnet. *Am Mineral*, **69**, 328–338.
- Akizuki, M., Nakai, H. & Suzuki, T. (1984): Origin of iridescence in grandite garnet. *Am Mineral*, **69**, 896–901.
- Allen, F.M. & Buseck, P.R. (1988): XRD, FTIR, and TEM studies of optically anisotropic grossular garnets. *Am Mineral*, **73**, 568–584.
- Armbruster, T. & Geiger, C.A. (1993): Andradite crystal chemistry, dynamic X-site disorder and structural strain in silicate garnets. *Eur J Mineral*, **5**, 59–71.
- Austrheim, H. (1987): Eclogitisation of lower crustal granulites by fluid migration through shear zones. *Earth Planet Sci Lett*, **81**, 221–232.
- Austrheim, H. (1998): Influence of fluid and deformation on metamorphism of the deep crust and consequences for the geodynamics of collision zones. *in: "When continents collide: Geodynamics and geochemistry of ultrahigh-pressure rocks"*, B.R. Hacker, J.G. Liou, eds. Kluwer Academic Publishers.
- Austrheim, H., Erambert, M. & Boundy, T. (1996): Garnet recording deep crustal earthquakes. *Earth Planet Sci Lett*, **139**, 223–238.
- Austrheim, H. & Griffin, W.L. (1985): Shear deformation and eclogite formation within granulite-facies anorthosites of the Bergen arcs, Western Norway. *Chem Geol*, **50**, 267–281.

- Austrheim, H., Erambert, M. & Engvik, A.K. (1997): Processing of crust in the root of the Caledonian continental collision zone: the role of eclogitization. *Tectonophysics*, **273**, 129–153.
- Azimov, P.Y. & Shtukenberg, A.G. (2000): Simulation of phase diagrams for water-salt systems with solid solutions. *Russian Journal of Inorganic Chemistry*, **45(8)**, 1302–1309.
- Badar, M.A. & Akizuki, M. (1997): Iridescent andradite garnet from the Sierra Madre Mountains, Sonora, Mexico. *N Jb Miner Mh*, **12**, 529–539.
- Bass, J.D. (1986): Elasticity of uvarovite and andradite garnets. *J Geophys Res*, **91**, 7505–7516.
- Bass, J.D. (1989): Elasticity of grossular and spessartine garnets by Brillouin spectroscopy. *J Geophys Res*, **94**, 7621–7628.
- Baxter, E. & DePaolo, D. (2000): Field measurements of slow metamorphic reaction rates at temperatures of 500 to 600°C. *Science*, **288**, 1411–1414.
- Becker, U., Fernández-González, A., Prieto, M., Harrison, R. & Putnis, A. (2000): Direct calculation of thermodynamic properties of the barite/celestite system from molecular principles. *Phys Chem Mineral*, **27**, 291–300.
- Bjørnerud, M.G., Austrheim, H. & Lund, M.G. (2002): Processes leading to eclogitization (densification) of subducted and tectonically buried crust. *J Geophys Res Sol Ea*, **107(B10)**, 2252.
- Blanc, Y. & Maisonneuve, J. (1973): Sur la birefringence des grenats calcaïques. *Bull Soc Fr Mineral Cristallogr*, **96**, 320–321.
- Blum, J.R. (1843): “Die Pseudomorphosen des Mineralreichs”. E. Schweizerbartsche Verlagshandlung.
- Bosenick, A., Dove, M.T. & Geiger, C.A. (2000): Simulation studies on the pyrope–grossular garnet solid solution. *Phys Chem Mineral*, **27**, 398–418.
- Bosenick, A., Dove, M.T., Myers, E.R., Palin, E.J., Saint-Diaz, C.I., Guiton, B.S., Warren, M.C. & Craig, M.S. (2001): Computational methods for the study of energies of cation distributions: applications to cation-ordering phase transitions and solid solutions. *Mineral Mag*, **65**, 193–219.

- Boundy, T.M., Fountain, D.M. & Austrheim, H. (1992): Structural development and petrofabrics of eclogite facies shear zones, Bergen Arcs, western Norway: implications for deep crustal deformational processes. *J Metamorph Geol*, **10**, 127–146.
- Boundy, T.M., Mezger, K. & Essene, E.J. (1997): Temporal and tectonic evolution of the granulite–eclogite association from the Bergen arcs, western Norway. *Lithos*, **39**, 159–178.
- Boundy, T.M., Donohue, C.L., Essene, E.J., Mezger, K. & Austrheim, H. (2002): Discovery of eclogite facies carbonate rocks from the Lindås Nappe, Caledonides, western Norway. *J Metamorph Geol*, **20**, 649–667.
- Bryxina, N.A., Halden, N.M. & Ripinen, O.I. (2002): Oscillatory zoning in an agate from Kazakhstan: Autocorrelation function and fractal statistics of trace element distributions. *Math Geol*, **34**, 915–927.
- Bush, T.S., Gale, J.D., Catlow, C.R.A. & Battle, P.D. (1994): Self-consistent interatomic potentials for the simulation of binary and ternary oxides. *J Mat Chem*, **4**, 831–837.
- Cardew, P.T. & Davey, R.J. (1985): The kinetics of solvent-mediated phase transformations. *Proceedings Royal Society of London*, **A(398)**, 415–428.
- Carmichael, D.M. (1986): Induced stress and secondary mass transfer: thermodynamic basis for the tendency towards constant-volume constrain in diffusion metasomatism. *in* “Chemical transport in metasomatic processes”, H.C. Helgeson, ed. *Nato ASI Series C*, **218**, 237–264.
- Carpenter, M.A. (1981): Omphacite microstructures as time -temperature indicators of blueschist and eclogite-facies metamorphism. *Contrib Mineral Petrol*, **78**, 441–451
- Carpenter, M.A. & Putnis, A. (1985): Cation order and disorder during crystal growth: some implications for natural mineral assemblages. *in* “Metamorphic reactions”, A.B. Thompson, D.C. Rubie, eds. *Advances in physical geochemistry*, **vol 4**, Springer Verlag.
- Cartwright, I. (1997): Permeability generation and resetting of tracers during metamorphic flow: implications for advection–dispersion models. *Contrib Mineral Petrol*, **129**, 198–208.
- Catlow, C.R.A. (1988): Computer modelling in silicates. *in*: “Physical properties and thermodynamic behaviour of minerals”, E.K.H. Salje, ed. *NATO ASI Series C*, **225**, 619–638.

- Chakraborty, S. & Ganguly, J. (1991): Compositional zoning and cation diffusion in garnets. *in*: "Diffusion, atomic ordering, and mass transport", J. Ganguly, ed. *Advances in physical geochemistry*, vol. 8, Springer Verlag.
- Chase, A.B. & Lefever, R.A. (1960): Birefringence of synthetic garnets. *Am Mineral*, 45, 1126–1129.
- Cole, D.R. (2000): Isotopic exchange in mineral–fluid systems IV. The crystal chemical controls on oxygen isotope exchange rates in carbonate–H<sub>2</sub>O and layer silicate–H<sub>2</sub>O systems. *Geochim Cosmochim Acta*, 64, 921–933.
- Conrad, P.G., Chang-Zheng, Z., Ho-Kwang, M. & Russell, J.H. (1999): The high-pressure, single-crystal elasticity of pyrope, grossular, and andradite. *Am Mineral*, 84, 374–383.
- Cortini, M. & Anastasio, D. (2001): Chemical banding in volcanic minerals: a statistical phenomenological approach. *Eur J Mineral*, 13, 571–575.
- Dejewska, B. (1999): The characteristics of the mixed crystals of the KBr – KCl – H<sub>2</sub>O system at 298 K. *Cryst Res Technol*, 34, 975–979.
- Dejewska, B. & Szymański, T. (1998): The base of the computation of quantitative changes running in technological processes in the multicomponent systems with mixed crystals. *Cryst Res Technol*, 33, 757–765.
- Dove, M.T. (1989): On the computer modeling of diopside: towards a transferable potential for silicate minerals. *Am Mineral*, 74, 774–777.
- Dove, M.T. (2001): Computer simulations of solid solutions. *in* "Solid solutions in silicate and oxide systems of geological importance", C.A. Geiger, ed. *EMU Notes in Mineralogy*, vol 3, Eötvös University Press, Budapest.
- Durham, G.S., Rock, E.J. & Frayn, S.F. (1953): Solid solution of the alkali halides. I. The systems KBr – KCl – H<sub>2</sub>O, RbBr – RbCl – H<sub>2</sub>O, RbBr – KBr – H<sub>2</sub>O at 25°. *J Amer Chem Soc*, 75, 5793–5794.
- Engi, M. & Wersin, P. (1987): Derivation and application of a solution model for calcic garnet. *Schweiz Mineral Petrogr Mitt*, 67, 53–73.
- Engvik, A.K., Austrheim, H. & Erambert, M. (2001): Interaction between fluid flow, fracturing and mineral growth during eclogitization, an example from the Sunnfjord area, Western Gneiss Zone, Norway. *Lithos*, 57, 111–141.

- Erambert, M. & Austrheim, H. (1993): The effect of fluid and deformation on zoning and inclusion patterns in poly-metamorphic garnets. *Contrib Mineral Petrol*, **115**, 204–214.
- Feder, J. (1988): "Fractals". Plenum Press, New York.
- Ferry, J.M. (2000): Patterns of mineral occurrence in metamorphic rocks. *Am Mineral*, **85**, 1573–1588.
- Gale, J. (1998): GULP (General Utility Lattice Program), Imperial College/Royal Institution of Great Britain.
- Gali, S. (1983): Grandite garnet structures in connection with the growth mechanism. *Zeitschr Kristallogr*, **163**, 43–52.
- Geiger, C.A. (1999): Thermodynamics of  $(\text{Fe}^{2+}, \text{Mn}^{2+}, \text{Mg}, \text{Ca})_3\text{Al}_2\text{Si}_3\text{O}_{12}$  garnet: a review and analysis. *Mineral Petrol*, **66**, 271–299.
- Geiger, C.A. & Armbruster, T. (1997):  $\text{Mn}_3\text{Al}_2\text{Si}_3\text{O}_{12}$  spessartine and  $\text{Ca}_3\text{Al}_2\text{Si}_3\text{O}_{12}$  grossular garnet: structural dynamic and thermodynamic properties. *Am Mineral*, **82**, 740–747.
- Geiger, C.A., Newton, R.C. & Kleppa, O.J. (1987): Enthalpy of mixing of synthetic almandine–grossular and almandine–pyrope garnets from high-temperature solution calorimetry. *Geochim Cosmochim Acta*, **51**, 1755–1763.
- Gillet, P., Fiquet, G., Malezieux, J.M. & Geiger, C.A. (1992): High-pressure and high-temperature Raman spectroscopy of end-member garnets – pyrope, grossular and andradite. *Eur J Mineral*, **4**, 651–664.
- Ginibre, C., Kronz, A. & Wörner, G. (2002): High-resolution quantitative imaging of plagioclase composition using accumulated backscattered electron images: new constraints on oscillatory zoning. *Contrib Mineral Petrol*, **142**, 436–448.
- Glikin, A.E. (1995): To a theory of isomorphic mixed-crystal formation. *Zapiski VMO*, **5**, 125–134 (in Russ.).
- Glikin, A.E. & Sinai, M.Yu. (1991): Morphological-genetic classification of products of crystal replacements. *Zapiski VMO*, **1**, 3–17 (in Russ.).
- Glikin, A.E. & Sinai, M.Yu. (1993): Experimental investigation of monocystal pseudomorph formation. *Zapiski VMO*, **6**, 742–748 (in Russ.).

- Glikin, A.E., Kovalev, S.I., Rudneva, E.B., Kryuchkova, L. Yu. & Voloshin, A.E. (2003): Phenomena and mechanisms of mixed crystal formation in solutions I. General concept on the example of the system  $\text{KHC}_8\text{H}_4\text{O}_4 - \text{RbHC}_8\text{H}_4\text{O}_4 - \text{H}_2\text{O}$ . *J Crystal Growth*, **255**, 150–162.
- Glynn, P.D. & Reardon, E.J. (1990): Solid-solution aqueous-solution equilibria: thermodynamic theory and representation. *Amer Journ Science*, **290**, 164–201.
- Glynn, P.D., Reardon, E.J., Plummer, L.N. & Busenberg, E. (1990): Reaction paths and equilibrium end-points in solid-solution aqueous-solution systems. *Geochim Cosmochim Acta*, **54**, 267–282.
- Guggenheim, E.A. (1937): Theoretical basis for Raoult's law. *Transactions of the Faraday Society*, **33**, 151–159.
- Haasen, P. (1994): "Physikalische Metallkunde". Springer Verlag.
- Hacker, B.R. (1996): Eclogite formation and the rheology, buoyancy, seismicity, and  $\text{H}_2\text{O}$  content of oceanic crust. *in: "Subduction Top to Bottom"*, G.E. Bebout, D.W. Scholl, S.H. Kirby, J.P. Platt, eds. Geophys. Monogr. Ser., vol. 96, AGU, Washington, D.C., 337–346.
- Halden, N.M. & Hawthorne, F.C. (1993): The fractal geometry of oscillatory zoning in crystals: application to zircon. *Am Mineral*, **78**, 1113–1116.
- Halden, N.M. (1996): Determination of Lyapounov exponents to characterize the oscillatory distribution of trace elements in minerals. *Can Mineral*, **34**, 1127–1135.
- Harlov, D.E., Förster, H.-J. & Nijland, T.G. (2002): Fluid-induced nucleation of (Y + REE)-phosphate minerals within apatite: Nature and experiment. Part I. Chlorapatite. *Am Mineral*, **87**, 245–261.
- Harlov, D.E. & Förster, H.-J. (2003): Fluid-induced nucleation of (Y + REE)-phosphate minerals within apatite: Nature and experiment. Part II. Fluorapatite. *Am Mineral*, **88**, 1209–1229.
- Harlov, D.E., Förster, H.-J. & Schmidt, C. (2003): High p-T experimental metasomatism of a fluorapatite with significant britholite and flourellestadite components: implications for LREE mobility during granulite-facies metamorphism. *Mineral Mag*, **67**, 61–72.

- Haselton, H.T. Jr. & Westrum, E.R. Jr. (1980): Low-temperature heat capacities of synthetic pyrope, grossular, and pyrope<sub>60</sub>grossular<sub>40</sub>. *Geochim Cosmochim Acta*, **44**, 701–709.
- Hatch, D.M. & Griffen, D.T. (1989): Phase transition in grandite garnets. *Am Mineral*, **74**, 151–159.
- Hazen, R.M. & Finger, L. (1989): High-pressure crystal chemistry of andradite and pyrope: revised procedures for high-pressure diffraction experiments. *Am Mineral*, **74**, 352–359.
- Herz, R. (1892): Ueber die Zonarstruktur der Plagioklase. *Tschermaks Mineral Petrogr Mitt*, **13**, 343–348.
- Heuss-Aßpichler, S. & Fehr, K.T. (1997): Intercrystalline exchange of Al and Fe<sup>3+</sup> between grossular–andradite and clinozoisite–epidote solid solutions. *N Jb Miner Abh*, **172**, 69–100.
- Hirai, H. & Nakazawa, H. (1986): Grandite garnet from Nevada: confirmation of origin of iridescence by electron microscopy and interpretation of a moiré-like structure. *Am Mineral*, **71**, 123–126.
- Holten, T., Jamtveit, B., Meakin, P., Cortini, M., Blundy, J. & Austrheim H (1997): Statistical characteristics and origin of oscillatory zoning in crystals. *Am Mineral*, **82**, 596–606.
- Holten, T., Jamtveit, B. & Meakin, P. (1998): Self-affine fractal geometry of agate. *Eur J Mineral*, **10**, 149–153.
- Holten, T., Jamtveit, B. & Meakin, P. (2000): Noise and oscillatory zoning of minerals. *Geochim Cosmochim Acta*, **64**, 1893–1904.
- Hori, S. (1990): Seismic waves guided by untransformed oceanic crust subducting into the mantle: The case of the Kanto district, central Japan. *Tectonophysics*, **176**, 355–376.
- Hoskin, P.W.O. (2000): Patterns of chaos: Fractal statistics and the oscillatory chemistry of zircon. *Geochim Cosmochim Acta*, **64**, 1905–1923.
- Huckenholz, H.G. & Fehr, K.T. (1982): Stability relationships of grossular+quartz+wollastonite+anorthite. II. The effect of grandite–hydrograndite solid solution. *N Jb Miner Abh*, **145**, 1–33.

- Huckenholz, H.G., Lindhuber, W., & Springer, J. (1974): The join  $\text{CaSiO}_3 - \text{Al}_2\text{O}_3 - \text{Fe}_2\text{O}_3$  of the  $\text{CaO} - \text{Al}_2\text{O}_3 - \text{Fe}_2\text{O}_3 - \text{SiO}_2$  quaternary system and its bearing on the formation of the granditic garnets and fassaitic pyroxenes. *N Jb Miner Abh*, **121**, 160–207.
- Inden, G. & Pitsch, W. (1991): Atomic ordering. *in*: "Phase transformation in materials", R.W. Cahn, P. Haasen, E.J. Kramer, eds., Materials science and technology, **Vol. 5**, VCH, Weinheim, 499–549.
- Ingerson, E. & Barksdale, J.D. (1943): Irisdescent garnet from the Adelaide mining district, Nevada. *Am Mineral*, **28**, 303–312.
- Isaak, D.G., Anderson, O.L. & Oda, H. (1992): High-temperature thermal expansion and elasticity of calcium garnets. *Phys Chem Mineral*, **19**, 106–120.
- Ivanova, T.I., Shtukenberg, A.G., Punin, Y.O., Frank-Kamenetskaya, O.V. & Sokolov, P.B. (1998): On the complex zonality in grandite garnets and implications. *Mineral Mag*, **62**, 857–868.
- Jamtveit, B. (1991): Oscillatory zonation patterns in hydrothermal grossular–andradite garnet: Nonlinear dynamics in regions of immiscibility. *Am Mineral*, **76**, 1319–1327.
- Jamtveit, B. & Anderson, T.B. (1992): Morphological instabilities during rapid growth of metamorphic garnets. *Phys Chem Minerals*, **19**, 176–184.
- Jamtveit, B. & Hervig, R.L. (1994): Constraints on the transport and kinetics in hydrothermal systems from zoned garnet crystals. *Science*, **263**, 505–508.
- Jamtveit, B., Bucher-Nurminen, K. & Austrheim, H. (1990): Fluid controlled eclogitization of granulites in deep crustal shear zones, Bergen arcs, western Norway. *Contrib Mineral Petrol*, **104**, 184–193.
- Jamtveit, B., Bucher-Nurminen, K. & Stijfhoorn, D.E. (1992): Contact metamorphism of layered shale-carbonate sequences in the Oslo rift: I. Buffering, infiltration, and the mechanisms of mass transport. *J Petrol*, **33**, 377–422.
- Jamtveit, B., Wogelius, R. & Fraser, D.G. (1993): Zonation patterns of skarn garnets: stratigraphic records of hydrothermal systems. *Geology*, **21**, 113–116.



- Jamtveit, B., Ragnarsdottir, K.V. & Wood, B.J. (1995): On the origin of zones grossular–andradite garnets in hydrothermal systems. *Eur J Mineral*, **7**, 1399–1410.
- Jamtveit, B. & Meakin, P. (Eds.) (1999): “Growth, dissolution and pattern formation in geosystems”. Kluwer Academic Publishers.
- Jamtveit, B., Austrheim, H. & Malthes-Sørensen, A. (2000): Accelerated hydration of the Earth’s deep crust induced by stress perturbations. *Nature*, **408**, 75–78.
- John, T. & Schenk, V. (2003): Partial eclogitisation of gabbroic rocks in a late Precambrian subduction zone (Zambia): prograde metamorphism triggered by fluid infiltration. *Contrib Mineral Petrol*, **146**, 174–191.
- Kingma, K.J. & Downs, J.W. (1989): Crystal-structure analysis of a birefringent andradite. *Am Mineral*, **74**, 1307–1316.
- Kirby, S.H. , Engdahl, E.R. & Denlinger, R. (1996): Intermediate-depth intraslab earthquakes and arc volcanism as physical expressions of crustal and uppermost mantle metamorphism in subducting slabs. *in: Subduction Top to Bottom*, G.E. Bebout, D.W. Scholl, S.H. Kirby, J.P. Platt, eds. Geophys. Monogr. Ser., vol. 96, AGU, Washington, D.C., 195–214.
- Kitamura, K. & Komatsu, H. (1978): Optical anisotropy associated with growth strain of yttrium garnet,  $Y_3(Al, Fe)_5O_{12}$ . *Krist Tech*, **13**, 811–816.
- Klein, U., Sharp, T.G. & Schumacher, J.C. (1997): Analytical electron microscopy of nanometer-scale hornblende lamellae: low-temperature exsolution in cummingtonite. *Am Mineral*, **82**, 1079–1090.
- Knižek, K. & Jurek, K. (1994): Correction procedure for the electron microprobe analysis of porous materials. *Microchim Acta*, **117**, 87–93.
- Kolesnik, Y.N., Nogteva, V.V., Arkhipenko, D.K., Orekhov, B.A. & Paukov, I.Y. (1979): Thermodynamics of pyrope–grossular solid solutions and the specific heat of grossular at 13–300 K. *Geochemistry*, **79**, 57–64.
- Korzhinskii, D.S. (1970): “Theory of Metasomatic zoning”. Clarendon Press, Oxford.
- Krabbendam, M., Wain, A. & Andersen, T.B. (2000): Pre-Caledonian granulite and gabbro enclaves in the Western Gneiss region, Norway: Indications of incomplete transition at high pressure. *Geol Mag*, **137**, 235–255.

- Lasaga, A.C. (1979): Multicomponent exchange and diffusion in silicates. *Geochim Cosmochim Acta*, **43**, 455–469.
- Le Pichon, X., Henry, P. & Goffé, B. (1997): Uplift of Tibet: from eclogites to granulites — implications for the Andean Plateau and the Variscian belt. *Tectonophysics*, **273**, 57–76.
- Lessing, P. & Standish, R.P. (1973): Zoned garnet from Crested Butte, Colorado. *Am Mineral*, **58**, 840–842.
- Lindgren, W. (1918): Volume changes in metamorphism. *J Geology*, **26**, 542–554.
- Lippmann, F. (1977): The solubility product of complex minerals, mixed crystals and three-layer clay minerals. *N Jb Miner Abh*, **130**, 243.
- Lippmann, F. (1980): Phase diagrams depicting the aqueous solubility of mineral systems. *N Jb Miner Abh*, **139**, 1–25.
- Lippmann, F. (1982): Stable and metastable solubility diagrams for the system  $\text{CaCO}_3 - \text{MgCO}_3 - \text{H}_2\text{O}$  at ordinary temperature. *Bull Mineral*, **105**, 273–279.
- Lund, M. & Austrheim, H. (2001): Pseudotachylyte-like veins in coronitic gabbros from Ålesund, Western Gneiss Region — The role of brittle faulting in high-grade metamorphism. *Norsk Geol Forening Landsmøte Program Sammendrag*, **17**, 76.
- Maden, M. & Ibaruchi, J.I.G. (1991): Characterization and thermodynamic properties of andradite,  $\text{Ca}_3\text{Fe}_2\text{Si}_3\text{O}_{12}$ . *Am Mineral*, **76**, 1249–1260.
- Maliva, R.G. & Siever, R. (1988): Diagenetic replacement controlled by force of crystallisation. *Geology*, **16**, 688–691.
- Mandelbrot, B.B. (1982): “The fractal geometry of nature”. W.H. Freeman, San Francisco.
- McAloon, B.P. & Hofmeister, A.M. (1993): Single-crystal absorption and reflection infrared spectroscopy of birefringent grossular–andradite garnets. *Am Mineral*, **78**, 957–967.
- McAloon, B.P. & Hofmeister, A.M. (1995): Single-crystal IR spectroscopy of grossular–andradite garnets. *Am Mineral*, **80**, 1145–1156.

- Meakin, P. (1998): "Fractals, scaling and growth far from equilibrium". Cambridge nonlinear science series, **no 5**, Cambridge University Press, Cambridge.
- Merino, E. & Dewers, T. (1998): Implications of replacement for reaction-transport modeling. *J Hydrol*, **209**, 137–146.
- Myers, E.R. (1998): Al/Si ordering in silicate minerals. PhD Thesis, University of Cambridge, Cambridge, UK.
- Myers, E.R., Heine, V. & Dove, M.T. (1998): Thermodynamics of Al/Al avoidance in the ordering of Al/Si tetrahedral framework structures. *Phys Chem Mineral*, **25**, 457–464.
- Novak, G.A. & Gibbs, G.V. (1971): The crystal chemistry of silicate garnets. *Am Mineral*, **56**, 791–825.
- Oda, H., Tanaka, T. & Seya, K. (1990): Subducting oceanic crust on the Philippine Sea plate in southwest Japan. *Tectonophysics*, **172**, 175–189.
- Olsen, A. (1979): Coherent elastic energies of exsolution boundaries in Peristerite and Bøggild intergrowth. *Phys Chem Mineral*, **4**, 115–127.
- O'Neil, J.R. & Taylor, H.P. Jr. (1967): The oxygen isotope and cation exchange chemistry of feldspars. *Am Mineral*, **52**, 1414–1437.
- O'Neil, J.R. & Taylor, H.P. Jr. (1969): Oxygen isotope equilibrium between muscovite and water. *J Geophys Res*, **74**, 6012–6022.
- Ortoleva, P., Merino, E., Moore, C. & Chadam, J. (1987): Geochemical self-organization I: reaction-transport feedbacks and modeling approach. *Am J Sci*, **287**, 979–1007.
- Peacock, S. (1990): Numerical simulation of metamorphic pressure-temperature-time paths and fluid production in subducting slabs. *Tectonics*, **9**, 1197–1211.
- Phemister, J. (1934): Zoning in plagioclase feldspar. *Mineral Mag*, **23**, 541–555.
- Plummer, L.N. & Busenberg, E. (1987): Thermodynamics of aragonite–strontianite solid solutions: Results from stoichiometric solubility at 25 and 76°C. *Geochim Cosmochim Acta*, **51**, 1393–1411.

- Plummer, L.N., Parkhurst, D.L., Fleming, G.W., Dunkle, S.A. (1989): A computer program incorporating Pitzer's equation for calculation of geochemical reactions in brines. *U.S. Geol. Surv. Water-Resources Investigations Report*, **88**, 4153.
- Prieto, M., Putnis, A. & Fernández-Díaz, L. (1993): Crystallization of solid solution from aqueous solution in a porous medium: zoning in  $(\text{Ba}, \text{Sr})\text{SO}_4$ . *Geol Mag*, **130**, 289–299.
- Prieto, M., Fernández-González, A., Putnis, A. & Fernández-Díaz, L. (1997): Nucleation, growth, and zoning phenomena in crystallizing  $(\text{Ba}, \text{Sr})\text{CO}_3$ ,  $\text{Ba}(\text{SO}_4, \text{CrO}_4)$ ,  $(\text{Ba}, \text{Sr})\text{SO}_4$ , and  $(\text{Ca}, \text{Cd})\text{CO}_3$  solid solutions from aqueous solutions. *Geochim Cosmochim Acta*, **61**, 3383–3397.
- Putnis, A. (1992): "Introduction to Mineral Science". Cambridge University Press.
- Putnis, A. (2002): Mineral replacement reactions: from macroscopic observation to microscopic mechanisms. *Mineral Mag*, **66**, 689–708.
- Putnis, C.V. & Mezger, K. (2004): A mechanism of mineral replacement: Isotope tracing in the model system  $\text{KCl} - \text{KBr} - \text{H}_2\text{O}$ . *Geochim Cosmochim Acta*, **68**, 2839–2848.
- Putnis, A., Putnis, C.V., Giampaolo, C. (1994): The microstructure of analcime phenocrysts in igneous rocks. *Eur J Mineral*, **6**, 627–632.
- Putnis, A., Prieto, M., Fernandez-Diaz, L. (1995): Supersaturation and crystallization in porous media. *Geol Mag*, **132**, 1–13.
- Redlich, O. & Kister, A.T. (1948): Algebraic representation of thermodynamic properties and the classification of solutions. *Industrial and Engineering Chemistry*, **40**, 345–348.
- Reeder, R.J. & Prosky, J.L. (1986): Compositional sector zoning in dolomite. *J Sediment Petrol*, **56**, 237–247.
- Reeves, N.J., Clegg, S.L., Brimblecombe, P. (2000): Data evaluation and molality-based parameterisation. in "An expert chemical model for determining the environmental conditions needed to prevent salt damage in porous material", C. Price, ed. Research Report no 11, Archetype Publications Ltd, London.

- Rendón-Angeles, J.C., Yanagisawa, K., Ishizawa, N., Oishi, S. (2000a): Conversion of calcium fluoroapatite into calcium hydroxyapatite under alkaline hydrothermal conditions. *J Solid State Chem*, **151**, 65–72.
- Rendón-Angeles, J.C., Yanagisawa, K., Ishizawa, N., Oishi, S. (2000b): Topotaxial conversion of chloroapatite and hydroxyapatite to fluorapatite by hydrothermal ion exchange. *Chem Mater*, **12**, 2143–2150.
- Rendón-Angeles, J.C., Yanagisawa, K., Ishizawa, N., Oishi, S. (2000c): Effect of metal ions of chloroapatites on the topotaxial replacement by hydroxyapatite under hydrothermal conditions. *J Solid State Chem*, **154**, 569–578.
- Robie, R.A., Zhao, B.I.N., Hemingway, B.S. & Barton, M.D. (1987): Thermodynamic properties of andradite garnet,  $\text{Ca}_3\text{Fe}_2\text{Si}_3\text{O}_{12}$ , between 10 and 1000 K and revised values for  $\Delta G_{f,298}^0$  of hedenbergite and wollastonite. *Geochim Cosmochim Acta*, **51**, 2219–2224.
- Rossmann, G.R. & Aines, R.D. (1986): Spectroscopy of a birefringent grossular from asbestos, Quebec, Canada. *Am Mineral*, **71**, 779–780.
- Rubie, D.C. (1990): Mechanisms of reaction-enhanced deformability in minerals and rocks. *in*: “Deformation Processes in Minerals, Ceramics and Rocks”, D. Barber & P. Meredith, eds. Chapman and Hall, New York.
- Rumble, D. III & Spear, F.S. (1983): Oxygen isotope equilibration and permeability enhancement during regional metamorphism. *J Geol Soc London*, **140**, 619–628.
- Sanders, M.J., Leslie, M. & Catlow, C.R.A. (1984): Interatomic potentials for  $\text{SiO}_2$ . *J Chem Soc Chem Commun*, **19**, 1271–1273.
- Shannon, R.D. & Rossmann, G.R. (1992): Dielectric constants of silicate garnets and the oxide additivity rule. *Am Mineral*, **77**, 94–100.
- Shore, M. & Fowler, A.D. (1996): Oscillatory zoning in minerals: a common phenomenon. *Can Mineral*, **34**, 1111–1126.
- Shtukenberg, A.G., Punin, Yu.O, Frank-Kamenetskaya, O.V., Kovalev, O.G. & Sokolov, P.B. (2001a): On the origin of anomalous birefringence in grandite garnets. *Mineral Mag*, **65**, 445–459.
- Shtukenberg, A.G., Punin, Yu.O., Haegeler, E. & Klapper, H. (2001b): On the origin of inhomogeneity of anomalous birefringence in mixed crystals: an example of alums. *Phys Chem Minerals*, **28**, 665–674.

- Silcock, H. L. (1979): "Solubilities of Inorganic and Organic Compounds". Pergamon Press, Oxford.
- Sobolev, S. & Babeyko, A. (1994): Modeling of mineralogical composition, density and elastic-wave velocities in anhydrous magmatic rocks. *Surv Geophys*, **15**, 515–544.
- Spear, F.S. (1993): "Metamorphic phase equilibria and pressure–temperature–time paths. Mineralogical Society of America: Monograph series.
- Spear, F., Peacock, S., Kohn, M., Florence, F. & Menard, T. (1991): Computer programs for petrologic P–T–t path calculations. *Am Mineral*, **76**, 2009–2012.
- Takéuchi, Y. & Haga, N. (1976): Optical anomaly and structure of silicate garnets. *Proc Jpn Acad*, **52**, 228–231.
- Takéuchi, Y., Haga, N., Shigemoto, U. & Sato, G. (1982): The derivative structure of silicate garnets in grandite. *Zeitschr Kristallogr*, **158**, 53–99.
- Thompson, A.B. & England, P.C. (1984): Pressure-temperature-time paths of regional metamorphism II. Their inference and interpretation using mineral assemblages in metamorphic rocks. *J Petrol*, **25**, 929–955.
- Tomaschek, F., Kennedy, A.K., Villa, I.M., Lagos, M. & Ballhaus, C. (2003): Zircons from Syros, Cyclades, Greece — Recrystallization and mobilization of zircon during high-pressure metamorphism. *J Petrol*, **44**, 1977–2002.
- Tovbin, M.V. & Krasnova, S.I. (1951): Stability of supersaturated solutions of salts. *Zh Fiz Khim*, **25**, 161–166 (in Russ.).
- Turcotte, D.L. (1997): "Fractals and chaos in geology and geophysics". Cambridge University Press, Cambridge.
- Van Cappellen, E. & Doukhan, J.C. (1994): Quantitative transmission X-ray microanalysis of ionic compounds. *Ultramicroscopy*, **53**, 343–349.
- Van Roermund, H.L.M. & Lardeaux, J.M. (1991): Modification of antiphase domain sizes in omphacite by dislocation glide and creep mechanisms and its petrological consequences. *Mineral Mag*, **55**, 397–407.
- Van Wyck, N., Valley, J.W. & Austrheim, H. (1996): Oxygen and carbon isotopic constrains on the development of eclogites, Holsnøy. *Lithos*, **38**, 129–147.

- Walker, F.D.L., Lee, M.R., Parson, I. (1995): Micropores and micropermeable texture in alkali-feldspars: geochemical and geophysical implications. *Mineral Mag*, **59**, 505–534.
- Walther, J.V. & Wood, B.J. (1986): Mineral–Fluid reaction rates. *in*: “Fluid–rock interactions during metamorphism”, J.V. Walther, B.J. Wood, eds. *Advances in Physical Geochemistry*, vol. 5, Springer Verlag.
- Wayte, G.J., Wordon, R.H., Rubie, D.C. & Droop, G.T.R. (1989): A TEM study of disequilibrium plagioclase breakdown at high pressure: the role of infiltrating fluid. *Contrib Mineral Petrol*, **101**, 559–570.
- Westrum, E.R. Jr., Essene, E.J. & Perkins, D. III. (1979): Thermophysical properties of the garnet, grossular:  $\text{Ca}_3\text{Al}_2\text{Si}_3\text{O}_{12}$ . *J Chem Thermophys*, **11**, 57–66.
- Yanagisawa, K., Rendón-Angeles, J.C., Ishizawa, N., Oishi, S. (1999): Topotaxial replacement of chloroapatite by hydroxyapatite during hydrothermal ion exchange. *Am Mineral*, **84**, 1861–1869.
- Yang, T.J., Gopalan, V., Swart, P. & Mohideen, U. (2000): Experimental study of internal fields and movement of single ferroelectric domain walls. *J Phys Chem Solids*, **61**, 275–282.
- Yeomans, J.M. (1992): “Statistical mechanics of phase transitions”. Oxford Science Publications, Clarendon Press, Oxford.
- Zhang, R. & Liou, J. (1997): Partial transformation of gabbro to coesite-bearing eclogite from Yangkou, the Sulu Terrane, eastern China. *J Metamorph Geol*, **15**, 183–202.
- Zhang, L., Ahsbahs, H., Kotuglu, A. & Geiger, C.A. (1999): Single-crystal hydrostatic compression of synthetic pyrope, almandine, spessartine, grossular and andradite garnets at high pressures. *Phys Chem Mineral*, **27**, 52–58.





